2015-01-21

Reliability Improvement of Sensors Used in Personal Navigation Devices

Dhital, Anup

UNIVERSITY OF CALGARY

Reliability Improvement of Sensors Used in Personal Navigation Devices

by

Anup Dhital

A THESIS

SUBMITTED TO THE FACULTY OF GRADUATE STUDIES

IN PARTIAL FULFILMENT OF THE REQUIREMENTS FOR THE

DEGREE OF DOCTOR OF PHILOSOPHY

GRADUATE PROGRAM IN GEOMATICS ENGINEERING

CALGARY, ALBERTA

JANUARY, 2015

Abstract

Along with advancements in microelectromechanical system (MEMS) technology, many modern personal navigation devices incorporate measurements from various sensors alongside Global Navigation Satellite Systems (GNSS) receivers. Despite using these sensors, GNSS still remains an important component of these navigation devices in view of its absolute positioning capability. Thus, when it comes to navigating in GNSS signal degraded areas like in urban and natural canyons, the performance of such multi-sensor integrated navigation systems is still found to be sub-optimal. In particular, existing filtering algorithms are often unreliable in such environments. This affects the usability of such personal navigation devices in some applications where reliability is a critical parameter. Moreover, reliability can be further degraded by the occurrence of faults in other sensors besides GNSS. This research thus develops several algorithm modules with an ultimate goal of improving the performance, and especially reliability, for low cost multi-sensor integrated navigation systems.

Among the proposed algorithm modules, the first method modifies the filtering algorithm by replacing the assumption of normal distribution of GNSS measurements with that of a heavy-tailed distribution. The second module adapts the covariance of the GNSS measurements to match the true error characteristics of the surrounding environment, based on the consistency of GNSS derived user acceleration values to those obtained from inertial measurement units. Finally, a third algorithm module detects possible faults arising in various sensors. Based on the type of sensor fault, the algorithm either rejects some of the measurements before they enter the integration filter, issues a warning signal to indicate lack of reliability information or deems the navigation solution unusable. The

proposed algorithms are tested with numerous field data sets collected in various environments as well as with carefully simulated faults that are added to clean measurements.

The analysis of the results obtained using the proposed methods indicate a significant improvement in the reliability of the navigation solution. The average improvement in the reliability varied between 15 % and 26 % for the data sets used in the analysis. Position accuracy was also found to improve. In particular, maximum position errors are significantly decreased, up to a factor of 2.5 in some cases. Finally, the simulated as well as actual faults occurring in the sensor measurements were also correctly detected.

Acknowledgements

First and foremost, I would like to express my sincere gratitude to my supervisor, Professor Gérard Lachapelle. It was an honour and privilege to receive your gracious guidance and support throughout my doctoral studies. Your valuable advices have not only helped me in my academic pursuits but also to grow in a personal level. I would also like to thank you for providing me the opportunity to accompany you in numerous hikes in the beautiful Rockies.

My sincere gratitude goes to my advisor, Dr. Jared Bancroft. Thank you very much for the valuable discussions, guidance and comments from the beginning to end of my doctoral research and thesis writing. Your kind support during this period is highly appreciated. A special thanks also goes to Professor Kyle O'Keefe for his valuable feedbacks during different stages of this research.

A special thanks to Srinivas Bhaskar, Sergey Krasovski, Bernhard Aumayer and Rakesh Kumar for helping me with, often very physically demanding data collections. I thank Thomas Moaut for proof-reading and correcting my thesis. I have been immensely fortunate to meet so many good friends in the PLAN Group during the last four years. I thank you all for your friendship and for the sense of a family far from home. I would also like to thank my Nepalese friends in Calgary for all the good times that we have had together.

Finally, I thank my parents and my little sister for their unconditional love and support throughout my life. This would not have been possible without the warmth of your love.

To my mom, dad and my sweet sister…

Table of Contents

List of Tables

List of Figures

List of Symbols and Abbreviations

Symbol	Definition
A	Azimuth
b	Bias
c	Speed of light
d_{iono}	Ionospheric delay
d_{tropo}	Tropospheric delay
$\dot{d}_{iono}$	Ionospheric error drift
$\dot{d}_{tropo}$	Tropospheric error drift
dT	Receiver clock bias
dt^i	Clock bias of i^{th} satellite
$d\dot{T}$	Receiver clock drift
$d\dot{t}^i$	Clock drift of i^{th} satellite
$d\rho$	Orbital position error
$d\dot{\rho}$	Orbital velocity error
F	Dynamic matrix
f	Specific force
g	Acceleration due to gravity
H	Design matrix
h	Altitude
H^n	Magnetic field vector in n frame
K	Kalman gain
L_g	Atmospheric temperature gradient
N_{amb}	Integer Ambiguity
N_x	Non-orthogonality of sensor x
P	Pressure

p	Pitch
P_k	State covariance at k^{th} epoch
P_o	Standard pressure at sea level
Q	Process noise covariance
R	Measurement noise covariance
r	Roll
R_g	Ideal gas constant
R_a^b	Rotation from frame a to b
r^i	Range between receiver and i^{th} satellite
S	Scale factor
T_o	Standard temperature
w	Angular velocity
α	Significane level
δg	Gravity error
ε	Stochastic error
λ	Longitude
λ_c	Wavelength
Φ	Transition matrix
φ	Latitude
$\dot{\phi}^i$	Doppler of i^{th} satellite
ρ^i	Pseudorange of i^{th} satellite
σ	Standard deviation
ξ	Test statistic
$(\dot{\bullet})$	Time derivative
$(\ddot{\bullet})$	Double time derivative
$(\hat{\bullet})$	Estimate
$(\tilde{\bullet})$	Measured parameter

$(\bullet)^{-}$	Predicted parameter
$(\bullet)^{+}$	Updated parameter
$(\bullet)^{T}$	Transpose
$(\bullet)(t)$	Function of time

Abbreviation	Definition
AMR	Anisotropic Magneto Resistive
AR	Auto Regressive
ARMA	Auto Regressive Moving Average
BC	Bhattacharyya Coefficient
BDS	BeiDou Satellite Navigation System
CDF	Cumulative Distribution Function
CKF	Cubature Kalman Filter
DoD	Department of Defense
ECEF	Earth Centred Earth Fixed
EKF	Extended Kalman Filter
ENU	East North Up
ESA	European Space Agency
FDE	Fault Detection and Exclusion
FOG	Fibre Optic Gyroscope
GM	Gauss Markov
GNSS	Global Navigation Satellite System
GPS	Global Positioning System
HSGPS	High Sensitivity GPS
IGRF	International Geomagnetic Reference Field
IMU	Inertial Measurement Unit
INS	Inertial Navigation System
IRNSS	Indian Regional Navigation Satellite System
ISA	International Standard Atmosphere
KL	Kullback-Leibler
KF	Kalman Filter
LKF	Linearized Kalman Filter
LLF	Local Level Frame
LS	Least Squares
MEMS	Micro Electro Mechanical Systems

MEO	Medium Earth Orbit
NCO	Numerically Controlled Oscillator
NLOS	Non Line of Sight
PDOP	Position Dilution of Precision
PND	Personal Navigation Device
PNT	Position Navigation and Timing
PPS	Pulse per Second
PRN	Pseudo Random Number
PSD	Power Spectral Density
QZSS	Quasi-Zenith Satellite System
RAIM	Receiver Autonomous Integrity Monitoring
RF	Radio Frequency
RLG	Rate Laser Gyro
RMSE	Root Mean Square Error
SNR	Signal to Noise Ratio
TOA	Time of Arrival
UKF	Unscented Kalman Filter
VB	Variational Bayes
ZUPT	Zero Velocity Update
ZARU	Zero Angular Rate Update

Chapter One: **Introduction**

Global Navigation Satellite Systems (GNSS) receivers have become an essential feature of modern day life. They are used for a variety of applications such as navigation, location, survey and precise timing. While originally designed for military applications, GNSS soon became an essential component of many civilian applications like aviation and car navigation. In recent years, GNSS have become the backbone of an extensive number of civilian applications including many personal navigation applications. Users of modern navigation applications would like to have personal navigation devices that have seamless, continuous navigation capability. Despite tremendous improvements in performance during the last decade, however, when it comes to signal degraded environments, namely urban canyons, under foliage or indoors, GNSS still fails to achieve these requirements. A very promising approach to meet the aforesaid criteria is to aid GNSS with other complementary sensors, such as inertial measurement units (IMU), barometers and magnetometers. The speedy advancement in the microelectromechanical systems (MEMS) technology in the last decade or so has enabled the realization of these complementary sensors in extra small forms. Along with the reduction in size, MEMS realization also significantly reduces power consumption, thus making them suitable for use in portable navigation devices. In such integrated navigation systems, the information from various sensors is fused together to obtain a final solution. The data fusion process comes with two inherent challenges that have to be addressed appropriately. Firstly, the measurement from various sensors should be modeled as accurately as possible and all the uncertainties should be incorporated during

data fusion. Secondly, if an unmodeled error occurs in any of the sensor measurements, the navigation system may not be able to identify the degradation of the navigation solution and, consequently, the users may not be alerted about such degradation, thus making navigation unreliable. Reliability is one of the most critical parameters for many applications using integrated navigation devices. Hence, it becomes essential to have a mechanism that ensures the detection and isolation of modeled as well as unmodeled errors in all the sensors being used.

1.1 Background

Personal Navigation Devices (PND) are portable electronic devices that can be used for positioning and navigation purposes. They include electronic appliances with a wide spectrum of applications, ranging from road navigation units, used in automobiles, to various pedestrian navigation applications, including mobile phone users, first responder services, military, travel aids for visually impaired, etc. Initially, PNDs were purely based on GNSS. However, with the advent of new technologies, progress in the GNSS receiver technologies, and with the immense expansion of the markets of PNDs, the requirements of many applications have also increased. The PNDs based on GNSS alone often fall short of meeting these requirements in terms of accuracy, availability and reliability. Specifically, meeting these requirements while navigating in urban canyons, dense foliage areas and indoors is most difficult since in these environments GNSS suffers from problems such as a limited field of view, signal attenuation, multipath and signal unavailability (Lachapelle 2010). These problems have been alleviated to some extent by the development of high sensitivity GNSS (HS-GNSS) receivers (Van Diggelen 2009). In

indoor environments, dense forests, urban areas, or any other area where the GNSS signals are strongly attenuated, the use of HS-GNSS can significantly improve the chance of detecting GNSS signals, thus improving the availability of a navigation solution. The goal of these HS-GNSS receivers is to improve the signal detection ability, by improving the signal to noise ratio (SNR). However, as the broadcast GNSS signal power cannot be increased, a HS-GNSS receiver reduces the effect of the noise on the correlation process by increasing the integration time for the acquisition of the signal (Bickerstaff et al 2006). The maximum integration time, though, is limited due to requirements like the ability to track the user dynamics, time to first fix (TTFF) and navigation data bit transitions. These limitations are addressed to some extent by using more correlators, to speed up the signal search or sometimes, by reducing the search space on signal parameters through the use of assisted information (Van Diggelen 2009). Nevertheless, integrating the signal for longer duration makes the receivers more susceptible to multipath errors (Lachapelle 2010), which results in large position and velocity errors. Thus, in spite of using HS-GNSS, the PND's based on GNSS alone don't meet the requirements of many applications, mainly in terms of reliability of the navigation solution. As a result, recent PNDs are often found to be integrated with other self-contained sensors, e.g., IMU, wheel speed sensors, barometers, etc. These sensors are self-contained, in the sense that they can be used in almost any location or environment, and they don't rely on an external reference system or an external radio frequency (RF) signal source. An integrated navigation system called AP15, recently developed by Trimble Navigation Ltd, is an example of the form of modern PNDs that can be used for a variety of commercial mobile positioning and orientation applications. Moreover, when combined with a wheel-mounted

Distance Measurement Instrument (DMI), in addition to the GNSS receiver and inertial sensors, this unit provides a full 6-degrees-of-freedom navigation solution for land vehicles that is capable of providing position and orientation information even during times when the GNSS is completely denied (GPS World 2013). Similar products from several manufacturers that use other sensors besides GNSS are now commercially available and extensively used in numerous applications, e.g., tracking of first responders, human motion analysis in sports, or analysis of braking and acceleration technology in vehicles.

Nevertheless, even for personal navigation devices that consist of GNSS integrated with other self-contained sensors, especially those using relatively low cost MEMS IMUs, the quality of GNSS signals plays a significant role in navigation. Consequently, when it comes to harsh environments, the absence of GNSS or the presence of biased and noisy GNSS measurements can result in significant errors, depending upon the quality of the sensors and the navigation algorithm being used. There are two facets to this problem, firstly the possibility of errors should be appropriately reflected by the estimated accuracy of the navigation solution; and secondly, these errors should be reduced as much as possible through proper characterization of their statistics. The first issue is the problem of reliability. Reliability is the level of trust that can be placed on the navigation solution provided by a personal navigation device. It specifies a degree of confidence about the accuracy of the estimated navigation solution. Reliability is very important for some applications, especially those related to safety and authentication. For instance, a tracking system worn by a criminal offender that monitors the offender's movement within local communities should be very reliable, as it is associated with safety and legal

consequences. Some other examples of such applications include military operations, authenticating user's identity through position for electronic voting, etc. Moreover, in personal navigation devices that use multiple sensors to generate the navigation solution, an undetected fault in any of the sensors can make the computed navigation solution unreliable. Hence, in such multi-sensory integrated navigation systems, reliability should also be monitored at the individual sensor level.

1.2 Limitations of Previous Work

A reliable navigation solution can be obtained by detecting, identifying and removing faults in any of the sensor measurements used to obtain the final solution. In the case of GNSS, this basically means finding faults in measurements from satellites. However, personal navigation devices also use other sensors, besides GNSS, in order to obtain the navigation solution. Hence, it is also necessary to validate the measurements obtained from these sensors by detecting and removing any fault present therein.

The following sub-sections present a brief review of some of the theoretical contributions and research developments related to the reliability of navigation systems made in the past. Moreover, these contributions are broadly categorized into two types, namely those dealing with faults in GNSS measurements and secondly, those that take into account faults in other sensors.

1.2.1 Faults in GNSS measurements

For the case of GNSS, reliability can be obtained either at the system level or at the user level. Faults occurring at the system level have been the focus of most reliability schemes developed since the very early days of GNSS. These faults mainly comprise those arising

on the satellite side (errors in orbital predictions, satellite clock, etc.) and the ionospheric error. However, for personal navigation devices, the problem mainly occurs at the user level. In harsh environments, GNSS signal degradation occurs in user surroundings due to such issues as multipath, signal blockage and attenuation. Hence, in these environments, reliability has to be implemented at the user level (Simon et al 2010). User level reliability can be obtained through receiver autonomous integrity monitoring (RAIM). Over the years, many RAIM schemes have been proposed in the literature (e.g., Lee 1986, Sturza 1988, Parkinson & Axlerad 1987, etc.), and they are all based on some kind of self-consistency checks among the available measurements. Since RAIM was originally designed for aviation, to detect the failures in satellites, many assumptions made during its development are not suitable for ground based personal navigation devices. For instance, the assumption about the presence of a single fault at a time is not appropriate for location based services as the occurrence of multiple simultaneous faults, such as large code multipath combined with high noise, is common in urban canyon environments. Moreover, assuming that the errors are distributed normally may also be unsuitable, especially in the presence of multipath. As a result, traditional RAIMs tend to degrade in performance when it comes to determining the reliability of navigation solutions in signal degraded environments. As depicted in Figure 1-1, the blockage of GNSS signals by buildings and structures often reduces the visibility of satellites in urban areas or inside buildings. Relying on traditional RAIMs in such scenarios can thus lead to unavailability of reliability information, due to lack of sufficient redundancy following the removal of faulty measurements.

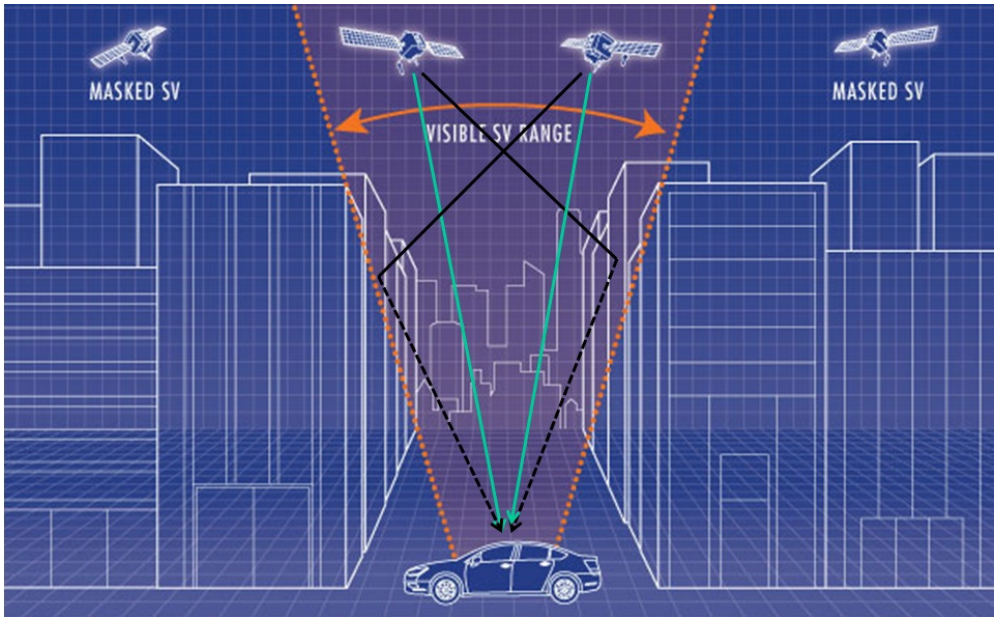

Figure 1-1: GNSS Signal Masking in Urban Area

Some new RAIM schemes have been proposed to address the problem of multiple simultaneous faults, e.g. Angus (2006), Kuusniemi (2005) and Schroth et al (2008). However, removing multiple satellites often leads to unavailability of the reliability scheme, especially in areas where visibility of satellites is very poor. Moreover, in some of these algorithms, the computational complexity increases drastically as the number of available measurements increase and the error bound increases with the number of measurement faults. In particular, it is noted that, as new global and regional navigation systems are being developed and deployed, many contemporary PNDs are capable of tracking navigation signals from multiple constellations. The addition of the new satellite signals, through the incorporation of newer constellations, drastically increases the computational cost of the aforementioned fault detection and exclusion techniques.

Furthermore, the fault detection schemes generally assume constant measurement error statistics, as reflected by the GNSS measurement covariance. In degraded environments, this assumption is often invalid, as the true GNSS error statistics varies while the user navigates. This can be addressed by adapting the assumed covariance of the GNSS measurements to suit the true measurement quality. Several techniques have been proposed in the literature to adapt the covariance of GNSS measurements. These techniques, however, come with several drawbacks, such as filter instability, divergence and computational complexity (Almagbile et al 2010, Hide et al 2002). This calls for the development of reliability scheme that takes into account all the challenges in the signal degraded environments and is suitable for all kinds of personal navigation applications.

1.2.2 Faults in other sensors

As mentioned earlier in Section 1.1, in case of a multi-sensory integrated navigation system, the measurements from sensors other than GNSS have to be validated as well in order to obtain a reliable navigation solution. The users of such personal navigation devices often navigate in environments where GNSS measurements are corrupt, very scarce or even totally denied, thus rely heavily on other sensors for navigation. As a consequence, a fault in any of these sensors can result in highly unreliable navigation solutions. Therefore, detecting the faults in these sensors is very important for personal navigation devices. Although this issue was identified a long time ago, only limited research work can be found in the literature. For instance, Sturza (1988), Wei & Huddle (1986) and Bancroft & Lachapelle (2011) used multiple inertial systems in order to attain sufficient redundancy, and the reliability was subsequently obtained by checking the

consistency between multiple navigation solutions corresponding to each inertial system. However, this approach of using multiple inertial systems significantly increases cost and complexity. Similarly, Sukkarieh et al (2000) propose a redundant inertial measurement unit for unmanned air vehicles that uses multiple low-cost accelerometers and gyroscopes whose measurements are combined optimally to improve the information content of the integrated navigation system. Such redundant inertial sensor configurations allow the detection of faults in any of the inertial sensors being used. Furthermore, Bras et al (2012) propose two strategies to detect and isolate the faults in the inertial sensors. The first approach simply uses redundant measurements from multiple sensors of similar kind, while the second approach exploits the analytical redundancy between dissimilar sensors. Both of these approaches use multiple inertial sensors and hence carry the same drawbacks as the previous techniques. In conclusion, the research mentioned above and other similar work is found to use redundant sensors, in order to validate the proper operation of the self-contained sensors resulting in higher cost and and often higher complexity of the overall navigation system. Hence, there is a need to explore and design a cost effective reliability scheme that can detect and isolate faults in any of the navigation sensors used in integrated navigation systems. This becomes increasingly important with low cost portable devices that have limited power supplies and are limited in size.

1.3 Objectives and Contributions

Considering the limitations of existing work related to the reliability of personal navigation devices that are based on multiple sensors, this research proposes a novel scheme to

improve the reliability of personal navigation applications. In particular, the research investigates new methods to optimize the use of GNSS measurements in harsh signal conditions, as well as to assess the reliability of individual sensors, by exploiting the analytical redundancy among the dissimilar sensor measurements. The specific objectives and contributions of this thesis are summarized as follows:

1. *Optimization of the use of GNSS measurements in harsh signal conditions*: The research primarily focuses on improving the reliability of personal navigation systems in areas where GNSS signals are degraded. In this regard, some algorithms are developed that take into account wide-ranging challenges pertaining to such environments and either assign appropriate weights to the GNSS measurements or reject the bad measurements. The key idea here has been to characterize the GNSS measurement errors as closely as possible to the true error statistics.
2. *Pre-filter validation of self-contained sensors*: The reliability of multi-sensor integrated navigation system relies on proper functioning of each individual sensor used for navigation. Hence, it is imperative to ensure that the measurements from all of these sensors are valid. A pre-filter sensor validation scheme is thus developed where the mathematical relationships between different sensor measurements are used to obtain analytical redundancy between different types of sensors. This scheme confirms the correct operation of various sensors before they are used to generate the navigation solution. Any sensor measurement that

is deemed to be invalid by the pre-filter sensor validation scheme is discarded by the navigation filter.

3. *Assessment and analysis of the integrated navigation system*: The proposed algorithms and architectures are assessed through multiple sets of field data collected in varied environments. The performance of the integrated navigation system is analysed from different perspectives. Specifically, the fault detection and exclusion capability of the proposed architecture is assessed through the computed reliability values. Such analysis involves the use of simulated faults added to clean data, as well as the faults that are attributed to the navigation environment. Finally, the advantages and limitations of the proposed scheme are identified.

1.4 Thesis Outline

After a brief background of personal navigation devices, and description of the research objectives, the remainder of the thesis is organized as follows:

Chapter 2 provides the theoretical background related to multi-sensor integrated navigation systems. It starts with a brief introduction of the sensors used in a typical personal navigation device and presents the measurement error characteristics of these sensors. The theory of Kalman filtering is then introduced, followed by details on multi-sensor integration techniques. The standard Kalman filter based multi-sensor integrated navigation system, developed following the techniques presented herein, will serve as a benchmark against which the novel methods proposed in this thesis will be compared.

The concept of residual based statistical reliability testing and reliability theory in general is presented in **Chapter 3**. The challenges of fault detection in degraded GNSS signal environments are discussed and the limitations of conventional fault detection techniques are identified. A concept of reliability for multi-sensor integrated navigation systems is then introduced. In addition, the possibilities of faults in different sensors and their nature are briefly discussed.

Chapter 4 details the development of a novel filtering architecture, which is proposed to improve the reliability of navigation solution in harsh GNSS signal environments. Firstly, the idea of using a heavy tailed distribution for GNSS measurement errors is presented. The implementation and fault handling that results from using such a distribution is also detailed. Finally, an adaptive approach that changes the assumed covariance of the GNSS measurements to suit the actual error characteristics in the user surroundings is presented.

In **Chapter 5**, a pre-filter sensor validation scheme is proposed to detect and isolate faults in disparate sensors. Several mathematical developments that observe common parameters using dissimilar sensors are presented in the subsequent sub-sections. Ultimately, the order of fault handling and the actions taken during the occurrence of faults in any of the sensors is demonstrated through a flowchart of the proposed scheme.

Chapter 6 elaborates on the experimental setup, including the equipments being used, the mode of navigation, test environments, etc. The proposed algorithms are assessed through an in depth analysis of the results obtained by processing multiple sets of field

data collected in such varied environments as open sky, urban canyons and natural canyons. Primarily, the proposed algorithms are assessed in terms of reliability and accuracy of the navigation solution.

Finally in **Chapter 7**, the major contributions of the thesis are summarized; some conclusions are drawn based on the assessment of the proposed algorithms and possible future work is identified.

Chapter Two: **Multi-sensor Personal Navigation Devices**

This chapter begins with a brief presentation of the theoretical background on disparate sensors and systems used in modern PNDs. In particular, the working principles of the sensors being used in the realization of the multi-sensor PND prototype used in this thesis are discussed. The techniques used to integrate the sensor measurements in such integrated navigation systems are then provided.

2.1 GNSS

Global Navigation Satellite System (GNSS) refers to any radio navigation system that provides geo-spatial positioning with global coverage, using signals transmitted from satellites. The user position is determined through a technique called *trilateration;* wherein, the distances to the satellites from the user's position are estimated based on the time of arrival (TOA) of the signals. Global Positioning System (GPS), the first modern GNSS, was developed by the U.S. Department of Defense (DoD) and was declared operational in 1995. Although primarily designed for military use, GPS provides position, navigation and timing (PNT) services to both military and civilian users. Besides GPS, other global and regional navigation systems have been developed over the years that have significantly contributed to the revolutionizing of satellite based navigation. Another fully operational GNSS called GLONASS (Global Navigation Satellite System) was developed by the Russian Federation and is providing similar services as the GPS. Yet another GNSS is being built by the European Union (EU) and the European Space Agency (ESA) and is called Galileo. A few satellites have already been deployed and

position was computed using solely Galileo signals for the first time on March 2013. As of now, the Galileo system is expected to be fully operational by around 2020. Similarly, China is also developing a GNSS called the BeiDou Satellite Navigation System (BDS), which has already begun offering services in some regions and is expected to be fully operational by 2020. Besides GNSS, several regional navigation systems such as the Indian Regional Navigation Satellite System (IRNSS) and the Japanese Quasi-Zenith Satellite System (QZSS) are also being developed. These regional navigation systems are very similar to GNSS in terms of structure and functionality, but differ from GNSS in that they are designed to offer reliable services in only a specific region, as compared to the world wide coverage of the GNSS. The availability of various global and regional navigation systems and the possibility to combine them together in a receiver have made an immense impact on the performance of satellite based navigation systems and helped the proliferation of applications that benefit from using such navigation systems.

2.1.1 GNSS Architecture

A GNSS mainly consists of three segments: the Space Segment, the Control Segment and the User Segment.

The space segment basically comprised the satellite payloads and the orbital configuration over which the satellites orbit. In the case of GPS, the space segment consists of a medium earth orbit (MEO) constellation of 24 satellites, distributed in six nearly circular orbital planes, inclined at 55 degrees relative to the equatorial plane (Misra & Enge 2011). Similarly, the GLONASS space segment also consists of a MEO constellation of 24 satellites, but distributed in three orbital planes, whose ascending

nodes are 120 degrees apart (ICD GLONASS 5.1 2008). The Galileo space segment, however, will be comprised of a MEO constellation of up to 30 satellites (including three active spares) distributed in three orbital planes, inclined at 56 degrees.

The control segment, also known in some cases as the ground segment, comprises a few control stations or master stations and several other ground stations that are dispersed over various locations. The major functions of the control segment include monitoring satellite orbits and satellite health, predicting ephemerides and clock parameters, and updating satellite navigation messages (Misra & Enge 2011).

Finally, the user segment consists of the GNSS receivers, whose main function is to receive the satellite signals, determine the measurement observables and solve the navigation equations in order to provide various PNT services.

2.1.2 GNSS Measurements

The most common GNSS observable is the *code phase measurement*. The signal transmitted by a satellite can be identified and aligned with the receiver generated replica signal, by using the autocorrelation properties of the pseudorandom noise (PRN) code. Assuming that all the satellites and receivers are synchronized to the system time and that there is no clock drift, such alignment at the receiver gives the signal transit time, which on multiplication by the speed of light in vacuum yields the satellite-receiver range (Misra & Enge 2011). However, since the satellite and receiver clocks are not synchronized, there is a bias in range that is computed in this manner. Hence, each range measurement is contaminated by clock error, as a result of which these range measurements are also referred to as *pseudorange* measurements. In addition to the

clock errors, the pseudorange measurements are further diluted by the introduction of other error components as well. The code phase or pseudorange observable between a receiver and an i^{th} satellite can be represented as (Lachapelle 2010)

$$\rho^i = r^i + c(dT - dt^i) + d\rho + d^i_{iono} + d^i_{tropo} + \varepsilon^i_\rho \qquad \textbf{2-1}$$

where

r^i : range between receiver antenna and satellite *i* (m)

c : speed of light (m/s)

dT : receiver clock error with respect to the system time (s)

dt^i : satellite clock error with respect to the system time (s)

$d\rho$: orbital position error (ephemeris) (m)

d^i_{iono} : ionospheric delay (m)

d^i_{tropo} : tropospheric delay (m)

ε^i_ρ : receiver noise, multipath and unmodeled errors (m)

Although pseudoranges are the most common GNSS observables, they are not the most precise ones. A much precise satellite to receiver range can be obtained using *carrier phase measurements*. The carrier phase measurement by a GPS receiver is the difference between the phases of the receiver generated carrier signal and the carrier signal at the same frequency received from a satellite at the instant of the measurement (Misra & Enge 2011). This provides an indirect means of measuring the signal transit time and, consequently, the satellite-receiver range. The initial difference between the two

phases is a fraction of a cycle of the carrier signal. When the tracking is continued, the carrier phase measurement becomes a certain number of full carrier cycles, plus a fractional part of the phase cycle. The initial integer number of whole cycles, known as the integer ambiguity, is however unknown and thus has to be solved along with other navigation parameters. The carrier phase measurement for the i^{th} satellite can be expressed in the unit of length (m) as

$$\phi^i = r^i + c(dT - dt^i) + d\rho + \lambda_c N_{amb} - d^i_{iono} + d^i_{tropo} + \varepsilon^i_\phi \qquad \textbf{2-2}$$

where

λ_c : carrier wavelength (m)

N_{amb} : integer ambiguity

ε^i_ϕ : receiver noise, carrier phase multipath and unmodeled errors (m)

In spite of being very precise, the carrier phase measurements cannot easily be used for several applications, due to frequent losses of phase lock which lead to cycle slips. Cycle slips are the discontinuities in the measured number of cycles (ambiguities) that occur due to numerous reasons such as loss of one or more satellites, blunders in measurements and excessive receiver dynamics. A new ambiguity occurs each time a cycle slip occurs, making the effective use of carrier phase difficult to achieve in pedestrian environments, although current research is addressing this limitation. For instance, Bhaskar (2014) proposes a technique that exploits the quasi-periodic nature of the pedestrian dynamics to dynamically compensate for the changes occurring in carrier phase measurements as a result of such dynamics.

Similarly, another GNSS observable, commonly used in many applications, is the *Doppler measurement*. This is a measure of the frequency shift of the tracked satellite's signal, as indicated by the numerically controlled oscillator (NCO). The observed frequency differs from the nominal carrier frequency, because of Doppler shifts produced due to the dynamics and clock drifts of both the satellite and the user (Axelrad & Brown 1996). The Doppler shift caused by relative satellite and user motion is proportional to the projection of the relative velocities onto the line of sight vector. The Doppler measurements thus formed can be used to determine the absolute user velocity. The Doppler observation of the ith satellite, in units of m/s, is given as

$$\dot{\phi}^i = \dot{r}^i + c(d\dot{T} - d\dot{t}^i) + d\dot{\rho} + \dot{d}^i_{iono} + \dot{d}^i_{tropo} + \varepsilon^i_{\dot{\phi}} \qquad \textbf{2-3}$$

where

$\dot{r}^i$: range rate between receiver antenna and satellite *i* (m/s)

$d\dot{T}$: receiver clock drift error

$d\dot{t}^i$: satellite clock drift error

$d\dot{\rho}$: orbital velocity error (ephemeris) (m/s)

$\dot{d}^i_{iono}$: ionospheric error drift (m/s)

$\dot{d}^i_{tropo}$: tropospheric error drift (m/s)

$\varepsilon^i_{\dot{\phi}}$: receiver noise, Doppler multipath rate of change and unmodeled errors (m)

2.1.3 GNSS Measurement Errors

Based on their sources, GNSS measurement errors can be broadly categorized into three classes, namely i) satellite-based errors, ii) propagation errors and iii) receiver-based errors (Lachapelle 2010).

i) Satellite-based errors mainly include orbital errors, satellite clock errors and group delay. Orbital errors, also referred to as ephemeris errors, and satellite errors are caused by imperfections in the prediction of orbital and clock parameters that occur in the control stations. These prediction errors grow with the age of data and hence can be reduced through more frequent data uploads to the satellites (Misra & Enge 2011). The difference in delays experienced in the satellites, by signals of different frequencies, results into an error termed as group delay. A scaled version of such delay is broadcast in the ephemeris, which should be taken into account at the receiver.

ii) Propagation errors are constituted by errors contributed by different media, as the signal traverses from the satellite to a receiver. One of the most critical mediums that affects the GNSS signal is the ionospheric layer of the atmosphere. Characterized by the presence of free electrons, the ionosphere causes the speed of the signal to be different from that in vacuum, thus resulting in a delay in the range measurements and a phase advance by an equal magnitude in the carrier phase measurements. The effects of this dispersive medium are more severe during a phenomenon called ionospheric scintillation. The ionospheric error can be mitigated to some extent by using multiple frequency signals or by using ionospheric models. Another deviation from the vacuum speed of light is caused by the troposphere. The speed of radio waves through the troposphere depends

on factors such as temperature, pressure and humidity (Parkinson 1996). The tropospheric error is also mitigated by the use of some tropospheric models. Besides these atmospheric effects, some intentional or unintentional radio frequency interference, coming from radio transmitters in the vicinity of a receiver, can also result in measurement errors. However, a more serious error that occurs due to the medium in the user proximity is multipath. Multipath is an error caused by reflected signals entering the front end of the receiver and masking the real correlation peak. Multipath is more severe in areas with large reflecting surfaces, such as urban areas and natural canyons. Multipath can cause significant biases in the GNSS measurements, especially in the absence of line of sight signals. Although various techniques have been proposed to mitigate the effect of multipath, it still remains a challenging problem.

iii) Receiver-based errors are mainly comprised of stochastic noise introduced in various components of the receiver and a number of deterministic bias components. Random measurement noise is introduced in various sections of the receivers, including antenna, amplifiers, cables, etc. Errors, both stochastic and deterministic, are also introduced due to the imperfections of receiver clocks. Finally, some deterministic biases are introduced by transmission delays in various sections of the receiver. Moreover, these delays vary for different channels and signal frequencies, resulting in inter-channel and inter-frequency biases (Dhital et al 2011). Receiver-based errors can be mitigated through calibration and proper stochastic characterization.

2.2 Other Sensors

Recent personal navigation devices use several other sensors besides a GNSS receiver in order to obtain a navigation solution. The sensors that have been used for the realization of a multi-sensor integrated navigation system in this thesis are discussed below.

2.2.1 Inertial Measurement Units

An inertial measurement unit (IMU) is generally comprised of two orthogonal inertial sensor triads: an accelerometer triad and a triad of gyroscopes (El-Sheimy 2006). However, some IMUs incorporate additional inertial sensors in skewed configuration to improve reliability. An IMU also includes a processor that is responsible for functions like calibrating out many of the raw sensor errors, performing boundary checks to detect sensor failures, and converting the sensor outputs from potential difference, current, or pulses into units of acceleration and angular rate (Groves 2008).

2.2.1.1 Accelerometers

An accelerometer measures acceleration or specific force (acceleration plus gravitation) along a sensitive axis. It consists of a proof mass suspended from a case along the accelerometer's sensitive axis, restrained by a pair of springs. On application of an accelerating force along the sensitive axis, the proof mass gets displaced from its equilibrium position. This displacement, measured by a pickoff unit, is proportional to the applied acceleration. The measurement of the pickoff is eventually scaled to give an indication of acceleration along the sensitive axis (El-Sheimy 2006).

Based on the technique used to sense the acceleration along a sensitive axis, accelerometers can be classified into various types, such as pendulous accelerometers and vibrating wire accelerometers. These accelerometers may be built using either conventional mechanical construction or MEMS technology (Groves 2008). Performance of these accelerometer technologies is usually described by their bias and scale factor stability, discussed later in Section 2.4. Generally, the mechanical constructions are better in terms of performance, but are much bulkier and more expensive than their MEMS counterparts.

2.2.1.2 Gyroscopes

Gyroscopes, commonly termed as gyros, measure angular velocity with respect to an inertial frame of reference. These measurements, after removal of deterministic errors, can be transformed to any other frame of interest.

Based on their working principle, gyros can be categorized into three types: Spinning mass gyros, optical gyros and vibratory gyros. The spinning mass gyros have been around since the mid nineteenth century and are realized using mechanical construction, following principles of conservation of angular momentum. The optical gyros, however, use the Sagnac effect on counter-rotating laser beams and an interferometric phase detector to measure the relative phase changes and consequently the angular rate with respect to inertial space (Grewal et al 2001). Ring laser gyros (RLG) and fiber optic gyros (FOG) are the two fundamental types of optical gyros. Finally, the vibratory gyros detect the angular rate through the measurement of Coriolis acceleration of the vibrating element, as the gyro is rotated. Vibratory gyros are almost exclusively realized using

MEMS technology. Generally, the performance improves progressively from vibratory to optical to spinning mass gyros. However, due to such advantages as low-cost, low weight, power requirements and significant improvement in MEMS technology, vibratory gyros are now widely used in many applications, including PNDs.

2.2.2 Magnetometers

Magnetic field sensors, or magnetometers, measure the magnetic field generated by an electronic device, ferromagnetic materials or the earth's magnetic field. Magnetometers are used in a wide range of applications, like detecting anomalies in geophysical surveys or in a production line, detecting metallic objects, resolving direction (compass), etc. In navigation, magnetometers are basically used as a compass to determine the user direction through the detection of earth's magnetic field.

The magnetic field of the earth resembles the dipole field produced by a simple bar magnet, with maximum field strength at the two poles. The field can be envisioned as lines of force that leave from the magnetic North Pole and re-enter at the South Pole, making an arc parallel to the surface of the earth. The intensity of this magnetic field varies between approximately 0.25 to 0.65 gauss around the surface of earth.

Depending on the field sensing range, Caruso et al (1998) categorized the magnetic sensors into three types: low field sensors (detect magnetic fields less than 1 micro gauss), Earth's field sensors (detect fields between 1 micro gauss and 10 gauss) and bias magnetic field sensors (detect fields above 10 gauss). The magnetometers that are used in PNDs for determining direction/heading fall under the category of Earth's field sensors.

Different types of Earth's field sensors, including fluxgate sensors, magneto-inductive sensors and magneto-resistive sensors, can be used to derive a magnetic heading using Earth's magnetic field. Among these different types, the magneto-resistive sensors and, in particular, the anisotropic magneto-resistive (AMR) sensors are considered to be highly suitable for PNDs, because of features such as miniaturized structure, the ability to detect very weak fields and the possibility of mass production as an integrated circuit, as well as a very short response time, etc. (Caruso 1997). The AMR elements change their effective resistance on application of a magnetic field. The magnetic field sensed by these sensors are sensitive to the direction of the field. Hence, the vector magnetic field components sensed by an orthogonal triad of such sensors can be used for orientation estimation. This heading computation, however, is often challenged, due to the magnetic perturbations from ferromagnetic materials in the vicinity of the sensors. A detailed description of such effects is presented in Chapter 3.

2.2.3 Barometer

Barometers, also known as barometric pressure sensors or barometric altimeters, are pressure transducers designed to measure absolute ambient air pressures. The air pressure mainly changes with altitude, as well as with the variation in the weather. Due to these characteristics, barometers are often used for such varied applications as forecasting weather, indoor floor tracking, aiding information in navigation systems and obtaining elevation profiles in sport applications. In navigation, the barometer is used as an extra height observation. The pressure measurement from a barometer is converted into altitude, using the international standard atmosphere (ISA) model:

$$h = \frac{T_o}{L_g}\left(\left(\frac{P}{P_o}\right)^{\frac{-R_g L_g}{g}} - 1\right) \qquad \textbf{2-4}$$

where

h = altitude in m

P = measured pressure (Pa)

g = Earth's gravitational force (9.8 m/s^2)

P_o = standard pressure at sea level (101325 Pa)

T_o = standard temperature (288.15 K)

L_g = atmospheric temperature gradient (-6.5e-3 K/m)

R_g = ideal gas constant (287.1 J/kg/K)

The absolute height computed using the above model is often found to be erroneous, as it does not take into account the pressure changes caused by sudden changes in weather or due to wind. This is discussed in detail in Chapter 3.

Barometers can be broadly categorized into two major types; one that uses fluid (mercury, water or oil based barometers) and the other that does not use fluid (aneroid barometers). The aneroid barometric pressure sensors that are realized using MEMS technology are most common in PNDs and many other applications, due to their small size, simplicity of use and low cost. The pressure measurements in the MEMS pressure sensors can be made using capacitive, inductive or resistive (piezoresistive or pressure sensitive resistors) techniques (Bicking 1998).

2.3 NavCube

NavCube is a multi-sensor hardware platform developed in the Position, Location and Navigation (PLAN) group of the University of Calgary (Morrison et al 2012). It comprises a multi-frequency survey grade GNSS receiver, two high sensitivity GPS (HS-GPS) receivers and a HS-GNSS receiver. Besides the receivers, it also consists of various inertial sensors and has a capability to be connected to a maximum of 10 external sensor pods through two connection ports. The external sensor pods' measurements are all synchronized internally within the NavCube.

The receivers included in the NavCube are listed in Table 2.1.

Table 2.1.1: Receivers inside the NavCube

Receiver	**Signals Supported**
OEM628 (NovAtel Inc., Calgary, AB, Canada)	L1/L2 GPS/GLONASS (L5 with firmware change)
u-blox 6T (U-blox, Thalwil, Zurich, Switzerland)	L1 GPS
SiRF IV (SiRF Technology Inc., San Jose, CA, USA)	L1 GPS
Teseo II (STMicroelectronics, Geneva, Switzerland)	L1 GPS/GLONASS

The inertial sensors present inside the NavCube includes Analog Device's six degrees of freedom inertial sensors (ADIS16375), each comprising a tri-axis gyroscope and a tri-axis accelerometer. The inertial sensor is accompanied by a magnetometer triad from Honeywell (HMC5883L) and a barometer from Bosh Sensortec (BMP085). Similarly, an Analog Device's ADIS16488 inertial sensor was connected externally to the NavCube during the field tests reported later. The ten degrees of freedom inertial sensor pod includes a tri-axis gyroscope, a tri-axis accelerometer, a tri-axis magnetometer and a pressure sensor. The key specifications of the inertial sensors included in the NavCube and those connected externally are given in Table 2.2.

Table 2.2 NavCube Sensor Specifications

Sensor	**Parameter**	**Internal Sensors (ADIS16375 + HMC5883L + BMP085)**	**External Sensors (ADIS16488)**
Gyroscopes	In-Run Bias Stability (1σ)	12 °/hr	6.25 °/hr
	Angular Random Walk (1σ)	1 °/√hr	0.3 °/√hr
	Rate Noise Density	72 °/hr/√Hz RMS	23.8 °/hr/√Hz RMS
Accelerometers	In-Run Bias Stability (1σ)	0.13 mg	0.1 mg
	Velocity Random Walk (1σ)	0.076 m/s/√hr	0.029 m/s/√hr
	Noise Density	0.06 mg/√Hz RMS	0.067 mg/√Hz RMS
Magnetometers	Dynamic Range	±8 gauss	±2.5 gauss
	Resolution	2 mgauss	0.45 mgauss
Barometer	Noise	2.5 Pa RMS	3 Pa RMS

The features of the NavCube are summarized in the following sub-sections.

2.3.1 Timing

The OEM628 GNSS receiver inside the NavCube lies at the heart of time synchronization of the sensors in the NavCube. The Pulse per Second (PPS) signal from this receiver is distributed to all the sensor modules in order to synchronize them to the GPS time. Moreover, the time and data controller inside the NavCube steers the sampling train of all sensors inside the NavCube and those connected externally thus ensuring that the data sampled from various sensors are within a margin of ±100 µs.

2.3.2 Data logging

All data collected by the receivers and sensors inside the NavCube as well as those collected by the external sensors are internally synchronized and logged into an SD card for post processing.

2.3.3 Power

All the components inside the NavCube and the external sensor pods connected to it are powered using a four cell 88.8 Watt-hr lithium polymer battery pack. Once fully charged, it can support the full system along with eight external sensor pods for approximately 4.5 hours.

2.4 Inertial Sensors Error Characterization

The raw measurements of the inertial sensors are affected by various error sources. These errors degrade the accuracy of the measured observables and consequently the navigation solution. The errors are more severe in case of low cost MEMS sensors which are typically used in most of the personal navigation devices. Hence, it becomes very important to identify, characterize and mitigate the effect of these errors to the extent

possible. Both accelerometers and gyros are subject to similar types of errors. The major error components in each sensor include bias, scale factor and noise. In this regard, the specific measurement of the accelerometers and the angular rate measurements of the gyros, for the case of a sensor with three orthogonal axes, can be modeled by the following observation equations (El-Sheimy 2006, Godha 2006). El-Shiemy (2006) has modeled the accelerometer scale factor to consist of a linear and a non-linear component. However, for the grade of IMUs used in this dissertation, a simple linear model suffices.

$$\tilde{f} = f + b_a + S_g f + N_a f + \delta g + \varepsilon_a \quad \textbf{2-5}$$

$$\tilde{w} = w + b_g + S_g w + N_g w + \varepsilon_g \quad \textbf{2-6}$$

where the subscripts *a* and *g* represent accelerometer and gyro respectively,

$\tilde{f}$ is the measured specific force vector (m/s^2)

f is the true specific force vector (m/s^2)

$\tilde{w}$ is the measured angular rate (°/hr)

w is the true angular rate (°/hr)

b is the bias vector

S is a diagonal scale factor matrix

δg is the vector representing the deviation from the theoretical gravity value

N is an off-diagonal matrix representing non-orthogonality of the sensor triad

ε is the vector representing the random noise attribution of the sensor

2.4.1 Major Error Components

The errors outlined in the above inertial sensor measurement models define how much can be expected from an inertial sensor in terms of navigation performance. A brief description of these error components and methods used in a navigation filter to mitigate their effect is given below.

2.4.1.1 Bias

Bias refers to the sensor output which is present even in the absence of any input. It consists of a deterministic and a random time varying part. The deterministic part is often termed as bias offset while the stochastic part is termed as bias drift or bias instability.

The bias offset can generally be removed through calibration (Noureldin et al 2013). For a good quality IMU (navigation grade or better), the variability of the bias offset is very small and a factory calibration is good enough to remove it. However, for low cost MEMS IMUs, the bias offset values can be quite significant and their repeatability is very poor, meaning that bias offset values vary every time the IMU is turned on. For this reason, bias offset is also known as turn on bias. This turn on bias thus requires a calibration at the beginning of every data collection mission.

Similarly, the bias drift refers to a random bias component that varies throughout the run in a particular mission and is attributed due to various factors such as temperature variations, instabilities with the sensors, etc. (Titterton & Weston 2004). These time

varying error components are modeled as a random process and corrected for after estimation in a navigation filter. The characterization of the random process is discussed in Section 2.4.2.

2.4.1.2 Scale Factor

Scale factor is the ratio relating the output signal of a sensor to the physical quantity being measured. It is commonly expressed in parts per million (ppm). It is generally considered deterministic and hence is removed from the raw sensor data through calibration as in the case of the bias offset. However, sometimes it is also found to be modeled as a parameter comprised of second order deterministic components as well as a random component (Godha 2006, Titterton & Weston 2004).

2.4.1.3 Non-Orthogonality

The non-orthogonality of the sensor axes, resulting from some imperfections in the manufacturing process, causes the measurement in each sensor axis to be affected by the measurements of the other two axes. As with the scale factors, these cross-coupling errors are also generally expressed in ppm. Non-orthogonality errors can generally be calibrated using some special techniques or estimated in a navigation filter (El-Sheimy 2006).

2.4.1.4 Noise

Noise is an additional signal arising due to number of sources in the sensor itself or those due to interference from surrounding electronic equipment. The noise is more significant in low cost MEMS sensors as compared to the higher grade IMUS. The presence of noise limits the performance of inertial sensor in terms of independent operation, resolution,

dynamics etc. Noise is stochastic in nature and hence cannot be removed by the use of deterministic models. The noise in the inertial sensors is often assumed to be white, which is to say the spectral noise density is the same at all frequencies (El-Sheimy 2006). White noise in an accelerometer measurement, when integrated, is a random walk in velocity. Hence the noise component in the accelerometer measurement is usually termed as velocity random walk. Similarly, a white noise in a gyro measurement is usually termed as angular random walk. The characterization and quantization of inertial sensor noise is discussed in Section 2.4.2. Inertial sensor noise is usually expressed in terms of the roots of power spectral density (PSD). The common units for accelerometer noise are $\mu g / \sqrt{Hz}$ or $m / s^2 / \sqrt{Hz}$ and that for gyros are $^\circ / hr$ or $^\circ / hr / \sqrt{Hz}$ (Groves 2008).

2.4.2 Stochastic modeling of random errors

All the time varying random errors, including bias drift and noise, have to be modeled stochastically. Unlike in dynamic modeling where the inputs are deterministic, the inputs in the case of stochastic modeling are unobservable. So the main principle of stochastic modeling is to assume the system model to have a certain canonical form and to drive such a canonical model by white noise sources of certain strength. The stochastic model can then be obtained by computing the transfer function. In fact for a linear time-invariant system, it is possible to characterize the unknown model by just observing the output when driven by the white noise at the input (IEEE Std 647 2006).

One of the most straightforward methods of characterizing the inertial sensor error is to use the PSD. For the case of stationary processes, the two-sided PSD, $S(w)$ and covariance, $C(\tau)$ are related as

$$S(w) = \int_{-\infty}^{+\infty} e^{-jw\tau} C(\tau) d\tau \qquad \textbf{2-7}$$

However, instead of directly using the frequency domain approach like PSD, several time-domain approaches are used in practice for stochastic modeling due to simplicity. The correlation function approach is the most common approach adapted for such purpose. It is a time domain dual of the PSD method. The residual sensor error (after removal of the deterministic parts) is modeled by passing a white noise sequence through a shaping filter which changes the correlation characteristics of the input signal sequence to fit the residual error component of the inertial sensor (Nassar et al 2003). However, since an infinite length of data is required to compute autocorrelation, a major limitation of the auto-correlation method, and hence its frequency domain dual PSD method, is that usually a huge length of data is required to obtain a sufficiently accurate estimate (Brown & Hwang 1997).

For random processes which are intrinsically discrete, the auto-covariance sequences can be related to the coefficients of the difference equations of an auto regressive moving average (ARMA) process (Papoulis 1991). Several techniques have been proposed for estimating the coefficients of such a model. Nassar (2003) analyzes three such techniques and proposes a modified scheme to model inertial sensor biases as an autoregressive (AR) process. However, as with any other correlation based methods,

ARMA methods are very model sensitive and works best only with an a priori knowledge based on a model of few terms (IEEE Std 647 2006).

Another time domain analysis technique called the Allan variance method falls among the most popular approaches for characterising inertial sensor errors. This technique was originally developed to study the frequency stability of oscillators (Allan 1966). In the Allan variance method, the randomness in the data is assumed to be generated by error sources of a specific character. The magnitude of each noise sources is then estimated by inspecting the characteristic curve obtained through some operation on the entire length of data. Unlike the one-to-one mapping between the PSD and correlation based methods, the mapping from the noise spectrum to Allan variance is not one-to-one. As a result, the Allan variance doesn't always yield a unique noise spectrum. This is the main limitation of the Alan variance method. Nevertheless, the Allan variance method offers a very effective means to segregate low frequency errors from the high frequency errors. This property is very useful while modeling a system that includes both high and low frequency components. Readers are encouraged to refer to Allan (1966), IEEE Std 647 (2006) or El-Sheimy et al (2008) for further details on the Allan variance technique.

From Equation (2-5) and (2-6) as well as the discussion about the nature of errors in Section 2.4.1, it follows that there are basically two types of errors in inertial sensors, namely the slowly varying low frequency errors (eg, bias instability) and the high frequency noise (eg, velocity random walk and angular random walk). In this research, the slowly varying bias instabilities are modeled using the autocorrelation method. The autocorrelation of the empirical data was first used to identify any resemblance with some

known stochastic model. For the case of sensor bias instabilities, the autocorrelation of the residual error resembled a first order Gauss Markov (GM) process (Gelb 1974). Hence, the parameters of the first order GM model, represented by Equation (2-8), were tuned to fit the autocorrelation of the residual sensor errors:

$$\dot{x}(t) = -\beta x(t) + w_{GM}(t) \qquad \textbf{2-8}$$

where

β is the reciprocal of the time constant τ

$w_{GM}(t) = \sqrt{2\sigma^2\beta}w(t)$ is the model uncertainty with a spectral density $q = 2\beta\sigma^2$

σ^2 is the temporal variance of the process

$w(t)$ is the white noise driving the system model

Once the GM parameters are determined, the inertial sensor bias errors represented by Equation (2-8) are incorporated in the navigation filter and estimated along with other state parameters.

The high frequency noise terms (angular and velocity random walk) have much shorter correlation times as compared to the bias instabilities. These errors are characterized by a white noise process and are quantized using the Allan variance method. The spectral density thus computed are incorporated while using the inertial sensor measurements in the navigation filter.

2.5 The Kalman Filter

The Kalman filter (KF) is a Bayesian estimation technique (Bayes & Prince 1763) developed by R.E. Kalman (1960). Following the Bayesian inference technique, the KF intends to improve the statistical inference by using the prior knowledge of a system or state in addition to the observed data. Unlike classical approaches (e.g. Maximum Likelihood Estimation) where the parameter of interest is assumed to be a deterministic but unknown constant, the Bayesian techniques (e.g. KF) consider the parameter to be a random variable. Hence there is always an uncertainty associated with the estimated parameter. The KF algorithms operate in a recursive configuration wherein the state parameters predicted on the basis of prior knowledge of the system are optimally combined with the latest observations to obtain the best possible state estimate. KFs are used in a wide range of applications in various fields including biomedical engineering, positioning and localization, economic modeling, etc. A variant of KF is used in this dissertation to realize the multi-sensor integrated navigation system. This section intends to present a brief introduction to the KF technique. However, exhaustive explanations about the KF technique and the derivation of the algorithm itself can be found in such texts as Kay (2001), Brown & Hwang (1997), Grewal & Andrews (1993), etc.

A statistical filtering problem involves estimating certain parameters called states that completely define the behaviour of a system. In order to estimate these state parameters, the KF uses two sets of information; firstly, the state model that defines the time evolution of states and secondly, the measurement model that allows to observe the state parameters through some measurement data. The state model, also known as the

process or the dynamics model, basically incorporates the deterministic and stochastic properties of the state. It is developed on the basis of knowledge of the physics of the application (Maybeck 1994) and the certainty of such knowledge. In a very generic discrete time form, the state and measurement model can be expressed as:

$$x_k = f_{k-1}(x_{k-1}, u_{k-1}, \mathrm{w}_{k-1}) \qquad \textbf{2-9}$$

$$z_k = h_k(x_k, v_k) \qquad \textbf{2-10}$$

where

$x_k \in R^{n_x}$ is the state vector of order n_x at time k

u_{k-1} is the known input at time $k-1$

$z_k \in R^{n_z}$ is the measurement vector of order n_z at time k

f_{k-1} is the state function that defines the time evolution of the system states

h_k is the observation function

w_{k-1} and V_k are called process noise and measurement noise respectively representing the uncertainties in the state and measurement model.

The known input parameter u_k is often excluded from the state model as it is common in most of the applications and hence will be ignored from henceforth.

The KF combines the process information represented by Equation (2-9) with the measurements of the state parameter to generate the estimate of the state vector x_k. The KF, however, is based on the following assumptions:

1. Both the system and measurement models are linear.
2. An initial unbiased estimate of the state vector is available along with the associated uncertainty.
3. The process and measurement noise are white and uncorrelated with each other as well as uncorrelated with the state vector.

With the above assumptions, the state and measurement models can be rewritten as

$$x_k = \Phi_{k-1,k} x_{k-1} + w_{k-1} \qquad \textbf{2-11}$$

$$z_k = H_k x_k + v_k \qquad \textbf{2-12}$$

where $\Phi_{k-1,k}$ is the transition matrix of order $n_x \times n_x$ that defines how the system is going to evolve from $k-1$ to k. Similarly, H_k is the design matrix of order $n_z \times n_x$ that relates the measurements to the state vector.

The recursive KF algorithm basically comprises two stages as summarized below.

Prediction Stage

$$\hat{x}_k^- = \Phi_{k-1,k} \hat{x}_{k-1}^+ \qquad \textbf{2-13}$$

$$P_k^- = \Phi_{k-1,k} P_{k-1}^+ \Phi_{k-1,k}^T + Q_k \quad \textbf{2-14}$$

Update Stage

$$\hat{x}_k^+ = \hat{x}_k^- + K_k(z_k - H_k \hat{x}_k^-) \quad \textbf{2-15}$$

$$K_k = P_k^- H_k^T (H_k P_k^- H_k^T + R_k)^{-1} \quad \textbf{2-16}$$

$$P_k^+ = (I - K_k H_k) P_k^- \quad \textbf{2-17}$$

P is the state covariance matrix representing the uncertainty of the estimated state vector. Similarly, the covariance matrices Q and R represent the uncertainty in the state model and the measurement error covariance. The minus and plus superscripts respectively indicate the values before and after an update while the superscript T denotes transpose of a matrix. Finally, K is the Kalman gain matrix that indicates how the filter weighs between the state model and the measurements.

The KF, however, cannot be used unless modified for a majority of real world problems including GNSS, INS or any other multi-sensor integrated navigation system as they don't meet the linearity conditions of the KF. In order to handle such situations, several KF based sub-optimal techniques has been proposed in the literature such as linearized Kalman filter (LKF), extended Kalman filter (EKF), unscented Kalman filter (UKF), etc. Dhital (2010) summarized some of those techniques and compared their performance for tracking applications using both simulated and field data.

The EKF technique is one of the most commonly used estimation technique for nonlinear applications. It has a relatively much smaller computational cost compared to other techniques and performs on par with some more complex techniques as long as the degree of non-linearity is not too high. For this reason, EKF has been chosen for implementation of the navigation algorithms herein. The EKF linearizes the state and/or observation functions through a Taylor-series expansion and applies the linear KF to the model. The linearization is done around the most recent estimate of the state vector

2.6 Coordinate Frames and Transformations

Before beginning a discussion about the navigation algorithms in a multi-sensor integrated system, it is important to understand the coordinate frames in which the navigation parameters could be expressed. Hence a brief introduction about the relevant coordinate frames is presented in this section. Moreover, the transformation equations required during the implementation of the navigation algorithms presented in this dissertation are also present.

2.6.1 The Inertial Frame

An inertial frame (*i*-frame) is an ideal reference frame that satisfies Newton's laws of motion. This implies that the frame does not rotate nor accelerate, but may be in uniform linear motion. However, since a body initially at rest or moving with constant velocity will accelerate under the gravitational influence of the sun and planets thus violating Newton's first law, a more practical inertial frame is usually adopted which is defined as the Earth-centered inertial frame (ECI). Extremely distant celestial objects that have not shown any evidence of changing their relative orientation are considered as the reference in defining

the ECI. The origin of the inertial frame is defined to lie at the Earth's centre while the x-axis and y-axis lie along the equatorial plane such that the x-axis always points toward the vernal equinox and the y-axis is at 90 degrees from the x-axis in the direction of Earth's rotation. The z-axis always points along the mean rotation axis of the Earth.

2.6.2 The Earth-Centred Earth-Fixed (ECEF) Frame

The ECEF frame (*e*-frame) has its origin at the Earth's centre and all axes remain fixed with respect to the Earth. The x-axis and y-axis lie along the equatorial plane with the x-axis pointing toward the Greenwich meridian and the y-axis pointing at 90 degrees east of Greenwich meridian. The z-axis points along the Earth's axis of rotation from the centre to the North Pole. The ECEF frame rotates with respect to the ECI at a rate of approximately 15 °/hr about the z-axis. The navigation algorithms in this dissertation are implemented in ECEF.

2.6.3 The Local Level Frame (LLF)

The LLF (*l*-frame), also known as the *navigation frame* or *geodetic frame*, has its origin at the point where a navigation solution is sought for which is usually the location of GNSS antenna or the centre of inertial sensor. The x-axis points to the east and the y-axis points to the true north. The z-axis completes the right-handed coordinate system by pointing up, perpendicular to the reference ellipsoid (Noureldin et al 2013). This frame is thus also referred to as east, north and up (ENU) frame. A similar LLF that completes left-handed coordinate systems is called the north, east and down (NED) frame. This frame is subjected to a rotation with respect to ECEF as well as ECI.

2.6.4 The Body Frame

The body frame (*b*-frame) is a coordinate frame that remains fixed with respect to the object (e.g. vehicle, human, etc.) for which a navigation solution is sought. In many applications, the inertial sensor is often mounted in a way that its axes coincide with that of the body frame. The origin of the body frame coincides with that of the navigation frame. The y-axis points towards the forward direction, the x-axis points towards the right and the z-axis points up towards the vertical direction thus completing the right-handed coordinate systems.

2.6.5 Coordinate Frame Transformations

The inertial sensor outputs are measured in *b*-frame. As the navigation algorithms are implemented in *e*-frame during this research, transformation between the *b*-frame and *e*-frame is required. Moreover, some results are more intuitive when expressed in the *l*-frame. Hence a transformation between *e*-frame and *l*-frame is also relevant. In this regard, some coordinate frame transformations used during this work are summarized below. Detailed derivations of the transformations can be found in Noureldin et al (2013), Groves (2008), etc.

2.6.5.1 Transformation between the *l*-frame and the *e*-frame

The coordinate frame transformations can be represented using rotation matrices which are derived as a function of angular velocities between the coordinate frames. A transformation from *l*-frame to *e*-frame is defined in terms of the rotation matrix R_l^e

$$R_l^e = \begin{bmatrix} -\sin\lambda & -\sin\varphi\cos\lambda & \cos\varphi\cos\lambda \\ \cos\lambda & -\sin\varphi\sin\lambda & \cos\varphi\sin\lambda \\ 0 & \cos\varphi & \sin\varphi \end{bmatrix} \quad \textbf{2-18}$$

where φ and λ are the latitude and longitude of the user.

2.6.5.2 Transformation between *l*-frame and *b*-frame

The angular velocities that define the rotation of the *l*-frame with respect to the *b*-frame are associated with changes in pitch, roll and azimuth angles. Thus the rotation between the *l*-frame and the *b*-frame is computed as a function of these angles as

$$R_b^l = \begin{bmatrix} \cos A\cos r - \sin A\sin p\sin r & -\sin A\cos p & \cos A\sin r + \sin A\sin p\cos r \\ \sin A\cos r + \cos A\sin p\sin r & \cos A\cos p & \sin A\sin r - \cos A\sin p\cos r \\ -\cos p\sin r & \sin p & \cos p\cos r \end{bmatrix} \quad \textbf{2-19}$$

where p , r and A are pitch, roll and azimuth angles respectively.

2.6.5.3 Transformation between *b*-frame and *e*-frame

The transformation between the *b*-frame and *e*-frame can be obtained by simple matrix multiplication of the two rotation matrices in Equations (2-18) and (2-19):

$$R_b^e = R_b^l R_l^e \quad \textbf{2-20}$$

Finally, it is noted that the coordinate frames can be transformed back and forth by simply taking the transpose of a matrix. For instance, the rotation from the *e*-frame to the *b*-frame is given by $\left(R_b^e\right)^T$.

2.7 Multi-Sensor Integration

As discussed in Chapter 1, modern personal navigation devices combine the information from various sensors in an attempt to improve the navigation performance. The sensors in such multi-sensor systems are usually complementary in nature so that the information from one sensor helps to some extent to overcome the drawbacks of others. Inertial navigation systems (INS) lie at the heart of integrated navigation systems. An INS is defined as the combination of inertial sensors and the algorithms that compensates the sensor errors and then computes the navigation solution from the error compensated data. For a standalone INS, however, as the inertial sensor measurements are integrated to obtain the navigation solution, the sensor errors are accumulated thus increasing the navigation error. The increase in the navigation error is much rapid in case of the MEMS grade IMUs typically used in PNDs. Hence, there must be some sort of update from other sensors in order to correct the drift in the navigation solution. Moreover, since INS is a relative positioning system, it must be initialized and updated with information coming from an absolute positioning system. The integration of INS and GNSS thus forms the base of the integrated navigation system which can be supplemented through integration of other sensors to improve the performance of the navigation system.

The INS/GNSS integration can be realized using different architectures. The three main integration architectures are

1. Loosely coupled
2. Tightly coupled
3. Ultra-tightly or deeply coupled

In the loosely coupled INS/GNSS architecture, the GNSS and the INS independently compute the navigation solutions which are then fused together by an optimal estimator to improve a final navigation solution. This architecture relies heavily upon the INS solution in areas like urban canyons where the GNSS solution is often unavailable. Hence, this architecture is not suitable for systems using low cost MEMS IMUs.

A tightly coupled architecture has a more centralized structure wherein a single integration filter is employed to fuse INS and GNSS measurements. The GNSS pseudorange and Doppler measurements are combined with those predicted from INS to form an input to the centralized integration filter. This scheme provides more accurate solutions than the loosely coupled scheme because the blending of pseudorange and Doppler measurements from the two systems has more information (less correlation) than the blending of position and velocity solutions in the case of the loosely coupled scheme (Farrell & Barth 1999).

Finally, the ultra-tight scheme integrates the INS and GNSS at the GNSS tracking level itself. Although this architecture has several benefits, it is not the most preferred integration scheme in the PNDs due to the complexity of the software architecture and computations, and the necessity to access the GNSS hardware. Thus, the tightly coupled architecture has been chosen for the implementation of the integrated navigation system in this research.

The multi-sensor integrated system has been realized using a strapdown configuration wherein the sensors are attached rigidly or ‘strapped down’ to the body of the user or

vehicle (Titterton & Weston 2004). The various algorithmic stages of the multi-sensor integrated navigation are summarized in the following sub-sections.

2.7.1 Initialization

As mentioned earlier, INS is a relative navigation system and hence it needs to be initialized with position and velocity obtained from some absolute navigation system. The most commonly used source for such initialization is the GNSS. Hence the INS was initialized with a GNSS solution obtained using least squares (LS) technique (Kay 2001). Alternatively, the INS could also be initialized using a pre-surveyed position and known velocity (e.g. zero velocity knowing the user is static).

2.7.2 Alignment

Alignment is the process of computing the initial attitude of the INS. Alignment is done in two steps: computing initial roll and pitch angles through accelerometer levelling, and the initial azimuth through gyro compassing.

2.7.2.1 Accelerometer Levelling

The idea of accelerometer levelling is to compute the x and y axis rotations required to mathematically align the z-axis of the stationary IMU to the z-axis of the *l*-frame so that the gravity field is completely observed by the z-axis of the accelerometer. Such rotations along x and y axis gives the values of the roll and pitch as

$$r = \sin^{-1}\left(\frac{\overline{f}_x^b}{g}\right) \qquad \textbf{2-21}$$

$$p = \sin^{-1}\left(\frac{\bar{f}_y^b}{g}\right) \qquad \textbf{2-22}$$

where $\bar{f}_x^b$ and $\bar{f}_y^b$ are the accelerometer measurements in the body frame averaged over a period of time during the levelling.

2.7.2.2 Gyro Compassing

While stationary, the only rotation sensed by the levelled gyros is the component of Earth rotation, $w_e \cos\varphi$. Here, w_e is the angular velocity of the Earth about the z-axis in the ECEF coordinate frame. Knowing that the east component of the Earth rotation is zero, the initial heading (azimuth) can be found by rotating the IMU about its z-axis such that the east gyro component becomes zero (El-Sheimy 2006). However, in the case of the MEMS IMUs, the initial azimuth cannot be computed using gyro compassing because the gyro drift is greater than w_e in the static mode. The other option would be to use GNSS for the initial azimuth. This method, however, requires the system to be moving. The initial heading can also be computed from magnetometer. But one has to be careful about the possibility of surrounding magnetic perturbations.

2.7.3 Mechanization

Mechanization is the process of obtaining the navigation parameters (position, velocity and attitude) from the inertial sensors. The mechanization equations define how a navigation solution is obtained starting from the raw IMU data. During this research, the mechanization is realized in the ECEF frame shown as a block diagram in Figure 2-1.

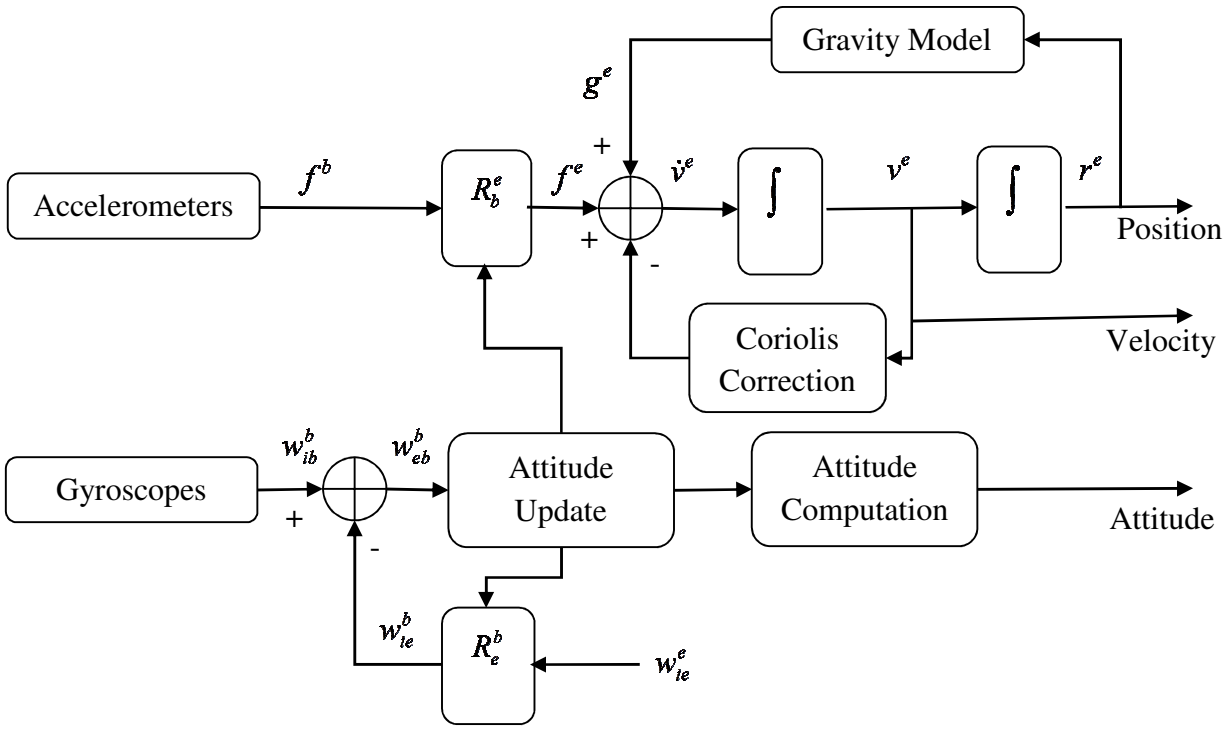

Figure 2-1. Block Diagram of INS Mechanization in ECEF Frame

.

The different steps of mechanization in the above block diagram are briefly summarized below. The text presented in this section closely follows the texts in Noureldin et al (2013), El-Sheimy (2006) and Titterton & Westen (2004). Hence, an in-depth derivation and discussion about the INS mechanization can be found in these references.

1. *Input measurement correction*: The first step in mechanization is to remove the estimated biases in the accelerometers and gyros. These biases are modeled, estimated and updated along with the other state parameters in the navigation filter. For low grade IMUs, however, other errors such as scale factors and misalignments have to be included in the state vector as well. The angular velocity

and specific force measurement after the removal of biases from the raw measurements are given as

$$w_{ib}^{b} = \tilde{w}_{ib}^{b} - b_g \qquad \textbf{2-23}$$

$$f^{b} = \tilde{f}^{b} - b_a \qquad \textbf{2-24}$$

where the subscript *ib* in w_{ib}^{b} indicates the rotation from *b* to *i* while the superscript *b* indicates that the angular velocity *w* is expressed in the *b*-frame. The same convention is followed for similar notations in the rest of this dissertation.

2. *Rotation matrix from alignment*: It follows from Equation (2-18) through (2-20) that the rotation matrix R_e^b is a function of INS attitude and the user position. Hence the position and attitude values obtained from initialization and alignment are used to obtain the rotation matrix R_e^b.
3. *Angular increments*: The body angular rates with respect to the *e*-frame is computed as

$$w_{eb}^{b} = w_{ib}^{b} - w_{ie}^{b} = w_{ib}^{b} - R_e^b w_{ie}^{e} \qquad \textbf{2-25}$$

where $w_{ie}^{e} = w_e \approx 15\,\text{deg/s}$ is the Earth rotation rate. The angular increments pertaining to the rotation of *b*-frame with respect to *e*-frame are thus obtained by multiplying the angular rate in Equation (2-25) by the time interval of mechanization Δt.

$$\theta_{eb}^{b} = w_{eb}^{b}\Delta t \qquad \textbf{2-26}$$

4. *Attitude update*: Once the angular increments are available in the *b*-frame, the corresponding attitudes are updated using the quaternions method (Kuipers 1999). This method is selected primarily because they are computationally simple and more robust against the singularity conditions. The rotation matrix R_b^e can be conveniently computed from the quaternions using a simple transformation matrix. The rotation matrix thus updated using the quaternions is used for transforming the specific force into the *e*-frame. In the subsequent cycles of mechanization, the rotation matrix R_e^b is directly obtained from the rotation matrix updated in the previous cycle instead of the values obtained from the alignment as discussed in the second step.
5. *Transformation of the specific force*: The updated rotation matrix is used to transform the specific force from the *b*-frame to the *e*-frame.

$$f^e = R_b^e f^b \qquad \textbf{2-27}$$

The velocity increment vector corresponding to the sensed acceleration in *e*-frame is then obtained by integrating this specific force over a small sampling period.

$$\Delta v_f^e = \int_{t_k}^{t_{k+1}} R_b^e(t) f^b(t) dt \qquad \textbf{2-28}$$

The rotation matrix $R_b^e(t)$ can be approximated as

$$R_b^e(t) = R_b^e(t_k)(\mathrm{I} + \mathrm{S}^b) \qquad \textbf{2-29}$$

where I is a unit matrix of order 3x3 and S^b is a skew symmetric matrix of the small incremental changes of rotation over the time interval $[t_k, t]$:

$$S^b = \begin{bmatrix} 0 & -\theta_z^b & \theta_y^b \\ \theta_z^b & 0 & -\theta_x^b \\ -\theta_y^b & \theta_x^b & 0 \end{bmatrix} \qquad \textbf{2-30}$$

where θ_x^b, θ_y^b and θ_z^b are the x, y and z components of the vector θ_{eb}^b.

6. *Coriolis and gravity correction*: The Coriolis correction involves removing the acceleration components induced due to the rotation of Earth with respect to the inertial frame. The Coriolis acceleration is represented in the *e*-frame as:

$$a_{coriolis}^e = 2\Omega_{ie}^e v^e = \begin{bmatrix} 0 & -2w_e & 0 \\ 2w_e & 0 & 0 \\ 0 & 0 & 0 \end{bmatrix} \begin{bmatrix} v_x \\ v_y \\ v_z \end{bmatrix} = \begin{bmatrix} -2w_e v_x \\ 2w_e v_y \\ 0 \end{bmatrix} \qquad \textbf{2-31}$$

Since the Earth's gravity is not uniform throughout the surface of the Earth, different gravity models has been proposed in the literature to get the gravity vector at a specific location on Earth. In this regard the gravity model proposed in Schwarz & Wei (1990) has been adapted in this work. The velocity increment of Equation (2-28) is thus corrected for the Coriolis acceleration $a_{coriolis}^e$ and the gravity vector obtained using the gravity model g^e.

$$\Delta v_f^e = \Delta v_f^e - a_{coriolis}^e \Delta t + g^e \Delta t \quad \textbf{2-32}$$

7. *Velocity update*: The INS velocity is updated as

$$v^e = v^e + \Delta v_f^e \quad \textbf{2-33}$$

where v^e is the velocity vector in the *e*-frame.

8. *Position update*: Similarly, the position is then updated as

$$r^e = r^e + v^e \Delta t \quad \textbf{2-34}$$

where r^e is the position vector in *e*-frame.

9. *Attitude Computation*: After the updated position is available, the INS attitude (roll, pitch and azimuth) can be obtained by first computing the rotation matrix R_l^e followed by computation of R_b^l as

$$R_b^l = R_e^l R_b^e \quad \textbf{2-35}$$

where, R_b^e is taken from Step 4. The attitude parameters can be computed as the arc tangents of the components of matrix R_b^l.

2.7.3.2 INS Dynamic Error Model

As discussed in Section 2.4, the inertial sensor measurements are affected by various deterministic and stochastic errors. To account for the effect of these errors in the navigation solution, it is essential to understand how these errors propagate in the navigation equations. This is represented by deriving the INS dynamic error model in the

form of a set of differential equations. An INS dynamic navigation state model in *e*-frame is given as

$$\begin{bmatrix} \dot{r}^e \\ \dot{v}^e \\ \dot{R}_b^e \end{bmatrix} = \begin{bmatrix} v^e \\ R_b^e f^b - 2\Omega_{ie}^e v^e + g^e \\ R_b^e(\Omega_{ei}^b + \Omega_{ib}^b) \end{bmatrix} \quad \textbf{2-36}$$

where Ω_{ie}^e, Ω_{ei}^b and Ω_{ib}^b are the skew symmetric forms of the angular velocities w_{ie}^e, w_{ei}^b and w_{ib}^b, respectively. The above dynamic state model leads to an INS error state model of the form:

$$\delta\dot{x}_1 = F_1\delta x_1 + F_{12}\delta x_2 \quad \textbf{2-37}$$

where

$\delta x_1 = \begin{bmatrix} \delta r \\ \delta v \\ \varepsilon \end{bmatrix}$: errors in the INS navigation parameters (position, velocity and attitude)

$\delta x_2 = \begin{bmatrix} \delta f^b \\ \delta w_{ib}^b \end{bmatrix}$: inertial sensor error state with time varying bias components (bias instabilities) in the accelerometers and the gyros

F_1 and F_{12} : dynamic matrices

Similar to the navigation error states shown in Equation (2-37), the time varying stochastic errors in the inertial sensors also need to be modeled and estimated along with other

parameters in the navigation filter. The bias instabilities in the inertial sensors are modeled using a GM model.

$$\delta \dot{f}^b = -\beta_a \delta f^b + \sqrt{2\beta_a \sigma_a^2} w(t) \qquad \textbf{2-38}$$

$$\delta \dot{w}_{ib}^b = -\beta_g \delta w_{ib}^b + \sqrt{2\beta_g \sigma_g^2} w(t) \qquad \textbf{2-39}$$

where $w(t)$ is the white process noise for the sensor error model. The subscripts *a* and *g* represent accelerometers and gyroscopes.

The composite dynamic model including the navigation states and the inertial sensor biases can be represented by

$$\begin{bmatrix} \delta \dot{x}_1 \\ \delta \dot{x}_2 \end{bmatrix} = \begin{bmatrix} F_1 & F_{12} \\ 0 & F_2 \end{bmatrix} \begin{bmatrix} \delta x_1 \\ \delta x_2 \end{bmatrix} + \begin{bmatrix} 0 \\ G \end{bmatrix} w(t) \qquad \textbf{2-40}$$

where

$$F_2 = \begin{bmatrix} -\beta_a & 0 \\ 0 & -\beta_g \end{bmatrix} \text{ and } G = \begin{bmatrix} \sqrt{2\beta_a \sigma_a^2} \\ \sqrt{2\beta_g \sigma_g^2} \end{bmatrix}$$

Modeling the errors in the form of Equation (2-40) allows propagating the uncertainties associated with each state parameter during the mechanization process. The uncertainties are represented in the form of a state covariance matrix.

2.7.4 GNSS Update

As discussed in the previous sections, the accuracy of an INS is much affected by the errors in the inertial sensors. In the case of an INS that uses low cost MEMS sensors, the output can drift rapidly making it essentially unusable for navigation. Thus, in order to improve performance, the errors in the inertial sensors must be compensated through regular updates from some external sources. GNSS is one of the most commonly used sources of update for an INS. During the course of this research, pseudorange and Doppler measurements from a GNSS receiver are used to update the INS in a tightly coupled configuration. However, the integration of GNSS measurements into the INS as an update calls for the estimation of some nuisance parameters, namely clock bias and clock drift which are modeled respectively as random walk and random constant processes (Brown & Hwang 1997).

$$\dot{cdt} = cdt + w_b \qquad \textbf{2-41}$$

$$\ddot{cdt} = w_d \qquad \textbf{2-42}$$

where

cdt : clock bias (m)

$\dot{cdt}$: clock drift in (m/s)

w_b : process noise for clock bias

w_d : process noise for clock drift

The GNSS update is implemented using the update stage equations of an EKF and have similar form as the equations (2-15) through (2-17), albeit the state parameters in this case are expressed as error terms. The linearization point however is taken as the position and velocity computed in the latest INS mechanization step. Moreover, the state covariance is also obtained from the INS mechanization step instead of the prediction stage. Thus, the INS mechanization can be thought of as a prediction stage of the EKF. With regard to the update stage EKF equations, the main parameter to derive for any update to an INS is the design matrix. In case of the GNSS, the pseudorange measurements for an i^{th} satellite given in Equation (2-1) can be expressed without the error terms as

$$\rho^i = r^i + cdT = \sqrt{(\mathrm{r}_{x,i} - r_x)^2 + (\mathrm{r}_{y,i} - r_y)^2 + (\mathrm{r}_{z,i} - r_z)^2} + cdT \qquad \textbf{2-43}$$

where

$(\mathrm{r}_{x,i}, \mathrm{r}_{y,i}, \mathrm{r}_{z,i})$: coordinates of i^{th} satellite in the ECEF frame

(r_x, r_y, r_z) : user coordinates in the ECEF frame

Equation (2-43) is linearized around $(\hat{r}_x, \hat{r}_y, \hat{r}_z)$ obtained from the mechanization step and the predicted clock bias term $c\hat{d}T$ using first order Taylor's series expansion. This results into an equation that relates pseudorange measurements to the errors in user position and the clock bias term.

$$\delta\rho^i = \frac{r_{x,i} - \hat{r}_x}{\hat{r}^i}\delta r_x + \frac{r_{y,i} - \hat{r}_y}{\hat{r}^i}\delta r_y + \frac{r_{z,i} - \hat{r}_z}{\hat{r}^i}\delta r_z + cdT = u_{x,i}\delta r_x + u_{y,i}\delta r_y + u_{z,i}\delta r_z + cdT \qquad \textbf{2-44}$$

where

$$\hat{r}^i = \sqrt{(\mathrm{r}_{x,i} - \hat{r}_x)^2 + (\mathrm{r}_{y,i} - \hat{r}_y)^2 + (\mathrm{r}_{z,i} - \hat{r}_z)^2}$$

$$\delta\rho^i = \rho^i - \hat{\rho}^i = \rho^i - (\hat{r}^i + c\hat{d}T)$$

Thus, for N satellites,

$$\begin{bmatrix} \delta\rho^1 \\ \vdots \\ \delta\rho^N \end{bmatrix} = \begin{bmatrix} u_{x,1} & u_{x,1} & u_{x,1} & 1 \\ \vdots & \vdots & \vdots & \vdots \\ u_{x,1} & u_{x,1} & u_{x,1} & 1 \end{bmatrix} \begin{bmatrix} \delta r_x \\ \delta r_y \\ \delta r_z \\ cdT \end{bmatrix} = \begin{bmatrix} H_{\rho,\mathrm{N}\times 3} & 1_{N\times 1} \end{bmatrix} \begin{bmatrix} \delta r_x \\ \delta r_y \\ \delta r_z \\ cdT \end{bmatrix} \qquad \textbf{2-45}$$

where $1_{N\times 1}$ is a matrix of order Nx1 with all elements equal to one.

Similarly, a design matrix that relates Doppler measurements to the position, velocity and the clock drift is of the form

$$\begin{bmatrix} \delta\dot{\phi}^1 \\ \vdots \\ \delta\dot{\phi}^N \end{bmatrix} = \begin{bmatrix} H_{\dot{\phi}r,N\times 3} & H_{\dot{\phi}v,N\times 3} & (1/\lambda)_{N\times 1} \end{bmatrix} \begin{bmatrix} \delta r_x \\ \delta r_y \\ \delta r_z \\ \delta v_x \\ \delta v_y \\ \delta v_z \\ c\dot{d}T \end{bmatrix} \qquad \textbf{2-46}$$

where λ is the wavelength of the GNSS signal.

Considering a full state vector that has been realized during this research, the design matrix for GNSS update takes the form:

$$H_{GNSS,N\times 18}=\begin{bmatrix} H_{\rho,N\times 3} & 0_{N\times 3} & 0_{N\times 3} & 0_{N\times 3} & 0_{N\times 3} & 0_{N\times 1} & 1_{N\times 1} & 0_{N\times 1} \\ H_{\dot{\rho}r,N\times 3} & H_{\dot{\rho}v,N\times 3} & 0_{N\times 3} & 0_{N\times 3} & 0_{N\times 3} & 0_{N\times 1} & 0_{N\times 1} & (1/\lambda)_{N\times 1} \end{bmatrix} \quad \textbf{2-47}$$

The EKF state vector $x_{18\times 1}$ comprises the following states: position error ($\delta r_{3\times 1}$), velocity error ($\delta v_{3\times 1}$), attitude error ($\varepsilon_{3\times 1}$), accelerometer bias ($\delta f_{3\times 1}$), gyro bias ($\delta w_{3\times 1}$), barometer bias ($\delta bar_{1\times 1}$), clock bias ($cdT_{1\times 1}$) and clock drift ($c\dot{d}T_{1\times 1}$).

$$x_{18\times 1}=\begin{bmatrix} \delta r_{3\times 1} & \delta v_{3\times 1} & \varepsilon_{3\times 1} & \delta f_{3\times 1} & \delta w_{3\times 1} & \delta bar_{1\times 1} & cdT_{1\times 1} & c\dot{d}T_{1\times 1} \end{bmatrix}^T \quad \textbf{2-48}$$

2.7.5 Other Updates

Besides GNSS, the multi-sensor integrated navigation system in this research also incorporates updates from other sensors and sources which are discussed in the following sub-sections.

2.7.5.1 Heading Update

The azimuth computed from magnetometer measurements serves an attitude update for the INS. The INS azimuth can be expressed in terms of the components of the estimated rotation matrix $\hat{R}_b^l$ and is given as

$$A=\tan^{-1}\left(\frac{\hat{R}_b^l(2,1)}{\hat{R}_b^l(2,2)}\right) \quad \textbf{2-49}$$

where $\widehat{R}_b^l(\mathrm{i},\mathrm{j})$ indicates an element in the ith row and jth column of the matrix $\widehat{R}_b^l$

It follows from Godha (2006) that given equations (2-35) and (2-49), the azimuth can be expressed in terms of attitude errors as

$$A = \tan^{-1}\left(\frac{N_A}{D_A}\right) = \tan^{-1}\left(\frac{n_1\varepsilon_x + n_2\varepsilon_y + n_3\varepsilon_z + n_4}{d_1\varepsilon_x + d_2\varepsilon_y + d_3\varepsilon_z + d_4}\right) \quad \textbf{2-50}$$

The numerator and denominator coefficient terms are defined as follows:

$$\begin{aligned}
n_1 &= R_e^l(1,3)R_b^e(2,2) - R_e^l(1,2)R_b^e(3,2)\\
n_2 &= R_e^l(1,1)R_b^e(3,2) - R_e^l(1,3)R_b^e(1,2)\\
n_3 &= R_e^l(1,2)R_b^e(1,2) - R_e^l(1,1)R_b^e(2,2)\\
n_4 &= R_e^l(1,1)R_b^e(1,2) + R_e^l(1,2)R_b^e(2,2) + R_e^l(1,3)R_b^e(3,2)\\
d_1 &= R_e^l(2,3)R_b^e(2,2) - R_e^l(2,2)R_b^e(3,2)\\
d_2 &= R_e^l(2,1)R_b^e(3,2) - R_e^l(2,3)R_b^e(1,2)\\
d_3 &= R_e^l(2,2)R_b^e(1,2) - R_e^l(2,1)R_b^e(2,2)\\
d_4 &= R_e^l(2,1)R_b^e(1,2) + R_e^l(2,2)R_b^e(2,2) + R_e^l(2,3)R_b^e(3,2)
\end{aligned} \quad \textbf{2-51}$$

The heading error equation can now be expressed as

$$\begin{aligned}
\delta A &= \frac{N_A n_1 - D_A d_1}{N_A^2 + D_A^2}\varepsilon_x + \frac{N_A n_2 - D_A d_2}{N_A^2 + D_A^2}\varepsilon_z + \frac{N_A n_3 - D_A d_3}{N_A^2 + D_A^2}\varepsilon_z\\
&= H_{A,1\times 3}\varepsilon_{3\times 1}
\end{aligned} \quad \textbf{2-52}$$

Thus the design matrix for heading update is given as

$$H_{Mag} = \begin{bmatrix} 0_{1\times 3} & 0_{1\times 3} & H_{A,1\times 3} & 0_{1\times 3} & 0_{1\times 3} & 0_{1\times 1} & 0_{1\times 1} & 0_{1\times 1} \end{bmatrix} \quad \textbf{2-53}$$

2.7.5.2 Height Update

A height measurement obtained from a barometer using Equation (2-4) is also used as an external height update for the INS. The height observed from the barometer is in local level frame. Hence the differential equation is of the form

$$\delta h^l = H^l_{Baro}\delta x^l \qquad \textbf{2-54}$$

Since it is a direct height observation in the *l*-frame, the design matrix for barometer is

$$H^l_{Baro} = \begin{bmatrix} 0 & 0 & 1 \end{bmatrix}$$

However, the error state should be expressed in the e-frame. Thus a transformation of the error state vector from l-frame to the e-frame is required.

$$\delta h^l = H^l_{Baro} A\delta x^e = H^e_{Baro}\delta x^e \qquad \textbf{2-55}$$

The matrix A transforms the error state vector and is given as

$$A = \begin{bmatrix} a\cos\varphi\cos\lambda - (N+h)\sin\varphi\cos\lambda & -(N+h)\cos\varphi\sin\lambda & \cos\varphi\cos\lambda \\ a\cos\varphi\sin\lambda - (N+h)\sin\varphi\sin\lambda & (N+h)\cos\varphi\cos\lambda & \cos\varphi\sin\lambda \\ a(1-e^2)\sin\varphi + N(1-e^2)\cos\varphi + h\cos\varphi & 0 & \sin\lambda \end{bmatrix}^{-1} \qquad \textbf{2-56}$$

where

a : semi major axis of Earth

$e = \sqrt{\left(1 - \frac{b^2}{a^2}\right)}$: first eccentricity

b : semi minor axis of Earth

$N = \frac{a}{\sqrt{1 - e^2 \sin^2 \varphi}}$: prime vertical radius of Earth

Thus,

$$\delta h = (a(1-e^2)\sin\varphi + N(1-e^2)\cos\varphi + h\cos\varphi)\delta x + \sin\lambda\delta z = H_{Baro}\delta r \quad \textbf{2-57}$$

where $H_{Baro} = \begin{bmatrix} a(1-e^2)\sin\varphi + N(1-e^2)\cos\varphi + h\cos\varphi & 0 & \sin\lambda \end{bmatrix}$

The time varying bias in the barometer is modeled as a random constant parameter. Considering this component, the complete design matrix for the height update is given as

$$H_{BAR} = \begin{bmatrix} H_{Baro} & 0_{1\times3} & 0_{1\times3} & 0_{1\times3} & 0_{1\times3} & 1_{1\times1} & 0_{1\times1} & 0_{1\times1} \end{bmatrix} \quad \textbf{2-58}$$

2.7.5.3 Zero Velocity Update

For pedestrian navigation, especially for the case of foot mounted IMU, an algorithm regularly checks for the zero velocity state during the stance phase when the foot is in contact with the ground (Susi 2012). Once a zero velocity state is detected, it is used as a velocity update to the INS. This is a direct observation of velocity and hence the design matrix is easily computed in the following form:

$$H_{ZUPT} = \begin{bmatrix} 0_{1\times3} & 1_{1\times3} & 0_{1\times3} & 0_{1\times3} & 0_{1\times3} & 0_{1\times1} & 0_{1\times1} & 0_{1\times1} \end{bmatrix} \quad \textbf{2-59}$$

Similar to the zero velocity update (ZUPT), another update that could be used for foot mounted pedestrian navigation is the zero angular rate update (ZARU). By analogy to

ZUPT algorithm, ZARU is based on the idea that during stance phase, foot attitude is considered constant and hence the rate of change of attitude is zero. Using such update improves the estimation of attitude angles and consequently yields more accurate navigation solution (Benzerrouk et al 2014).

Chapter Three: **Reliability of Personal Navigation Devices**

In the case of personal navigation devices that use measurements from multiple sensors to generate a navigation solution, the reliability of the navigation solution is determined by the capability of the PNDs to detect and remove faults occurring in any of the sensors. To address this issue, this chapter attempts to identify the major fault scenarios in the navigation sensors or systems used to generate the navigation solution. For personal navigation systems that are realized using low cost microelectromechanical systems (MEMS) sensors, the quality of the GNSS signals play a significant role in the navigation solution. The absence of GNSS or the presence of biased GNSS measurements can result in significant errors in the navigation solution. Considering this, the problem of reliability is categorized into two groups, one related to the quality of GNSS measurements and the other related to the faults occurring in other sensors in use. Irrespective of the categorization, the reliability of the overall navigation solution can be improved only by avoiding the use of hazardous and misleading information coming from any of the sensors in use.

3.1 GNSS Reliability Theory

The common errors occurring in GNSS measurements, as discussed in Chapter 2, can be easily accounted for by incorporating them into the stochastic model. However, the measurement outliers, arising due to satellite failure, ionosphere scintillation or multipath, result in biases in the navigation solution. Thus, detecting and removing such measurement outliers is important. The most common approach adapted over the years

in order to detect and remove faults or outliers in GNSS measurements is to use the RAIM (receiver autonomous integrity monitoring) technique. As the name suggests, RAIM attempts to detect the presence of and remove any errant satellite measurement through self-consistency checking among the available measurements and without any sort of aid from external sources. RAIM, however, requires a certain degree of measurement redundancy to effectively isolate and remove the outliers. A RAIM architecture is based on statistical detection theory and involves hypothesis testing in order to detect faulty satellite measurements. Two statistical tests are conducted, first to detect if there is an occurrence of a fault followed by a second test to identify the particular satellite with the fault. Both of these tests include two hypotheses, a null hypothesis (H_0) that states there is no fault and an alternate hypothesis (H_a) for a situation with a fault. Both of these tests, however, are based upon certain assumptions. As with any statistical testing method, RAIM inherently requires a known or assumed measurement error distribution. For a system implemented using a Kalman filter, both the process model as well as the measurement errors are generally assumed to be zero-mean, white and Gaussian distributed.

The first test, which intends to detect the presence of a single faulty measurement, is often termed a global test. The global test requires at least one redundant measurement, in order to be able to detect the fault. One of the most common statistical methods adapted for this test is the variance factor test (Vanícek & Krakiwsky 1986). The measurement covariance matrix R is often expressed as

$$R = \sigma_0^2 Q_R \qquad \textbf{3-1}$$

where σ_0^2 is the *a priori* variance factor and Q_R is the co-factor matrix of R. If the variance factor is unknown, the best approximation can be obtained by computing the *a posteriori* variance factor given by

$$\hat{\sigma}_0^2 = \frac{v^T Q_R^{-1} v}{n - m} \qquad \textbf{3-2}$$

where n is the number of satellite measurements, m is the size of the state vector x_k and v is the innovation vector denoted as

$$v = z_k - H_k \hat{x}_k^- \qquad \textbf{3-3}$$

Assuming a known *a priori* variance factor, the variance factor test compares the *a priori* variance factor to the *a posteriori* variance and thus the null hypothesis H_0 is that $\hat{\sigma}_0^2 = \sigma_0^2$. The corresponding test statistic, ξ, can be shown to be of the following form:

$$\xi = v^T R^{-1} v \qquad \textbf{3-4}$$

For Gaussian distributed errors and consecutively Gaussian distributed innovations, the test statistic ξ attains a chi-squared (χ^2) distribution with $n - m$ degrees of freedom. The hypothesis testing is then conducted as follows (Leick 2004):

$$H_0\ (No\ fault): \chi^2_{\alpha/2} > \xi > \chi^2_{1-\alpha/2} \qquad \textbf{3-5}$$

$$H_a\,(Fault): \chi^2_{\alpha/2} < \xi \text{ or } \xi < \chi^2_{1-\alpha/2}$$

where α is the significance level, representing the probability of rejecting the null hypothesis H_0 when H_0 is actually true. This is often termed a Type I error.

If a fault scenario is detected through the global test, a second test, commonly termed as a local test or blunder detection, is performed to identify the faulty measurement. This test requires the presence of at least two redundant measurements. Again, assuming a known σ_0^2, hypotheses are tested for individual standardized innovations, given as

$$\gamma_i = \frac{M_i^T C_v^{-1} v}{\sqrt{\left(C_v^{-1}\right)_{ii}}} \qquad \textbf{3-6}$$

where $M_i = \begin{bmatrix} 0 & \cdots & 0 & 1 & 0 & \cdots & 0 \end{bmatrix}^T$ has 1 at the ith column (corresponding to the ith satellite measurement being tested) and 0 elsewhere, and C_v is the innovation covariance matrix given by

$$C_v = HP^- H^T + R \qquad \textbf{3-7}$$

where H and P^- represent the design matrix and predicted state covariance matrix, as defined in Chapter 2. Now, the null hypothesis is that the standardized innovation is distributed normally, with zero mean and unity variance, while the alternate hypothesis states that it is distributed normally with a non-zero mean and unity variance. The respective hypotheses are accepted or rejected based on the following comparison:

$$H_0(\textit{No blunder}) : |\gamma_i| < N_{1-\alpha_0/2}$$
$$H_a(\text{B}\textit{lunder}) : |\gamma_i| \geq N_{1-\alpha_0/2} \qquad \textbf{3-8}$$

Although the significance level of the local test (α_0) can be different from that of the global test, its selection may not be independent from α. The parameter α_0 must be related to α as well as to the probability of missed detection, β, which is the same for both the tests. The parameter β represents the probability of accepting the hypothesis H_0 when it is actually false. Such a failure situation is termed a Type II error. Parameters α and β are commonly defined as a function of application requirements. The parameter α_0 is then derived, based on its relation to the other two parameters.

Often, a blunder in one of the satellite measurements results in an increase in standardized innovations corresponding to other satellite measurements, thus causing them to exceed the threshold. In such a scenario, to avoid removing a good measurement instead of the measurement with the actual blunder, the measurement with the largest standardized innovation exceeding the threshold is identified as the blunder and excluded during the computation of the navigation solution.

The FDE (fault detection and exclusion) scheme presented above (comprised of the global and local tests) is widely adopted for removing faults in GNSS measurements and, hence, it will be considered to be the benchmark against which the novel FDE scheme proposed in Chapter 4 will be compared when it is assessed.

Besides detecting and removing the outliers, RAIM is also used to provide integrity information that indicates the maximum size of the blunder that can go undetected and its effect on the navigation solution. This information is quantized in the form of internal and external reliability parameters (Baarda 1967). Such applications as aviation usually define a theoretical boundary in terms of an external reliability value, beyond which the solution is deemed unreliable.

The information about the integrity of individual satellite measurements (primarily the range measurements) can also be obtained through local area ground based augmented systems (LBAS) or regional satellite based augmented systems (SBAS). The SBAS are more common as they are usually available for all GNSS users in the region of availability. SBAS monitors the health of satellites through the use of a network of ground based monitoring stations. The integrity information is then uploaded onto the SBAS satellites for transmission to the users. Some of the commonly used SBAS include wide area augmentation system (WAAS), European geostationary navigation overlay service (EGNOS) and GPS aided geo augmented navigation (GAGAN).

Many personal navigation applications do not specify any requirements in terms of an external reliability boundary. Moreover, when realized as a multi-sensor integrated navigation system, the overall integrity of the navigation solution is also dependent upon other sensors. Hence, the integrity information in these applications is not very relevant. Nevertheless, the reliability of the navigation solution is still a very important parameter for many personal navigation applications. In the context of this thesis, reliability is thus defined as the capability of the navigation system to give a solution with proper estimated

accuracy and is formulated as the percentage of errors bounded by $\pm 3\sigma$ or 99.7% (three times the estimated standard deviation of the position or velocity solution along a particular axis envelope). For example, if a navigation system estimates a position with accuracy (1σ) of 5 m along a particular axis, then it means that the error along that axis is expected to be less than 15 m with a confidence of 99.7% (i.e., 3σ along that axis). However, as shown in Figure 3-1, if the true position along that axis is 20 m away from the estimated position, then the navigation solution is considered unreliable.

The above definition of reliability is thus different from the internal and external reliability parameters that were introduced by Baarda (1967). Such quantization of reliability provides a means to assess how well a navigation system or a navigation algorithm performs in terms of consistency between the estimated navigation solution and the associated estimated accuracy. Thus, if a navigation system gives a solution such that the estimated position is within three times the estimated standard deviation of the position along a particular axis for 800 out of 1,000 time epochs, then the reliability of the navigation system along that particular axis is said to be 80 %.

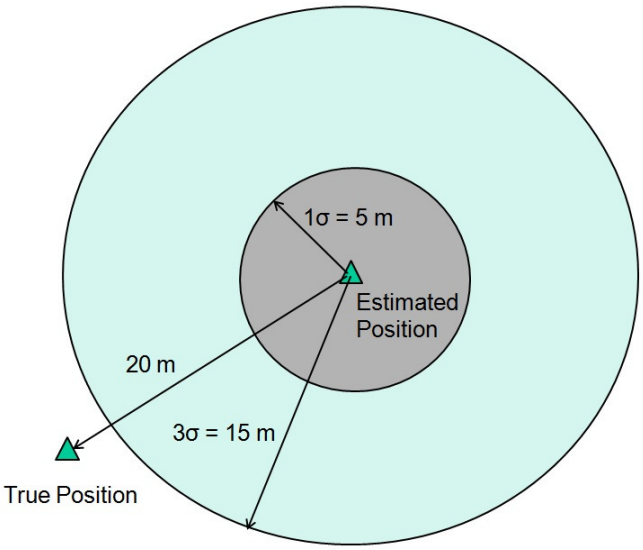

Figure 3-1: Example of an Unreliable Position Solution

As discussed in Section 1.2.1, degraded GNSS signal environments present unique conditions that cannot be appropriately addressed by traditional RAIM techniques. Thus, in order to improve the reliability of the navigation solution in the presence of biases and noise in the GNSS measurements, a more robust RAIM technique is required that overcomes the limitations and drawback of the prevalent techniques.

3.2 Faults in other navigation sensors

Besides GNSS, the presence of outliers in the measurement made by any other navigation sensors can result into the deterioration of the navigation solution. In order to obtain a reliable navigation solution, the navigation algorithm should also be able to detect, identify and remove faults occurring in other sensor measurements used to obtain

the final solution. The following sub-sections briefly discuss some of the possible fault scenarios in those sensors used during the research.

3.2.1 Faults in Magnetic Field Sensors

Magnetic field sensors have been used for a long time to derive magnetic headings, by using Earth's magnetic field. However, in the case of low cost magnetic field sensors, commonly used in personal navigation devices, the heading computation is often challenging, due to the faults occurring in the magnetic field measurements. These faults primarily are caused by the magnetic perturbations from ferromagnetic materials in the vicinity of the sensor or due to the imperfections in the calibration parameters.

3.2.1.1 Magnetic Perturbations

Magnetic perturbations result from any magnetic sources other than the Earth's magnetic field and are the major cause of faults in magnetometers. The magnetic perturbations are not explicitly due to the magnetic field sensor itself. However, for the application in hand, the magnetic field measurements arising from any other sources other than the Earth's geomagnetic field are interpreted as interference that gives rise to the faults. Based on the source of magnetic field generation, such perturbations can be primarily divided into two types, namely hard and soft iron errors. Hard iron errors occur due to a permanent magnetic field, generated by a permanent magnet or some electronic sub-systems near the sensor. Similarly, soft iron errors occur due to the generation of magnetic fields by ferromagnetic materials. These fields are mainly induced by the Earth's magnetic field. Magnetic perturbations are commonly found when navigating in urban areas and indoors, due to the abundance of perturbing sources in those environments. Figure 3-2 shows an

example of the total magnetic field using data collected in an urban area. It can be observed that the field is noisy and contains a large number of spikes that correspond to the magnetic perturbations in the test area. The black horizontal line indicates the ideal total magnetic field in the test area in the absence of perturbing sources.

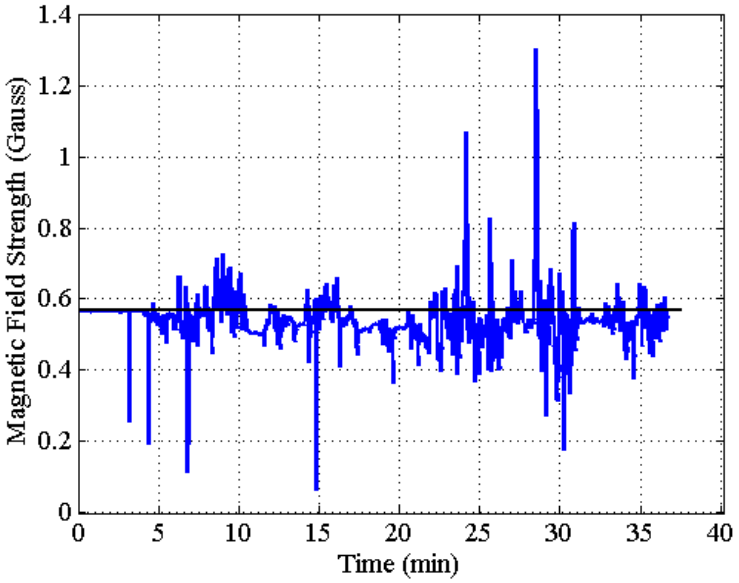

Figure 3-2: Total Magnetic Field in Urban Area

If the significantly perturbed magnetometer measurements are incorporated in the form of heading updates when computing the navigation solution, it is more likely to degrade the navigation solution than to improve it.

3.2.1.2 Calibration of Magnetic Field Sensors

The raw magnetometer data is contaminated by the magnetic field perturbations coming from sources (hard and soft iron) in and around the host platform. These measurements are also affected by such instrumentation errors as scale factors, non-orthogonality and

bias offsets. Hence a calibration algorithm is required to estimate and compensate for these deterministic errors, before the measurements are used for computing the navigation solution. Correspondingly, various calibration methods have been introduced in literature. One group of these calibration techniques relies on external reference information, such as the exact orientation of the earth's magnetic field or a reference heading from some other source (Jirawimut et al 2003). However, such external information may not be available for many applications. A second group of calibration techniques does not rely on such external reference (Caruso 1997, Gebre-Egziabher et al 2006). But these methods ignore or simplify some of the error sources in order to reduce the complexity. Finally, a third category of calibration techniques are available which are more rigorous and complete. Most of the methods under this category perform the calibration by solving the ellipsoid fitting problem (Dorveaux et al 2009, Renaudin et al 2010). These methods are based on the fact that the locus of clean tri-axis magnetometer measurements forms a sphere that transforms into an ellipsoid in the presence of errors. The goal of the calibration technique is thus to transform the ellipsoid into a sphere with proper origin and radius. This requires redundant measurements of magnetic field in a wide range of orientations. The method proposed by Renaudin et al (2010) uses an adaptive least-squares estimator to provide a solution to the ellipsoid fitting problem and derives the calibration parameters in the process. This algorithm requires no external information, other than the true magnitude of the magnetic field being measured. The same method has been adapted during this dissertation for the calibration of raw magnetometer data. The drawback of this method, however, is that it requires the user to rotate the device around each axis to observe the entire locus. It is also

computationally very intensive and is not suitable for on the fly calibration of the magnetometer in portable devices. Some recently proposed methods (Fang et al 2011, Tabatabaei et al 2013) claim to achieve calibration accuracy on par with the intensive ellipsoid fitting methods, but with much less complexity.

The adapted calibration algorithm is still prone to some errors, due to the presence of perturbations from sources other than the host platform during calibration or some possible imperfections in the error modeling. This can lead to a situation where the errors may exist in different axes of the magnetometer measurements, despite having a proper total magnetic field. Such situation can lead to errors in the heading computation.

3.2.2 Faults in Barometers

The height computed using the ISA model in Equation (2-4) is often found to be erroneous, as it does not take into account local pressure changes caused by reasons other than the change in altitude itself. The atmospheric pressure can change significantly over a very short duration (e.g. before a heavy rainfall). The barometer interprets this as a change in altitude; and, if not corrected, it can degrade the navigation solution. Such errors can be mitigated to a good extent by using differential barometry wherein a differential height information is used by placing a barometer at a base location with known elevation. The use of differential height information cancels out the effect of change in the local atmospheric conditions. The accuracy of the differential height depends on the proximity of the remote barometer to the base (McLellan et al 1994). Other common fault scenarios in barometers occur due to pressure variations generated by wind gusts.

To investigate the effect of pressure generated by wind, often termed as wind loading, barometric data was collected using two digital pressure sensors from Bosch Sensortec (BMP085 and BMP180). One set of data was collected during a low wind condition, while the other set of data was collected during a higher wind event. The wind, as measured by a Kestrel wind meter (Kestrel 4200 Pocket Air Flow Tracker), varied between 15 km/h and 40 km/h. For both data sets, the reference altitude was obtained as a double differenced carrier phase solution, using geodetic grade receivers and antennas at both the rover and base station.

Assuming a static atmospheric condition, the error in the barometer reading can be modeled as

$$\varepsilon(t) = b_{initial} + b_{wind}(t) + n(t) \qquad \textbf{3-9}$$

where $b_{initial}$ is the bias introduced by instrument errors, b_{wind} is the error introduced by the presence of wind and n is the stochastic noise component. The component $b_{initial}$, however, will be different for the two sensors in use as their instrument errors are different. Similarly, $b_{wind}(t)$ will also be different for the two sensors due to various factors, e.g. difference in the casing and sensor locations.

Further, removing the initial offset in the barometer derived altitude measurements, the residual error can be represented as

$$\varepsilon_{residual}(t) = \varepsilon - (h_{sensor}(t_0) - h_{ref}(t_0)) \qquad \textbf{3-10}$$

where h_{sensor} is the altitude obtained from the pressure sensor using Equation (2-4), t_0 is the start time and h_{ref} is the reference altitude. Ignoring the noise term, the difference $h_{sensor}(t_0) - h_{ref}(t_0)$ gives the initial instrumentation bias and the bias due to wind at time t_0. Thus the residual error can be rewritten as

$$\begin{aligned} \varepsilon_{residual}(t) &= \varepsilon - (b_{initial} + b_{wind}(t_0)) \\ &= b_{initial} + b_{wind}(t) + n(t) - (b_{initial} + b_{wind}(t_0)) \\ &= b_{wind}(t) - b_{wind}(t_0) + n(t) \end{aligned} \qquad \textbf{3-11}$$

The residual altitude errors computed for the data set obtained during high wind conditions are plotted in Figure 3-3. The blue and red dotted lines show the altitude errors for the two pressure sensors. The variations ranged between 5 and 10 m. The wind meter showed that the speed of the wind was maximum at the top of the 2,200 m high mountain where the data was collected and decreased along the lower parts of the ridge leading to the summit, indicating proportionality to the wind speed.

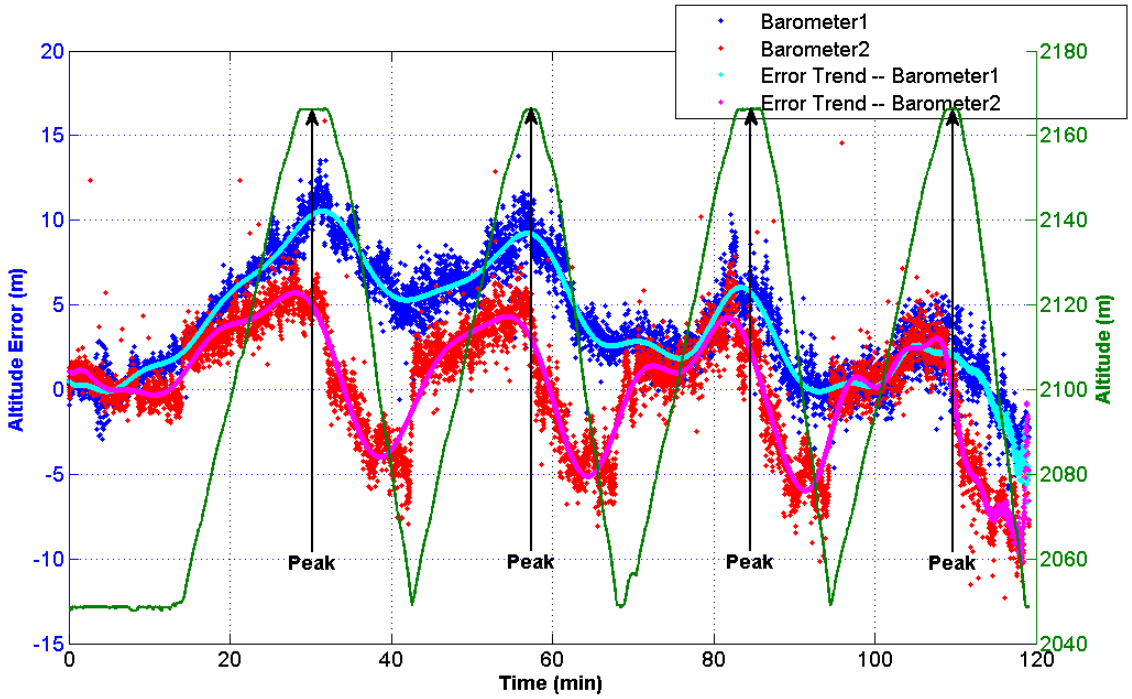

Figure 3-3: Altitude Error during High Wind Condition

To analyze the effect of wind on the stochastic part of the error, a high order polynomial fit was then obtained to estimate the error trend as plotted alongside the residual error values in the above figure. The variance of the barometer data was then observed, after removing the error trend (ε_{trend}). The estimate of the stochastic noise component was then obtained by removing this error trend from the residual error as

$$\tilde{n}(t) \approx \varepsilon_{\text{residual}}(\text{t}) - \varepsilon_{\text{trend}} \qquad \textbf{3-12}$$

The stochastic nature of the noise, estimated by using the equation introduced above, was analyzed by plotting the histogram of the noise component for one set of barometric data (Barometer 2). From the histogram depicted in Figure 3-4, it can be observed that

the barometric noise distribution closely follows a normal distribution, as indicated by its coherence with the normal fit plotted in red.

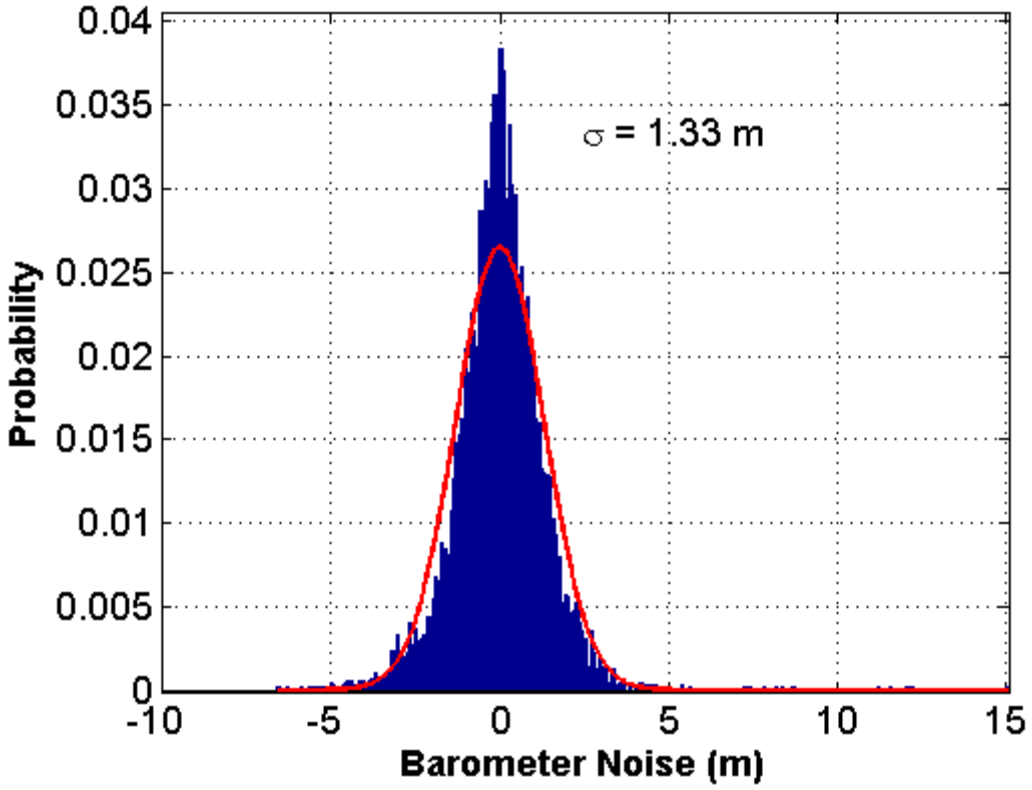

Figure 3-4: Histogram of Barometer Noise during Windy Condition

Moreover, the variance was observed to be slightly higher during high winds as compared to the variance obtained during low wind conditions, as indicated in Table 3-1. The increase in variance was higher in the case of Barometer 1, which was fully exposed to the west wind, as compared to Barometer 2, which was in a pocket. Although the variance differences are not significant, the biases shown in Figure 3-3 are, which is the most critical.

Table 3-1. Barometric Noise during Different Wind Conditions

	$\sigma_{Barometer1}$ (m)	$\sigma_{Barometer2}$ (m)
Low Wind	0.7	1.1
High Wind	1.2	1.3

From the above analysis, it can be concluded that the wind generated pressure not only leads to significant dynamic biases in the barometer derived altitude, but also increases the noise of the barometer data.

To further investigate possible fault scenarios in a barometer, pressure data was logged using a commercial “GPS unit”. Garmin’s Forerunner 910xt watch was used to collect the pressure data, while GPS was turned off. The pressure data collected during a hike of over six hours showed some large jumps in the pressure even during low wind conditions. This could likely be attributed to the response of the low cost pressure sensor to the user dynamics. The jump in the recorded pressure was more than a 100 m at one instance, as seen in Figure 3-5; where the barometer derived altitude obtained using the 910xt watch is compared to the altitude obtained from Garmin’s 64st receiver (a high-sensitivity GPS and GLONASS receiver with barometer).

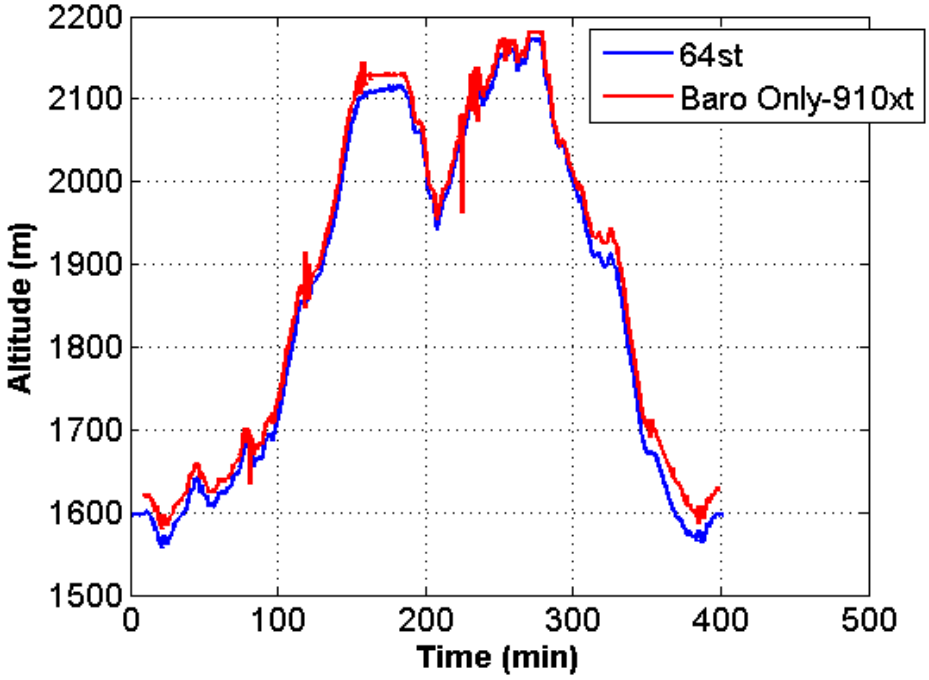

Figure 3-5: Altitude Profile for two Receiver Units

Thus, having identified various fault scenarios in typical pressure sensors used in the PNDs, it can be concluded that a navigation filter, performing a height update using barometer data, must incorporate a fault detection and exclusion scheme to prevent the effect of such faults in the navigation solution.

3.2.3 MEMS Inertial Sensor Faults

As with other self-contained sensors, inertial sensors (comprising triads of accelerometers and gyroscopes) that are realized using microelectromechanical systems (MEMS) technology are preferred in PNDs, due to their ultra-small size, low cost and lower power consumption. Errors such as bias, scale factor, non-orthogonality and noise are more severe in these sensors, as compared to those of their mechanical counterparts.

Thus, these errors have to be characterized properly and often need to be estimated along with other navigation parameters. However, apart from these errors, MEMS inertial sensors also often suffer from unexpected faults that cannot be modeled in a navigation filter.

One such failure situation is caused by deviation from the initial factory temperature calibration. This is more likely to happen with an inertial sensor that has been used for a few years, due to aging.

Other failure situations include stiction effects, which are more detrimental. Stiction or static friction is caused by adhesion of a microstructure to the adjacent surfaces when restoring forces are unable to overcome such interfacial forces as capillary forces, hydrogen bridging, electrostatic forces and van der Waals forces (Kolpekwar et al 1998, Tas et al 1996). For instance, a proof mass in an accelerometer can get “stuck” on the substrate due to a strong adhesive force resulting from surface interaction. Stiction could occur either during fabrication or while in use. In use stiction is more likely to occur during high humidity and temperature conditions or during high dynamics and jerk. Stiction can result in spurious measurement output or often railed measurements and thus if not detected can seriously compromise the navigation solution.

Chapter Four: **Design of a Filtering Strategy for Challenged Environments**

As discussed in Chapter 1, areas such as urban and natural canyons offer very harsh conditions for GNSS due to the presence of multipath, high noise and signal blocking. In those environments, the FDE schemes based on the conventional RAIM techniques are found to be inferior in handling large GNSS errors, often occurring simultaneously in multiple satellite measurements, mainly due to incorrect assumption about the error distributions. The inconsistency between the assumed and the true error statistics often leads either to removal of good measurements by the FDE or to improper weighting of each measurement. Removing a good measurement in environments where GNSS signals are already depleted not only degrades the navigation solution but can also make the FDE scheme unavailable due to lack of sufficient redundancy.

Thus, with an ultimate goal of improving the reliability of personal navigation systems in GNSS challenged environments, some novel statistical filtering techniques are proposed in the following sections. The fundamental strategy that has been followed is to make the assumed GNSS measurement error statistics as close as possible to the true one. In this regard, two approaches have been adopted herein to address two major challenges faced by the FDE schemes in harsh environments, namely non-Gaussianity and varying error statistics.

4.1 Student's t-Distribution for GNSS Measurement Errors

In the Bayesian framework, the influence of measurement outliers on inference for estimates, including population means and medians, can be reduced by replacing the normal distribution model by a heavy tailed distribution. Such heavy tailed distributions allow for the possibility of high noise and possibly biased observations. These distributions treat observations far from the regression line as high variance observations, yielding results similar to those obtained by deweighting the outliers (Gelman et al 1995). This, to a certain extent, avoids having to reject measurements because of incorrect error modeling. Moreover, in the case of GNSS measurement errors occurring in environments like urban canyons where a significant proportion of measurements could be affected by multipath, a heavy tailed distribution is likely to be more representative of the true errors than the normal distribution, thus leading to more precise test statistics and hence a better FDE. This was examined by plotting the cumulative density function (CDF) of approximate range errors of all available GNSS measurements for a data collected in a typical urban area. The range errors were computed following the procedure described in Appendix A. The mean of the range errors was approximately zero while the standard deviation was computed to be 9.6 m. The high variance is attributed to the presence of large measurement error which will either be rejected or significantly de-weighted. A more practical value of assumed GNSS accuracy falls around 5 m. Hence, Gaussian distributed samples were simulated with zero mean and standard deviation value of 5 m. Moreover, samples were also simulated with an equivalent heavy tailed distribution (Student's t-distribution). The CDFs for the two simulated cases were plotted along with the CDF of the range error data mentioned above. From these CDF plots in Figure 4-1 and the

zoomed version in Figure 4-2, the heavy tailed distribution is observed to be a closer approximation to the range error data in urban canyon. It is specifically noted that the Gaussian CDF underestimates the frequencies in the tails of the true distribution.

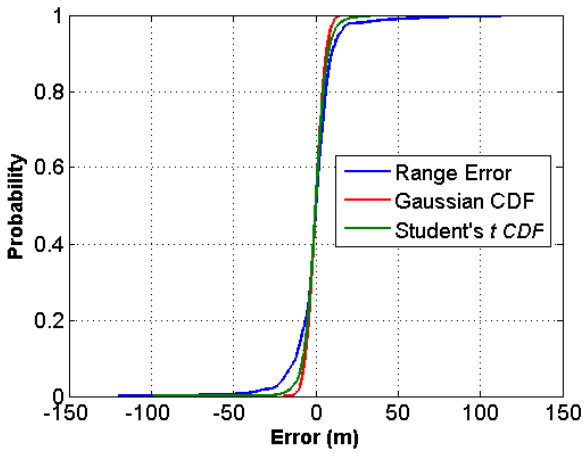

Figure 4-1: Empirical CDF of Range Error

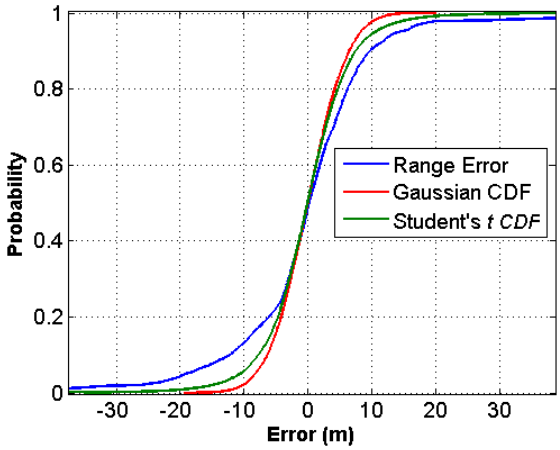

Figure 4-2: Empirical CDF of Range Error (Zoomed)

The assumption of a heavy tailed measurement error distribution in the Kalman filter implementation can be described in terms of the changes occurring in the Bayesian framework. The process noise in the prediction stage is still assumed to follow a Gaussian distribution. But the measurement errors are now assumed to follow the Student's t-distribution, or simply *t* distribution, instead of the Gaussian distribution. The use of the *t* distribution for GNSS measurement errors, however, makes the filtering problem intractable, as the functional measurement model that appears in the form of a likelihood function and transition density in the Bayesian framework (Kay 2001) does not reduce to a closed form solution as in the case of Gaussian distributed errors. Two techniques are

available to implement the filtering algorithm with such a distribution. One option is to use Monte Carlo techniques such as particle filters (Arunlampalam et al 2002). However, these techniques are computationally very demanding and are not preferred in most of the commercial products. Hence, a computationally effective option is chosen for the implementation of the filter with a *t* distribution. This method expresses the *t* distribution as a Gaussian mixture through the introduction of an auxiliary random variable λ. The measurement error distribution is thus expressed as

$$p(y_k \mid \mathrm{x}_k) = \int p(y_k \mid x_k, \lambda_k) p(\lambda_k) d\lambda_k \qquad \textbf{4-1}$$

where y_k is the measurement vector of dimension d, x_k is the state vector, $y_k \mid x_k, \lambda_k$ follows a Gaussian distribution (i.e. $y_k \mid x_k, \lambda_k \sim N\left(h(x_k), \frac{1}{\lambda_k} R_k\right)$) and λ_k follows a Gamma distribution (i.e. $\lambda_k \sim \Gamma\left(\frac{\vartheta}{2}, \frac{\vartheta}{2}\right)$). The parameter ϑ is the degree of freedom that determines the Kurtosis (heavy tailedness) of the *t* distribution. The heaviness of the tail of the *t* distribution increases with a decrease of ϑ. It has been found, in many applications, that $\vartheta = 4$ gives a reasonable heaviness in the tail of the distribution (Lange et al 1989) and hence the same value is adopted during this dissertation.

In order to make the computation of the resulting posterior density function tractable, the standard Variational Bayes (VB) technique is followed; wherein, the posterior probability density function (probability associated with the parameter of interest, given the observations) is approximated by the product of two probability densities.

$$p(x_k, \lambda_k \mid z_k) \approx q(x_k) q(\lambda_k) \qquad \textbf{4-2}$$

Again, the density $q(\lambda_k)$ follows a Gamma distribution, albeit with different parameters, and $q(x_k)$ is approximated with a Gaussian distribution with covariance $\frac{1}{\lambda_k} R_k$. The VB approximation minimizes the Kullback-Leibler (KL) divergence between the product approximation and the true posterior density function, following the calculus of variations. As the variational parameters of $q(\lambda_k)$ and $q(x_k)$ are coupled, they are solved through fixed point iteration, resulting into an algorithm of the following form (Piche et al 2012):

Algorithm : VB Filter

---

begin

$m_k^- \leftarrow \int f(x_{k-1}) N(x_{k-1} \mid m_{k-1}, P_{k-1}) dx_{k-1}$

$P_k^- \leftarrow \int (f(x_{k-1}) - m_k^-)(f(x_{k-1}) - m_k^-)^T N(x_{k-1} \mid m_{k-1}, P_{k-1}) dx_{k-1} + Q_k$

$\bar{\lambda} \leftarrow 1$

for k from 1 to M do

$\mu_k \leftarrow \int h(x_k) N(x_k \mid m_k^-, P_k^-) dx_k$

$S_k \leftarrow \int (h(x_k) - \mu_k)(h(x_k) - \mu_k)^T N(x_k \mid m_k^-, P_k^-) dx_k + \frac{1}{\lambda_k} R_k$

$C_k \leftarrow \int (x_k - m_k^-)(h(x_k) - \mu_k)^T N(x_k \mid m_k^-, P_k^-) dx_k$ **4-3**

$K_k \leftarrow C_k S_k^{-1}$

$m_k \leftarrow m_k^- + K_k (y_k - \mu_k)$

$P_k \leftarrow P_k^- - K_k S_k K_k^T$

$D_k \leftarrow \int (y_k - h(x_k))(y_k - h(x_k))^T N(x_k \mid m_k, P_k) dx_k$

$\bar{\gamma}_k \leftarrow tr(D_k R_k^{-1})$

$\bar{\lambda}_k \leftarrow \frac{\vartheta + d}{\vartheta + \bar{\gamma}_k}$

end for

end

---

where M is the number of VB fixed-point iterations.

The numerical integrations, corresponding to the measurement update stage, in the above algorithm are computed using the Cubature rule (Arasaratnam & Haykin 2009).

Despite using the *t* distribution for measurement errors, some form of FDE is still needed in order to account for gross errors. Hence, a FDE technique similar to the one used for Gaussian distributed measurement errors has been used. Due to the symmetry of the *t*

distribution, the test statistic for a local test assumes the same form as that for the normal distribution (Vanicek & Krakiwsky 1986), namely

$$\xi = \frac{r_i}{\sqrt{(C_r)_{ii}}} \qquad \textbf{4-4}$$

The threshold (Th) is, however, derived from the t distribution, $Th = t(\vartheta, 1-\alpha_t)$. The parameter α_t is the probability of false alarm for the t distribution and is commonly a design parameter.

4.2 Adaptation of GNSS Measurement Covariance

The navigation filters in personal navigation devices usually make an *a priori* assumption of the measurement covariance of the sensors being used. For a relatively good MEMS IMU, like the one used in this work (see Chapter 2.3), the stochastic characteristics of the measurement errors can be considered constant. However, the same does not apply for the case of GNSS measurements. For instance, the measurement covariance of a non-line of sight (NLOS) GNSS measurement is most likely to increase as the user moves into a deep canyon environment or on city streets due to multipath and low signal strength. Hence, a fixed *a priori* covariance for GNSS measurements in harsh environments will not correctly represent the true error characteristics of GNSS measurements. Hence, some adaptive technique must be used to continually tune the measurement covariance of GNSS measurements. Several techniques have been proposed in the literature to adapt the GNSS measurement covariance to changing signal conditions. These techniques however come with several drawbacks, including filter instability, divergence,

computational complexity or poor accuracy (Almagbile et al 2010, Hide et al 2002). Hence, in order to adapt the GNSS measurement variances with the changing signal conditions and considering the drawbacks of the prevalent adaptive techniques, a new technique is proposed in this work. This method scales the *a priori* variance of the GNSS measurements before they are fed to the navigation filter while avoiding various drawbacks of the earlier adaptive techniques.

The proposed method computes the user acceleration from GNSS Doppler measurements and compares its consistency with that obtained from accelerometers in the IMU. With a tactical grade MEMS IMU, the user acceleration obtained using accelerometers is fairly accurate and hence is taken as a reference to compare with that obtained from GNSS Doppler measurements. Thus, during good GNSS signal conditions, the two accelerations are highly consistent whereas in GNSS signal degraded environments, the consistency between the two accelerations degrades. Based on this characteristic, a scaling factor is computed to scale the assumed covariance of GNSS measurements thus adapting it in accordance with the changing GNSS signal conditions. A top level block diagram of the proposed method is depicted in Figure 4-3.

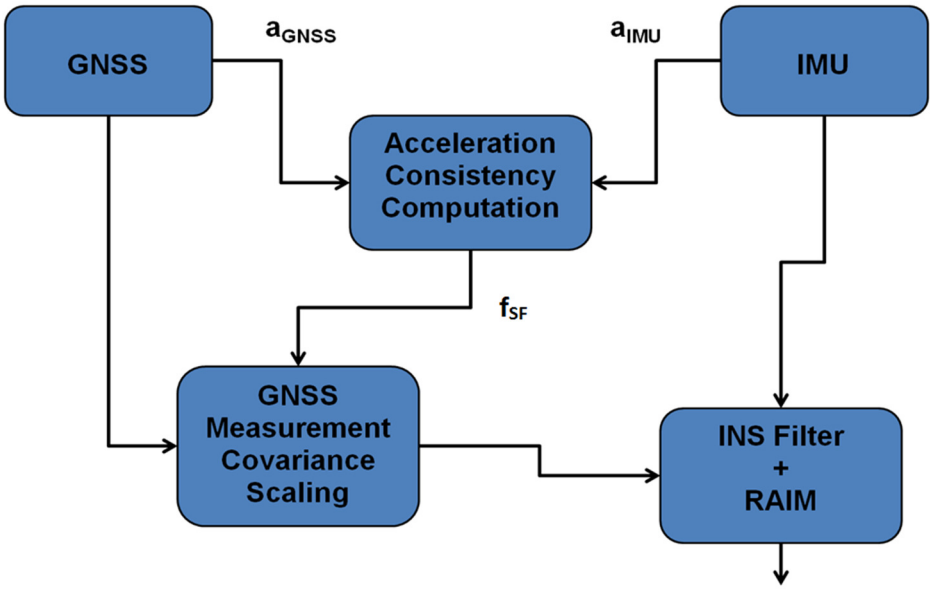

Figure 4-3: Block Diagram of GNSS Covariance Adaptive Scheme

Firstly, the user accelerations are computed along the three axes of the Earth Centered Earth Fixed (ECEF) frame using the GNSS Doppler measurements. The details on the computation of the user acceleration from the GNSS are given in Appendix B. The user accelerations are also sensed by the accelerometers inside the IMU. These accelerations, however, are in the IMU sensor frame. Thus they are transformed into the ECEF frame using rotation matrices so that they can be directly compared with the accelerations obtained using the GNSS measurements. The errors associated with each solution are assumed to follow Gaussian distributions. For the case when the GNSS measurement errors are assumed to follow the *t* distribution, the adaptive part of the GNSS variance still assumes a Gaussian distribution for the Doppler measurements while computing a GNSS derived user acceleration. The components a_{IMU} and a_{GNSS} in Figure

4-3 are the user acceleration values along a certain axis obtained using the accelerometer and that computed from the GNSS Doppler measurements respectively with associated standard deviation values of σ_{IMU} and σ_{GNSS}. The consistency between the two accelerations can then be expressed as the area overlap between the two acceleration distributions as shown in Figure 4-4.

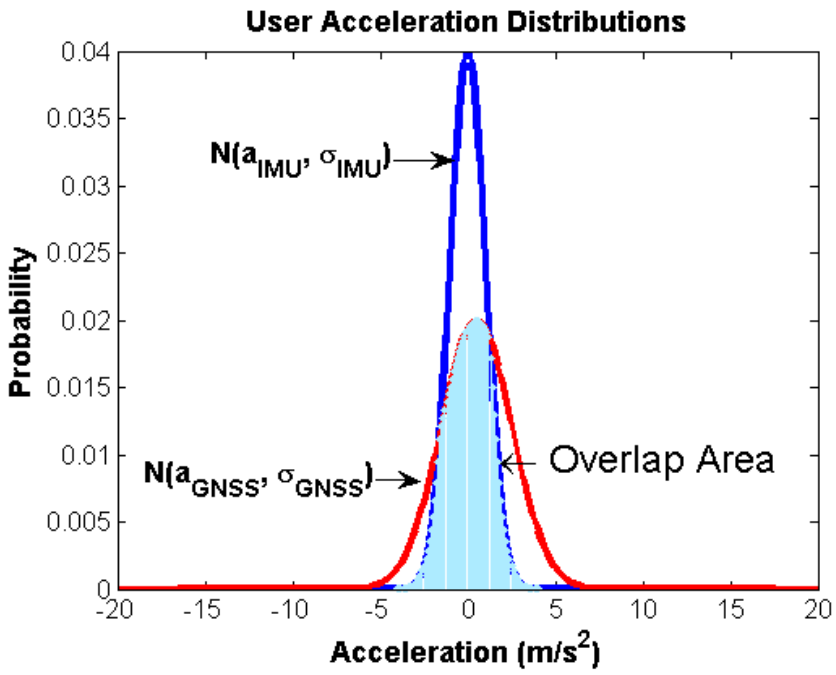

Figure 4-4: Consistency between User Accelerations

The overlap between the distributions can be calculated as a Bhattacharyya coefficient (BC) (Thacker et al 1998). Firstly, the Bhattacharyya distance (DB) for two univariate normal acceleration distributions is given as

$$BD = \frac{1}{4}\frac{(a_{IMU} - a_{GNSS})^2}{\sigma_{IMU}^2 + \sigma_{GNSS}^2} + \frac{1}{2}\log\left(\frac{\sigma_{IMU}^2 + \sigma_{GNSS}^2}{2\sqrt{\sigma_{IMU}^2 \sigma_{GNSS}^2}}\right) \quad \textbf{4-5}$$

The parameter BC is then obtained as

$$BC = e^{-BD} \quad \textbf{4-6}$$

The consistency between these two accelerations, as indicated by the parameter BC, is generally high in open sky conditions. However, in areas where the GNSS measurement quality degrades, the consistency between the two accelerations decreases. This is attributed to the increase in the variance of GNSS Doppler measurements and the error in the GNSS derived acceleration. Thus, in areas with a good consistency, a higher weight (lower variance) is assigned to GNSS measurement updates while in areas with a poor consistency, a lower weight is used. This is done by scaling the *a priori* GNSS variance using a scale factor, f_{SF}, that is computed based on the consistency between the two accelerations, as indicated in the block diagram of Figure 4-3.

The adaptation of the GNSS variance, based on the consistency of the acceleration values obtained using the two sensors, proposed in this dissertation, is shown in the flowchart of Figure 4-5.

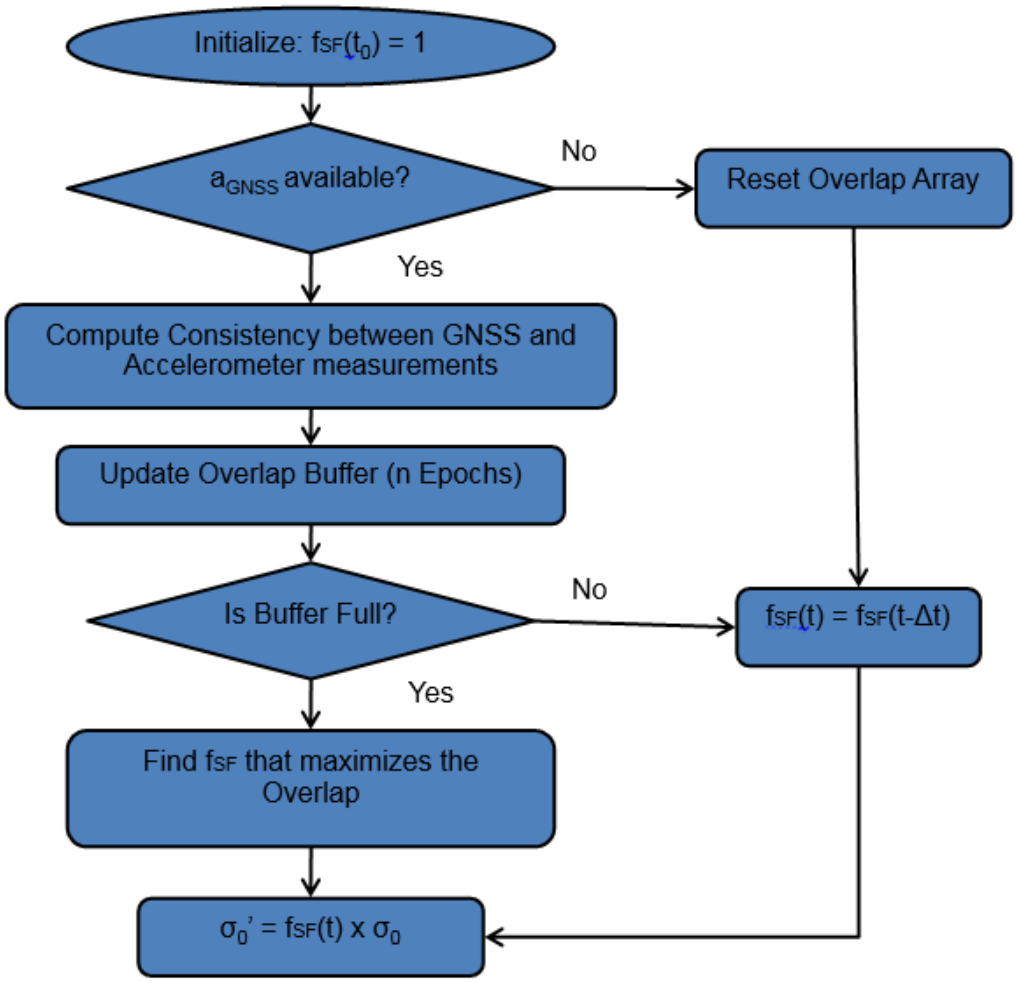

Figure 4-5: Flowchart for Adaptation of GNSS Variance

As with other non-adaptive filters, initially an assumption is made about the *a priori* variance for the GNSS measurements. The goal of the above architecture is to find a value to scale this *a priori* variance, so that the assumed measurement noise distribution closely matches the true error characteristics. As mentioned in Appendix B, the condition of the minimum number of Doppler measurements required for obtaining the user acceleration must however be met before the consistency between the accelerations can

be computed. The method described in Appendix B can be considered as a loosely coupled consistency check as the comparison is done after the user accelerations are made available by the two systems. However, the comparison could also be done using a tightly coupled approach. With the knowledge of the orientation of the IMU and the direction cosines of the satellites, the accelerations on the IMU could be mapped to the line of sight acceleration from the Doppler derivative of each satellite. This method would obviate the condition of having a certain minimum number of Doppler measurements.

In order to mitigate the effect of noise in the Doppler measurements, the consistency is computed as a moving average of the consistency values at '*n'* number of GNSS epochs; such that the adjacent epochs are typically separated by 50 ms. A buffer to store the consistency values of *'n'* consecutive epochs is thus maintained. This introduces a latency of *'n-1'* epochs at the beginning before the a priori variance scale factor can be computed. Moreover, if not enough Doppler measurements are available somewhere during the processing, then the buffer is reset as it has to hold the consistency values of *'n'* consecutive epochs in order to get the filtered consistency values.

Once the buffer is full, the current value of consistency is repeatedly computed by scaling the initial *a priori* variance with a range of scale factors. The final scale factor, and hence the final *a priori* variance, for the current epoch is chosen such that the moving average of the consistency values is maximized.

The performance of the filtering schemes presented in this chapter is compared to the standard approach in Chapter 6.

Chapter Five: **Pre-Filter Sensor Validation**

For personal navigation devices that are realized as a multi-sensor navigation system, a fault occurring in any of the sensors in use can affect the performance of the navigation system, potentially compromising the reliability of the navigation solution. It is thus imperative to detect and remove faults occurring in the individual sensors before they are integrated in a navigation filter. In this in regard, a pre-filter sensor validation scheme that is able to detect the occurrence of faults in individual sensor measurements is proposed in this chapter.

In order to realize a scheme that can overcome the drawbacks of prevalent methods, as discussed in Section 1.2.2, the sensor validation scheme proposed herein is designed while considering the constraints in terms of cost and complexity of the navigation system. These constraints are met by exploiting the analytical redundancy between dissimilar sensors to detect faults in the measurements. Analytical redundancy is achieved through the mathematical relationships between different sensor measurements. This avoids the use of redundant sensors which is common among the prevalent sensor validation schemes. The proposed scheme confirms the correct operation of various sensors before they are used in the estimation scheme (e.g. extended Kalman filter) thereby improving reliability. Sensor measurements deemed to be invalid by the sensor validation scheme can then be discarded.

5.1 Sensor Validation through Common Parameter Observation

Having identified the possible fault scenarios in various sensors, as discussed in Section 3.2, the proposed pre-filter sensor validation scheme confirms the correct operation of individual sensors through comparison of consistencies between common parameters obtained using dissimilar sensors. These common parameters are termed inter-sensor equivalents. The inter-sensor equivalents provide the analytical redundancy between dissimilar sensors already present in the multi-sensor platform and thus avoids the use of multiple sensors of the same kind for detecting faults.

The inter-sensor equivalents used in the pre-sensor validation scheme include user acceleration, angular velocity and magnetic field vector. These parameters can be observed independently using measurements from at least two different sensors in the multi-sensor platform. Before discussing the proposed sensor validation architecture in Section 5.2, the methods of observing these inter-sensor equivalents using different sensors are presented in the following sub-sections.

5.1.1 User Acceleration

User acceleration can be obtained using differentiated GNSS Doppler measurements. The computation of user acceleration from GNSS Doppler measurements is given in Appendix B. Similarly, the user acceleration can also be obtained from acceleration measurements. However, in order to compare these accelerations, the acceleration values have to be transformed appropriately to a common coordinate frame. Similarly, user acceleration can also be obtained along the vertical direction using twice

differentiated barometric altimeter measurements. Thus the comparison of barometer derived accelerations with that of other sensors will be only along the vertical axis.

The observation of user acceleration using three disparate sensors, available in the multi-sensor platform used during this work, provides an analytical redundancy of two. Due to this redundancy, it is possible to detect and isolate a fault occurring in one of the sensor measurements.

5.1.2 Angular Velocity

Angular velocity can be directly observed through the gyroscope measurements. However, angular velocity can also be derived from differentiated magnetometer measurements. The derivation of the angular velocity from magnetometer measurements is based on the assumption that the magnetic field intensity remains constant. Thus, any change in the orientation of the tri-axis magnetic field sensor results in respective changes in the fields sensed along the axes of the magnetometer. Consequently, a rate of change of the sensed magnetic field corresponds to the rate of change of orientation (i.e. the angular velocity). The derivation of the angular velocity from magnetometer measurements is presented below.

The geomagnetic field vector of Earth in the local level frame (L-frame) is given as

$$H^L = H\begin{bmatrix} \sin d \\ \cos d \\ \tan I \end{bmatrix} \qquad \textbf{5-1}$$

where H is the geomagnetic field strength in the horizontal plane, d is the magnetic inclination angle and I is the magnetic inclination.

The magnetic field measured by the magnetometer triad in the body frame (B-frame) can then be expressed as

$$\begin{aligned} H^B &= T_p T_r T_h H^L \\ &= R_L^B H^L \end{aligned} \qquad \textbf{5-2}$$

where R_L^B is a rotation matrix from the L to the B frame which can be expanded as a function of changes in pitch, roll and azimuth angles.

$$\begin{aligned} R_L^B = T_p T_r T_A &= \begin{bmatrix} \cos p & 0 & -\sin p \\ 0 & 1 & 0 \\ \sin p & 0 & \cos p \end{bmatrix} . \begin{bmatrix} 1 & 0 & 0 \\ 0 & \cos r & \sin r \\ 0 & -\sin r & \cos r \end{bmatrix} . \begin{bmatrix} \text{cosA} & \text{sinA} & 0 \\ -\text{sinA} & \text{cosA} & 0 \\ 0 & 0 & 1 \end{bmatrix} \\ &= \begin{bmatrix} \cos A \cos r - \sin A \sin p \sin r & \sin A \cos r + \cos A \sin p \sin r & -\cos p \sin r \\ -\sin A \cos p & \text{cosAcosp} & \sin p \\ \cos A \sin r + \sin A \sin p \cos r & \sin p & \cos p \cos r \end{bmatrix} \end{aligned} \qquad \textbf{5-3}$$

Assuming that the magnetic field is constant when going from time t to $t + \Delta t$ and that H and d are known, the time derivative of Equation 5-2 gives

$$\dot{H}^B = \dot{R}_L^B H^L \qquad \textbf{5-4}$$

However, the rate of change of the transformation matrix R_L^B can be given as (Noureldin et al 2013)

$$\dot{R}_L^B = R_L^B \Omega_{BL}^L \tag{5-5}$$

where Ω_{BL}^L is the skew-symmetric form of angular velocity given as

$$\Omega_{BL}^L = \begin{bmatrix} 0 & -w_z & w_y \\ w_z & 0 & -w_x \\ -w_y & w_x & 0 \end{bmatrix} \tag{5-6}$$

Thus, from equations 5-5 and 5-6,

$$\begin{aligned} \dot{H}^B &= R_L^B \Omega_{BL}^L H^L \\ &= R_L^B R_B^L \Omega_{BL}^B R_L^B H^L \\ &= \Omega_{BL}^B R_L^B H^L \\ &= \Omega_{BL}^B H^B \end{aligned} \tag{5-7}$$

Using the property $a \times b = \Omega_a b$, where $a \times b$ is the cross product of the two vectors a and b and Ω_a is the skew-symmetric matrix of vector a, Equation 5-7 can be expressed as

$$\begin{aligned} \dot{H}^B &= w_{BL}^B \times H^B \\ &= -(H^B \times w_{BL}^B) \\ &= -\Omega_{H^B} w_{BL}^B \end{aligned} \tag{5-8}$$

where Ω_{H^B} is the skew-symmetric form of vector H^B and $w_{BL}^B = \begin{bmatrix} w_x \\ w_y \\ w_z \end{bmatrix}$.

The angular velocity w_{BL}^B can thus be obtained as

$$w_{BL}^{B} = -\Omega_{H^B}^{-1}\dot{H}^{B} \qquad \textbf{5-9}$$

However, the system of linear equations represented by Equation 5-9 does not have a unique solution and the inverse of the matrix Ω_{H^B} does not exist. Hence, during this work, the angular velocity is computed as a best fit solution that is optimized in the least squares sense (i.e. the solution with a minimum Euclidean norm). Such solution can be obtained by computing the Moore-Penrose pseudoinverse of the matrix Ω_{H^B}. Hence Equation 5-9 can be modified to the following form:

$$w_{BL}^{B} = -\Omega_{H^B}^{+}\dot{H}^{B} \qquad \textbf{5-10}$$

where $\Omega_{H^B}^{+}$ is the pseudoinverse of the matrix Ω_{H^B}.

There are several ways of computing the pseudoinverse. One of the computationally efficient and accurate ways is to use the singular value decomposition. The singular value decomposition factorizes a real matrix A of dimension $m \times n$ to the form:

$$A = U \sum V^{T} \qquad \textbf{5-11}$$

where U is a unitary matrix of order $m \times m$, $\sum$ is an $m \times n$ diagonal matrix containing singular values of A and V is a unitary matrix of order $n \times n$. The pseudoinverse of matrix A is then computed as

$$A^{+} = V \sum^{+} U^{T} \qquad \textbf{5-12}$$

The matrix $\sum^{+}$ is obtained by inverting all the non-zero diagonal elements of the matrix $\sum$.

The observation of angular velocity using two dissimilar sensors provide an analytical redundancy of one. This enables the detection of measurement faults in any of these sensors. The identification of the fault, however, is not possible with the available degree of redundancy. But the sensor validation scheme does not need to rely on a single inter-sensor equivalent to attain analytical redundancy. A higher degree of redundancy can be obtained through the comparison of more than one inter-sensor equivalents among dissimilar sensors, which will be discussed in Section 5.2.

5.1.3 Magnetic Field Vector

Finally, the third inter-sensor equivalent is the magnetic field vector which is directly obtained from magnetometer measurements. They can also be obtained using a reference geomagnetic field model such as the international geomagnetic reference field model (IGRF). The magnetometer measurements must be rotated to the same frame as the reference model (or vice-versa) and thus is fundamentally tied to the efficacy of the attitude solution. Alternatively the measurements can be compared on a magnitude basis, in which case the system acts more like a perturbation detector (e.g. Afzal et al 2011). In this case, the magnitude of the total magnetic field can be simply computed from the magnetometer measurements as

$$\left|H^{B}\right| = \sqrt{\left(H_X^2 + H_Y^2 + H_Z^2\right)} \qquad \textbf{5-13}$$

where H_X, H_Y and H_Z are the magnetometer measurements sensed by the magnetometer along its orthogonal axes.

5.2 Pre-Filter Sensor Validation Flowchart

The flowchart of the proposed pre-filter sensor validation architecture is depicted in Figure 5-1. The purpose of this proposed architecture is to validate the measurements from four sensors, namely the magnetometer triad, the gyroscope triad, the accelerometer triad and the barometer. Only the validated sensor measurements are passed on to the integration filter, while the faulty sensor measurements are rejected. In the case when validation is not possible, a warning signal is issued to alert the user.

Some of the sensors can be validated simultaneously while the validation of some is dependent on the validation of other sensors. The sequence of validation is based on the degree of redundancy. In the validation architecture realized during this work, the accelerometer and magnetometer measurements are validated at the beginning due to higher degree of analytical redundancy. This is followed by the validation of the barometer and gyroscope measurements.

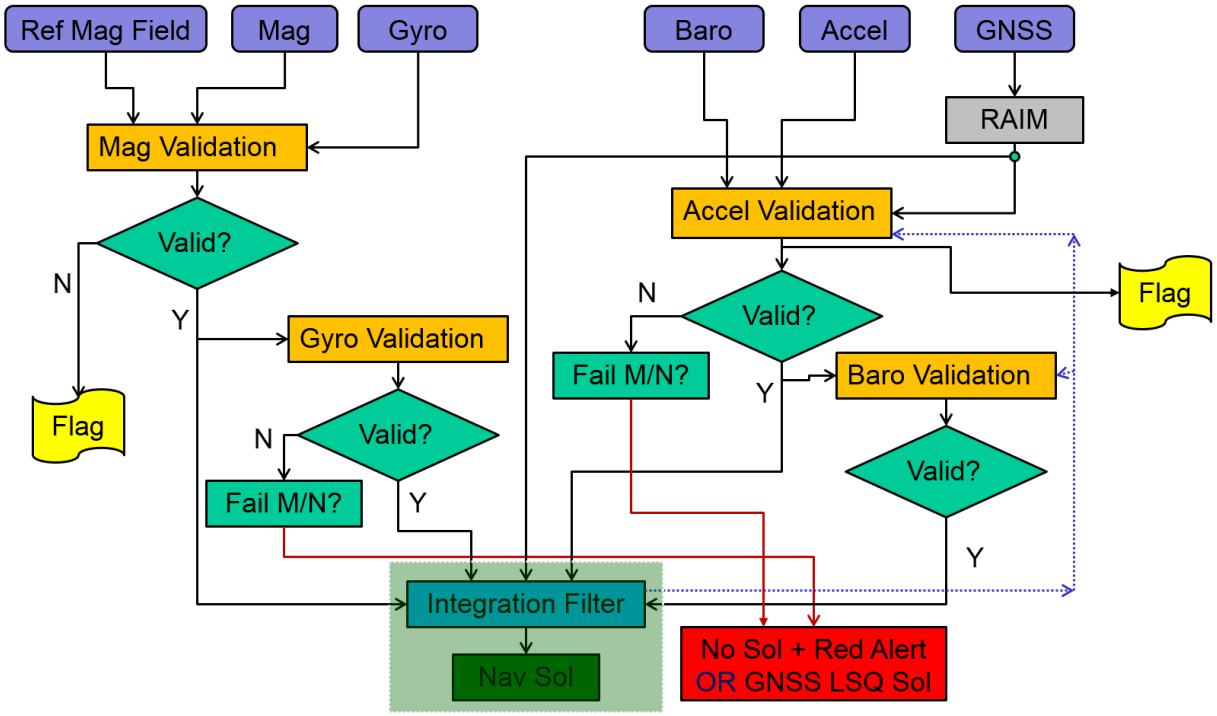

Figure 5-1. Pre-Filter Sensor Validation Flowchart

The sensor validation scheme realized as per above flowchart makes the sensor validation highly independent from the integrated filter. It thus acts as an effective quality control measure before faults are tested through innovation based tests in the integration filter.

5.2.1 Magnetometer Validation

The magnetometer is validated through the observation of two inter-sensor equivalents. Firstly, the total magnetic field obtained from the reference geomagnetic field model is compared to the total magnetic field computed from the triad of calibrated magnetometer measurements. Similarly, the magnetometer is also compared to the gyroscope through

the observation of angular velocities. The angular velocities derived from the magnetometer measurements are compared to those observed using the gyroscopes. Thus, by comparing the magnetometer to the reference magnetic field and the gyroscope, through the observation of two inter-sensor equivalents, an effective analytical redundancy of two is obtained during magnetometer validation. Based on the consistency of the magnetometer with the reference magnetic field and the gyroscopes, a decision is made if the magnetometer measurement is valid or not.

If the magnetometer is deemed valid, it is then passed to the integration filter and is also further used to validate the gyroscope measurements. However, if the magnetometer fails validation, the magnetometer measurement will not be used in the integration filter. Moreover, an invalid magnetometer measurement also means that it will no longer be possible to validate the gyroscopes. In such a case, a yellow flag would be raised to indicate that some of the sensors could not be validated and that the estimated navigation solution is not completely reliable.

The details on the comparison of inter-sensor equivalents for the validation of sensor measurements is given in Section 5.2.5.

5.2.2 Gyroscope Validation

As mentioned in the previous section, the gyroscope can be validated only after the magnetometer has been validated. The validation is again done through the comparison of the angular velocities observed by the magnetometer and the gyroscope. With just one degree of redundancy in this comparison, it would not have been possible to identify the faulty sensor measurement if the magnetometer was not already validated.

The gyroscopes and the accelerometers are however the core components of the integration filter which is realized as a strap-down inertial navigation system (INS) using extended Kalman filter (EKF) equations. Thus, if any of these sensors are deemed to be invalid, a red flag is raised to indicate that the navigation solution is not reliable. Alternatively, a GNSS only solution could be made available in case of failure of accelerometers or gyroscopes.

It is therefore important to ensure that the detection of fault in these primary sensors is not caused due to some short term errors in the validation algorithm or a short communication failure. Thus, a fault should be declared in the primary sensors only if the detected fault persists for a significant time duration. In this regard, a fault is declared in the gyroscope measurements only if the consistency of the gyro derived angular velocity with that derived from magnetometer is below the pre-set threshold for 80 % of the data within a time span of 30 s. In this regard, a moving average filter of 30 s is maintained, which counts the percentage of data during which the consistency is below the threshold. A red flag is raised only when the count reaches 80%.

5.2.3 Accelerometer Validation

The accelerometer is validated using only one inter-sensor equivalent, namely the user acceleration. The user acceleration obtained using the accelerometer is compared to that obtained using the GNSS and barometer.

If the accelerometer is deemed valid, it is used in the navigation filter and further used to validate the barometer measurement. As with the gyroscope, an accelerometer is deemed to be faulty only if its consistency with other sensors falls below the pre-set

threshold for 80 % of the epochs during a time window of 30 s. If the accelerometer is deemed to be faulty, a red flag is raised to indicate that the solution is unreliable. However, in situations when the number of GNSS measurements is insufficient to compute user accelerations, faults occurring in the accelerometer cannot be identified. In such cases, a yellow flag is raised to indicate that the sensor could not be validated. This is common in indoor scenarios.

5.2.4 Barometer Validation

Finally, the validated accelerometer is used to test the barometer measurement. The user acceleration along the vertical direction obtained using the accelerometer is compared to that obtained from the barometer. If the barometer could not be validated, it is not used in the integration filter.

5.2.5 Sensor Validation through Consistency Comparison

The comparison of the inter-sensor equivalents and their quantization can be better understood through Figure 5-2.

The consistencies between different sensors are computed through the comparison of inter-sensor equivalents. In order to quantize the consistencies, the inter-sensor equivalents observed or computed from each sensor are assumed to be drawn from normal distributions with corresponding means equal to the computed values of the inter-sensor equivalents. The variances of the normal distributions can be obtained from the noise characteristics of the respective sensors after the application of necessary transformations. The consistencies between two sensors can then be expressed as the overlap between the two distributions related to the estimated inter-sensor equivalent

values. The overlap between the distributions can be calculated as a Bhattacharyya coefficient (BC) following the same procedure discussed in Section 4.2.

The consistency parameters $C1$, $C2$, $C3$ and $C4$, in Figure 5-2, are all computed as Bhattacharyya coefficients. For instance, during accelerometer validation, the consistency parameters $C3$ and $C4$ are computed as follows:

$$C3 = \exp\left[-\left\{\frac{1}{4}\frac{(a_{IMU,U} - a_{Baro,U})^2}{\sigma_{IMU,U}^2 + \sigma_{Baro,U}^2} + \frac{1}{2}\log\left(\frac{\sigma_{IMU,U}^2 + \sigma_{Baro,U}^2}{2\sqrt{\sigma_{IMU,U}^2\sigma_{Baro,U}^2}}\right)\right\}\right] \quad \textbf{5-14}$$

where $a_{IMU,U}$ and $a_{Baro,U}$ are the user accelerations along the vertical direction obtained from accelerometer and barometer while $\sigma_{IMU,U}$ and $\sigma_{Baro,U}$ are the associated uncertainties. The parameter $C4$ is however computed as an average of consistency values along the three orthogonal axes as

$$C4_X = \exp\left[-\left\{\frac{1}{4}\frac{(a_{IMU,\mathrm{E}} - a_{\mathrm{GNSS,E}})^2}{\sigma_{IMU,\mathrm{E}}^2 + \sigma_{\mathrm{GNSS,E}}^2} + \frac{1}{2}\log\left(\frac{\sigma_{IMU,\mathrm{E}}^2 + \sigma_{\mathrm{GNSS,E}}^2}{2\sqrt{\sigma_{IMU,\mathrm{E}}^2\sigma_{\mathrm{GNSS,E}}^2}}\right)\right\}\right]$$

$$C4_Y = \exp\left[-\left\{\frac{1}{4}\frac{(a_{IMU,\mathrm{N}} - a_{\mathrm{GNSS,N}})^2}{\sigma_{IMU,\mathrm{N}}^2 + \sigma_{\mathrm{GNSS,N}}^2} + \frac{1}{2}\log\left(\frac{\sigma_{IMU,\mathrm{N}}^2 + \sigma_{\mathrm{GNSS,N}}^2}{2\sqrt{\sigma_{IMU,\mathrm{N}}^2\sigma_{\mathrm{GNSS,N}}^2}}\right)\right\}\right] \quad \textbf{5-15}$$

$$C4_Z = \exp\left[-\left\{\frac{1}{4}\frac{(a_{IMU,\mathrm{U}} - a_{\mathrm{GNSS,U}})^2}{\sigma_{IMU,\mathrm{U}}^2 + \sigma_{\mathrm{GNSS,U}}^2} + \frac{1}{2}\log\left(\frac{\sigma_{IMU,U}^2 + \sigma_{\mathrm{GNSS,U}}^2}{2\sqrt{\sigma_{IMU,\mathrm{U}}^2\sigma_{GNSS,U}^2}}\right)\right\}\right]$$

$$C4 = \frac{(C4_X + C4_Y + C4_Z)}{3}$$

where $a_{IMU,\mathrm{LF}}$ and $a_{\mathrm{GNSS,LF}}$ are the user accelerations along a particular local level frame LF ($\mathrm{LF} = \mathrm{E}, \mathrm{N}$ or U; $E = East, N = North, U = Up$) obtained from accelerometer and GNSS while $\sigma_{IMU,\mathrm{LF}}$ and $\sigma_{\mathrm{GNSS,LF}}$ are the associated uncertainties.

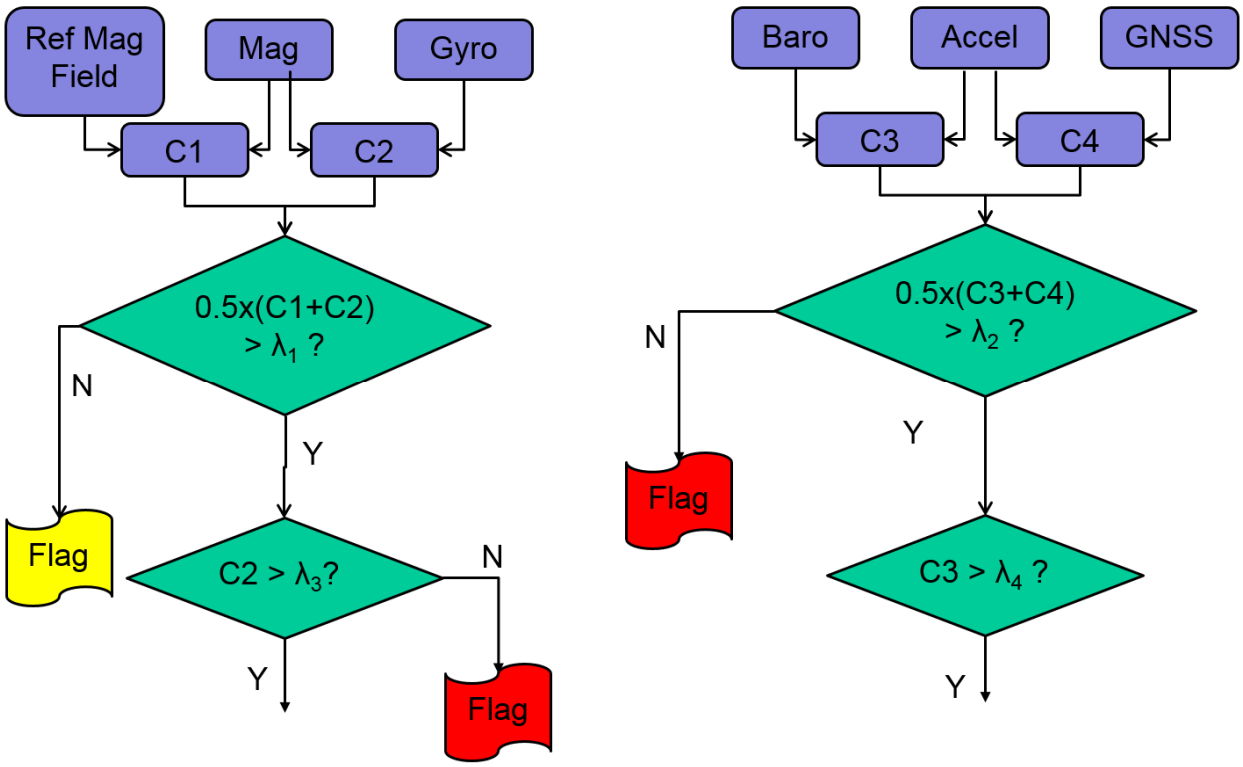

Figure 5-2. Consistency Comparison between Sensors

In order to mitigate the effect of noise that is translated from the sensor measurements to the inter-sensor equivalents, a moving average filter is used to smooth the inter-sensor equivalent values. The moving average filter is implemented using a Hanning window of length five seconds. The Hanning window has a maximum gain at the centre while the

side-lobes roll off at approximately 18 dB/octave. Such use of filtering, however, introduces latency at the output, thus imposing a limitation for real time output realization.

It can be seen from Figure 5-2 for magnetometer and accelerometer validations, the two consistency values are combined through simple averaging. However, a more sophisticated weighing scheme could be used to combine these parameters. Once the consistency values are computed, the validity of the individual sensors is determined by comparing the consistency parameters to a certain threshold. The values of these thresholds are determined empirically and depend upon factors such as system configuration, sensor error characteristics and application requirements.

The pre-filter sensor validation scheme proposed above is tested with both simulated as well as actual sensor faults present in the field data collected in various environments as presented in the following chapter.

Chapter Six: **Data Collection and Assessment of the Proposed Algorithms**

Considering that the overall goal of this research work is to improve the reliability of multi-sensor integrated navigation systems in harsh environments, the algorithms developed in Chapter 4 and Chapter 5 are now assessed by processing multiple field data collected in such harsh environments as urban areas and natural canyons. Due to the modularity of the proposed algorithms, the individual algorithm modules are assessed separately as well as in combinations. In the case of the pre-filter sensor validation scheme presented in Chapter 5, the fault scenarios may not occur in some sensors during field tests. Hence, the proposed validation scheme is mostly assessed by adding sensor errors in clean data sets. However, the algorithm module is also assessed by processing field data collected in some particular test environments in which actual faults occur in some of the sensors.

6.1 Data Collection Setup

In order to evaluate the performance of the proposed algorithms, both pedestrian and vehicular data were collected in GNSS signal challenged environments. The data collection platform, namely the NavCube (Morrison et al 2012) is the primary component in all the experiments. The other major component in the test setup is the NovAtel's SPAN system which was used to provide the corresponding reference solutions. The SPAN system consists of a low noise, tactical grade LCI IMU from Northrop-Grumman Litef GMBH and a NovAtel SPAN-SE GNSS receiver.

The experimental setup for most of the field tests was of the form depicted by the block diagram in Figure 6.1.

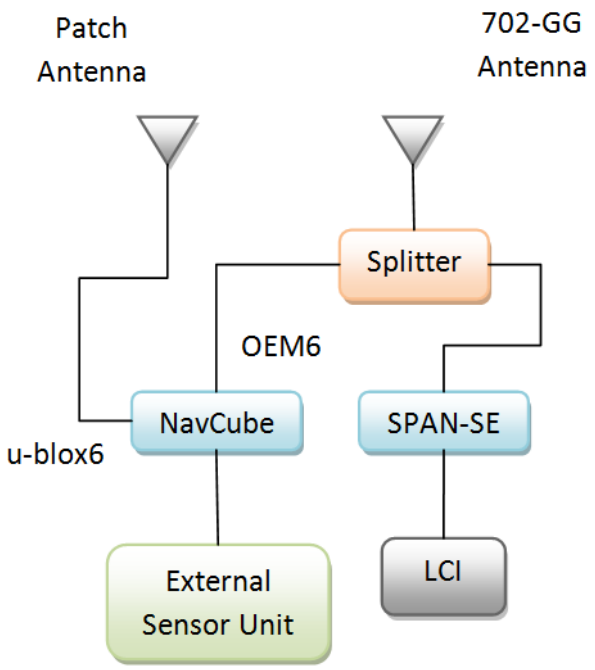

Figure 6-1. Block Diagram of Equipment Setup

As shown in Figure 6-1, GNSS data collected using NovAtel's high performance GPS-702-GG antenna was split to feed the OEM628, or simply OEM6, receiver inside the NavCube and the SPAN-SE receiver. A small ANN-MS-0-005 active patch antenna from u-Blox was used to collect GNSS data for the high sensitivity u-blox 6T, or simply u-blox6, receiver inside the NavCube. The inertial data, magnetometer data and barometer data were collected using the ADIS16488 sensor unit, connected externally to the NavCube.

Figure 6-2 shows a typical equipment setup for collecting pedestrian data. It comprises a rigid aluminium backpack that houses the NavCube, external sensor pod, antennas, the reference system and the batteries to power the equipment. The total weight of the backpack along with the equipment carried over it is approximately 25 kg, most of the weight being that of the rigid pack itself and the GPS/INS unit needed for the reference trajectory. While the first external sensor pod (External Sensor Pod 1), seen in the figure, is mounted rigidly over the backpack, a second sensor pod (External Sensor Pod 2) is mounted on the ankle of the user.

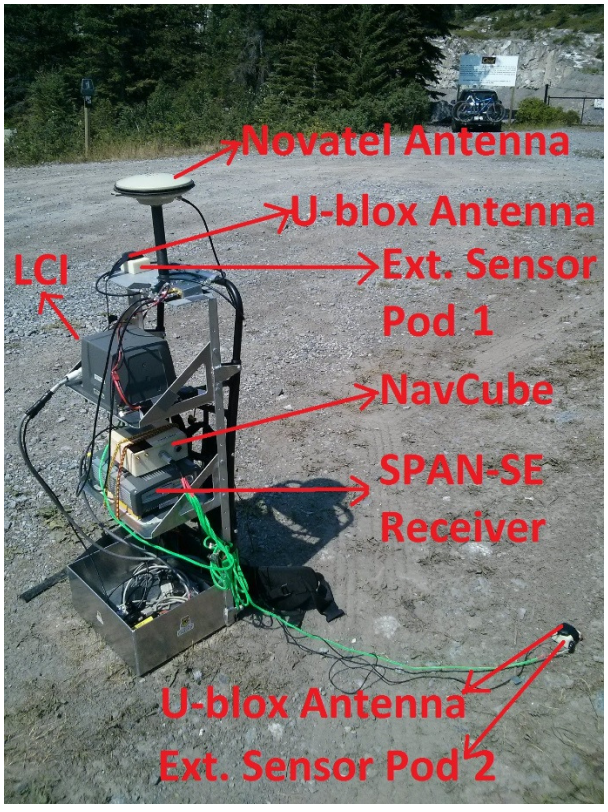

Figure 6-2. Pedestrian Data Collection Equipment Setup

A reference navigation solution was computed for each field test in order to evaluate the accuracies of the navigation solutions. Besides the SPAN system carried in the backpack, the reference system also comprised a static base station set at a pre-surveyed location. A NovAtel Propak V3 receiver was used for this purpose. The reference solution was computed using a tightly-coupled GNSS/INS solution, computed using NovAtel's Waypoint Inertial Explorer post-processing software. The accuracy of the reference trajectory was better than 0.2 m (1 σ) for most of the experiments.

6.2 Test Environments

In order to assess the performance of the proposed schemes, field data were collected in various environments. The data were mostly collected in areas with poor GNSS signal conditions. However, data was also collected in fault free environments in order to be able to analyse the performance of the proposed scheme with simulated errors added to specific sensor measurements at specific times. The field tests carried out in different environments during this research are summarized in the following subsections.

6.2.1 Urban Canyon Data

Urban canyons, created by the presence of tall buildings on either side of a street in dense urban areas, make navigation very challenging, especially for navigation systems with GNSS as a major component. The presence of multiple NLOS multipath signals with significant biases and limited visibility of the satellites degrades the quality and availability of the GNSS measurements. Hence, in order to assess the proposed schemes in GNSS challenged environments, both vehicular and pedestrian data were collected in downtown

Calgary, Canada. The test environment, shown in Figure 6-3, presented elevation mask angles varying from 15 to over 75 degrees.

Figure 6-3. Pedestrian Data Collection in an Urban Canyon

For all the data sets collected in the urban area, the equipment setup was similar to that shown in the block diagram of Figure 6-1. The base station for each of these tests was set at a pre-surveyed location at the University of Calgary, forming a distance of approximately 6 km.

Three sets of data were collected in the urban canyon. With a motive of assessing the proposed schemes for both vehicular and pedestrian mode, a set of vehicular data was

collected in July 2011 followed by a set of pedestrian data in the same area collected in August 2012. Since the adopted magnetometer calibration technique requires the magnetometer to be rotated in different orientations during initialization, a further set of pedestrian data was collected in July 2013 by following the required calibration procedure in order to be able to use the magnetometer data.

The above mentioned data sets will henceforth be referred to as Urban Canyon Vehicular Data, Urban Canyon Pedestrian Data-1 and Urban Canyon Pedestrian Data-2.

6.2.2 Natural Canyon Data

Unlike urban canyons where multipath is more specular, the multipath in natural canyons is generally more diffuse. The variation in the type of multipath while still limiting geometry and availability provides a unique test of the algorithms presented herein. Using a similar equipment setup as the urban scenario, data was thus collected in two natural canyon environments. For both of these data sets, the base stations were set on a car parked close to the trail head. Hence, the baselines for these data sets are smaller than 2 km.

The first set of natural canyon data was collected in February 2013 in King's Creek Canyon, Kananaskis Country, Alberta. This data set will be referred to as Natural Canyon Pedestrian Data-1. The test environment, as shown in Figure 6-4, presented satellite mask angles varying between 50 and 80 degrees.

Figure 6-4. Pedestrian Data Collection in a Natural Canyon

The reference trajectory obtained for this natural canyon data set is shown in Figure 6-5. The trajectory starts at Highway 40 and follows the creek until its end, 1,500 m later. The same snow path was easy to follow exactly on the way back. The fact that the same path was followed forth and back was also used to assess trajectory repeatability. However, despite following the same path in both directions, the error characteristics and signal availability do not remain the same due continuous changes in satellite geometry.

A second set of natural canyon data was collected in July 2014 in Grotto Canyon, Canmore, Alberta. This data set will be referred to as Natural Canyon Pedestrian Data-2. The length of this canyon is approximately 850 m. Similar to the Urban Canyon Pedestrian Data-2, the magnetometer calibration procedure was followed during initialization.

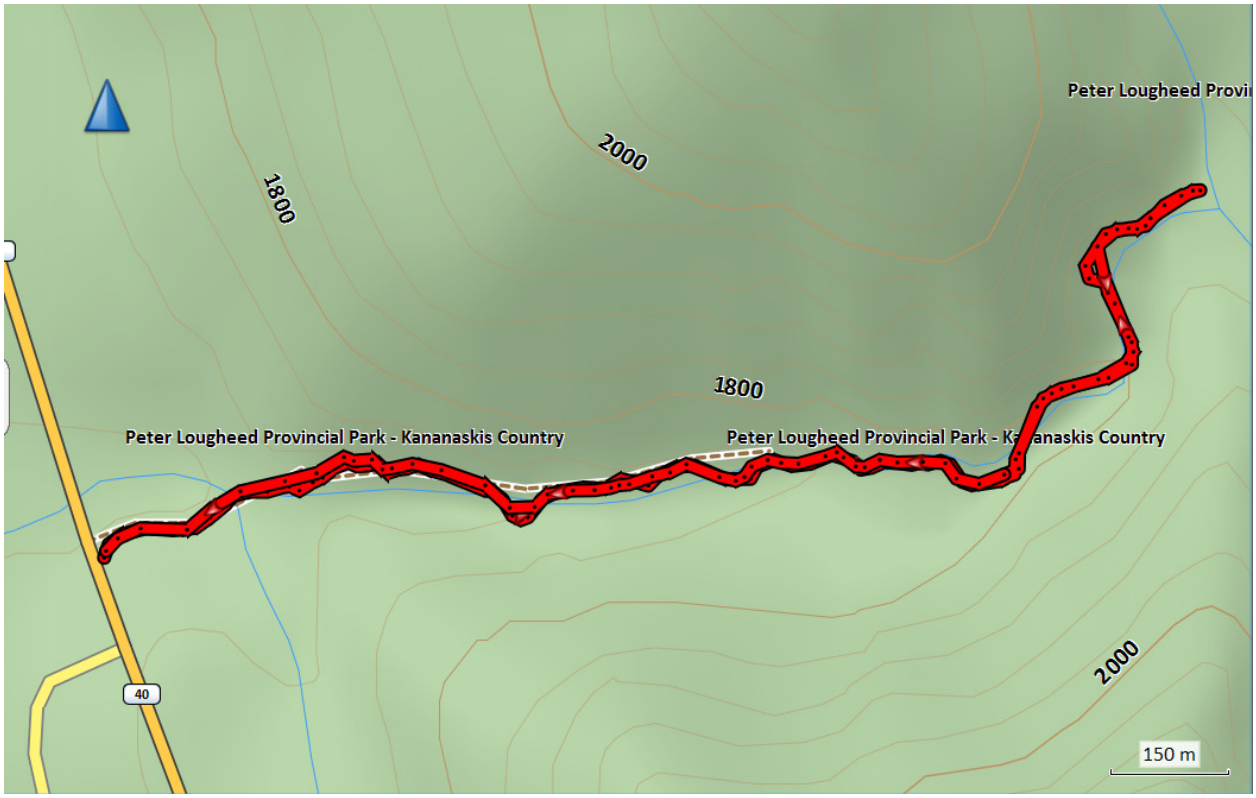

Figure 6-5. Reference Trajectory (Natural Canyon Pedestrian Data-1)

6.2.3 Open Sky Data

Apart from the data collected in harsh environments, some tests were also carried out in fault free environments. The data collected in such environments are as equally important as the ones collected in harsh conditions. The availability of clean data makes it possible to investigate the effect of controlled input measurement alterations to the performance of the proposed algorithms. Faults are simulated in the individual sensor measurements and their effects on the proposed algorithms are studied.

The open sky data were also collected using a similar setup to before. The test locations, however, were very close to the University of Calgary. Thus, a base station set at a pre-

surveyed location at the university was used during the computation of the reference solution in each case.

Three sets of data were collected in open sky conditions. One set of vehicular data was collected on September 2012 around the university in a fairly open sky condition. Similarly, a set of pedestrian data was also collected around the university in August 2012. Finally, one more set of pedestrian data was collected in July 2014, in Nose Hill Park, Calgary, which has completely open sky conditions. These three data sets will henceforth be referred to as Open Sky Vehicular Data, and Open Sky Pedestrian Data-1 and Open Sky Pedestrian Data-2.

The data sets used for the assessment of the algorithms proposed in this dissertation are summarized in Table 6-1.

Table 6-1. Summary of Field Tests

Data Set	Test Location	Test Date
Urban Canyon Vehicular Data	Downtown Calgary	July 2011
Urban Canyon Pedestrian Data-1	Downtown Calgary	August 2012
Urban Canyon Pedestrian Data-2	Downtown Calgary	July 2013
Natural Canyon Pedestrian Data-1	King's Creek Canyon	February 2013
Natural Canyon Pedestrian Data-2	Grotto Canyon	July 2014
Open Sky Vehicular Data	University Area	September 2012
Open Sky Pedestrian Data-1	University Area	August 2012
Open Sky Pedestrian Data-2	Nose Hill Park	July 2014

6.3 Assessment of GNSS Measurement Covariance Adaptive Scheme

As discussed in Chapter 3, a standard tightly coupled GPS/INS filter with residual based FDE is considered as a benchmark against which the proposed algorithms are compared. The GNSS range and Doppler measurement errors in this filter are assumed to follow Gaussian distributions. This benchmark filter, implemented in a C++ software program (Bancroft 2010), is termed as the “Standard filter” in this dissertation. Similarly, the GPS/INS filter implemented with the covariance adaptive algorithm proposed in Section 4.2 is referred to as the “Adaptive filter”.

The Urban Canyon Pedestrian Data-1 is used to assess the performance of the proposed adaptive scheme. The subject walked along the streets in the downtown area carrying the equipment on a backpack as shown in Figure 6-3. Used for analysis are the GNSS data collected with the OEM6 receiver inside the NavCube, along with the inertial data collected using the external sensor pod placed beside the antenna on top of the backpack. The navigation system is implemented as a GPS/INS integrated system. The backpack was kept stationary at the beginning to obtain a rough estimate of gyroscope biases.

Before evaluating the performance of the proposed scheme, the pseudorange measurements collected in the test environment are analyzed to assess the effect of multipath on the measurements and, consequently, on navigation solution. With the knowledge of true position (from the reference solution) and satellite coordinates (from ephemeris), true ranges were obtained. The pseudorange differences and true ranges thus obtained leave a composite of clock bias and errors. The clock bias was then estimated and removed. The pseudorange error computation is discussed in further detail

in Appendix A. The residual range errors, shown in Figure 6-6, mainly comprise multipath and may include small effects due to tropospheric and ionospheric modeling errors.

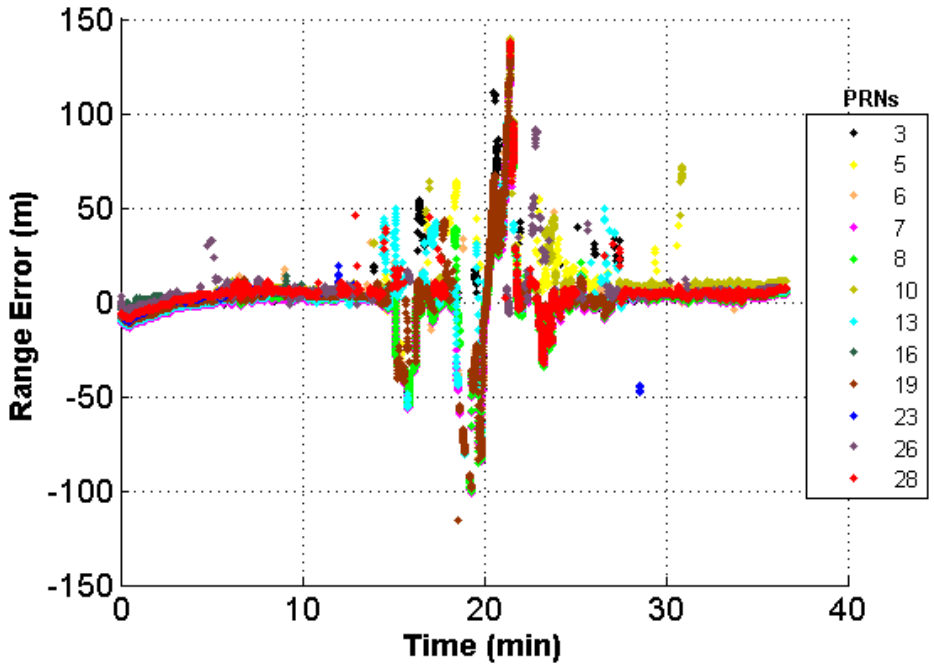

Figure 6-6. Pseudorange Errors – OEM6 (Urban Canyon Pedestrian Data-1)

It can be observed that the range errors are quite significant at many epochs, exceeding well over 100 m, thus indicating highly degraded GNSS signal conditions. The presence of NLOS multipath signals and signal fading can cause the receiver to generate such erroneous measurements through shift of the numerically controlled oscillators (NCO) and distortion of the correlation function.

With the primary focus of the proposed covariance adaptive scheme being improvement in the reliability of the navigation solutions, the two solutions computed using the Standard

and the Adaptive filters are compared in terms of reliability in Figure 6-7. The reliability, as defined in Section 3.1, is determined by the estimated accuracy associated with the navigation solution. The reliability values are computed following the post processing of the data using the above mentioned two filtering algorithms along easting, northing and vertical directions in the local level frame.

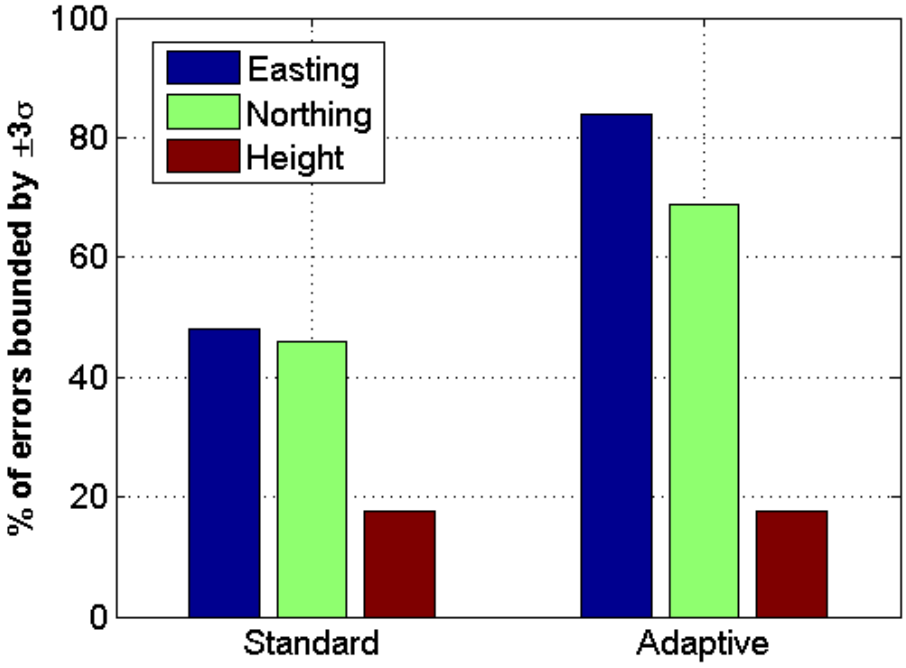

Figure 6-7. Reliability of Navigation Solution – OEM6+IMU (Urban Canyon Pedestrian Data-1)

The reliability values shown in the above figure indicate that the consistency between the position solutions and the associated estimated accuracies is much higher in the case of the proposed adaptive filtering algorithm as compared to the standard approach. Such improvement in reliability occurred despite the fact that there were many epochs where

the numbers of valid GPS Doppler observations were less than four during which the a-priori variance could not be adapted to fit the true GNSS measurement error characteristics. This means that the dynamic adaptation of the GNSS measurement covariance results into more realistic values of estimated accuracies, making the navigation solution more reliable. While the reliability is still not perfect in either of the approaches, the improvement is excellent. There was a 36 % improvement in easting and a 23 % improvement in northing, as shown in Figure 6-7. The improvement along the vertical direction was negligible.

Similarly, the position accuracies of the two pedestrian navigation solutions are compared along the horizontal and vertical directions in Figure 6-8 and Figure 6-9.

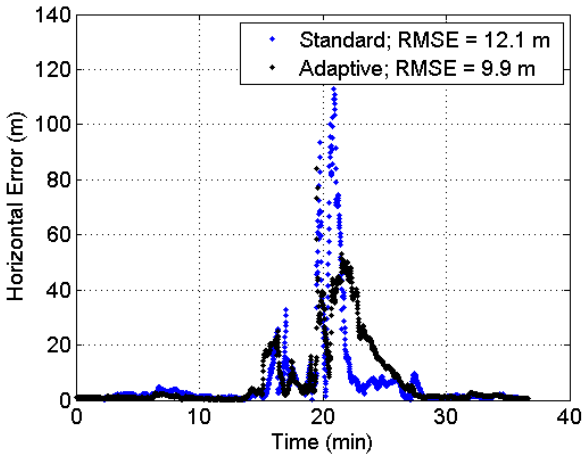

Figure 6-8. Horizontal Error – OEM6+IMU (Urban Canyon Data-1)

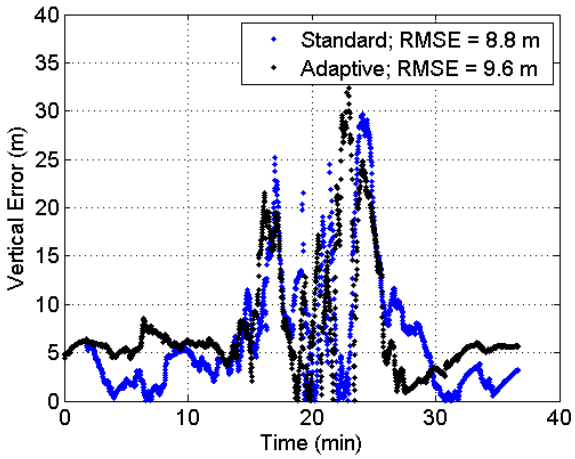

Figure 6-9. Vertical Error – OEM6+IMU (Urban Canyon Data-1)

The error values are obtained by comparing the navigation solutions to the reference solution obtained using the procedure described in Section 6.1. In accordance to the

pseudorange errors shown in Figure 6-6, the position errors are higher for both methods during the times when the GNSS measurement updates are corrupted by multipath. However, the maximum error along the horizontal direction is significantly reduced in the case of the proposed adaptive approach during the worst signal conditions. This can also be observed through the trajectories plotted for the two approaches along with the reference trajectory in Figure 6-10.

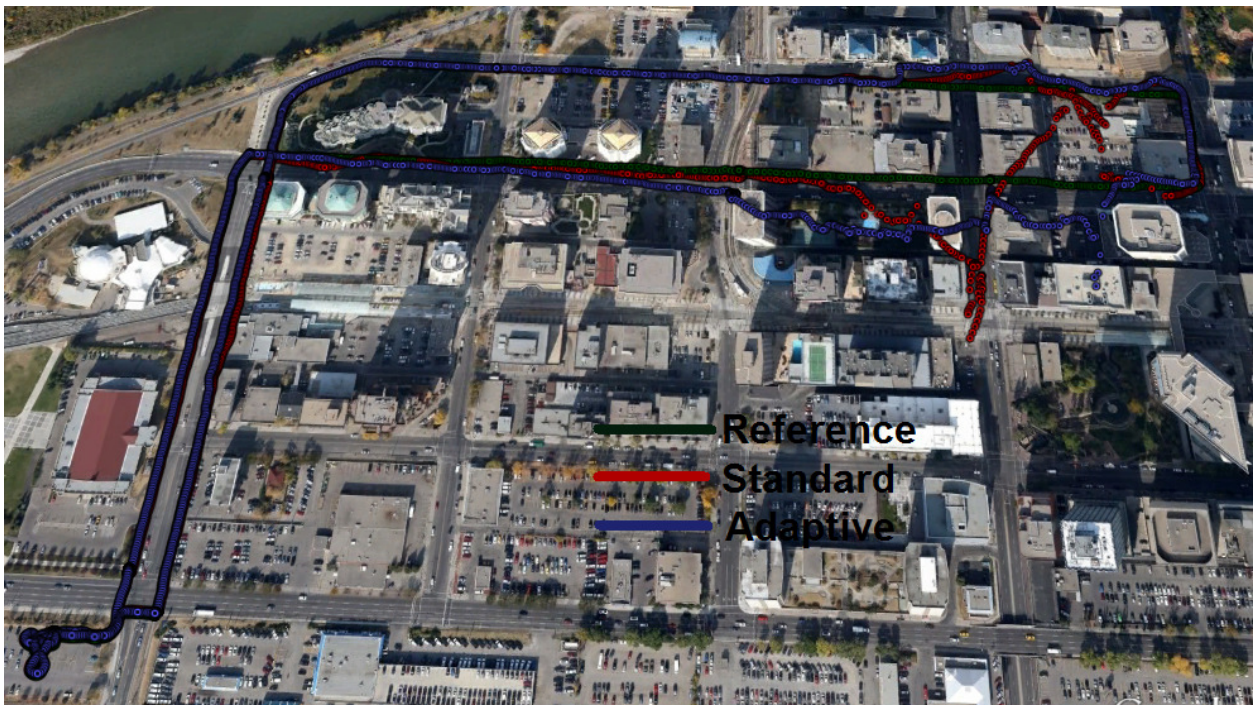

Figure 6-10. Navigation Trajectories (Urban Canyon Pedestrian Data-1)

Similarly, the proposed adaptive scheme is also assessed using a vehicular data collected in the same environment (Urban Canyon Vehicular Data). Again, the GNSS data was collected with the OEM6 receiver inside the NavCube. The inertial data in this case was collected using the ADIS16375 IMU inside the NavCube. The reliability values

computed for this data set, along the axes of local level frame, are shown in Figure 6-11. As with the previous data set, due to the lack of sufficient number of valid GPS measurements, the algorithm was not able to adapt the variance for many GPS epochs. Nonetheless, the proposed adaptive algorithm still increases the reliability by 21 % in easting, 7.3 % in northing and 2.5 % in the up direction. The RMS errors along the horizontal and vertical directions decreased by approximately 5 m and 1.5 m respectively.

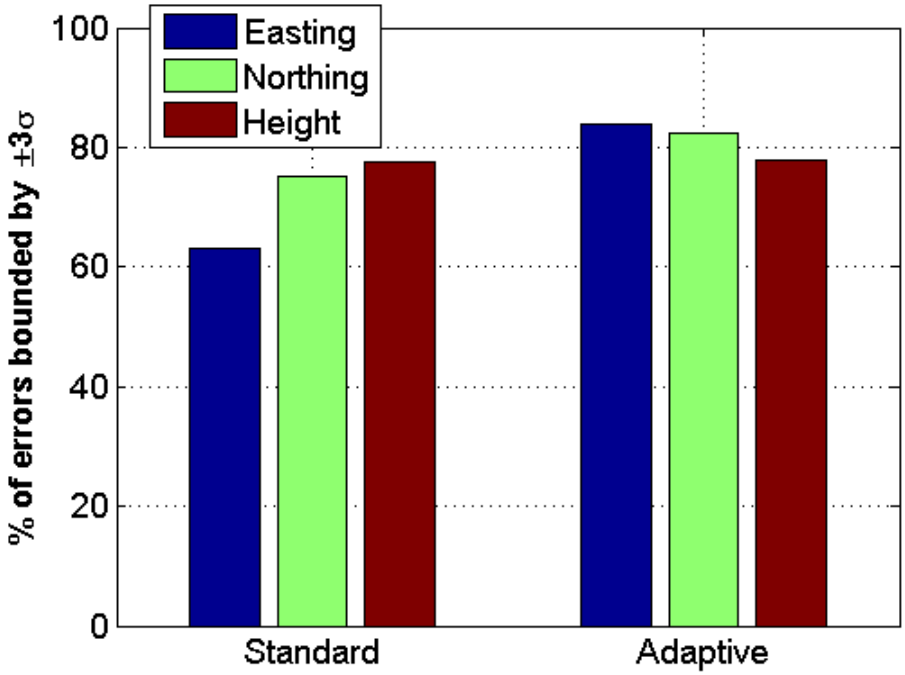

Figure 6-11. Reliability of Navigation Solution – OEM6+IMU (Urban Canyon Vehicular Data)

The proposed adaptive technique can be utilized to its fullest benefit if the measurement quality is degraded but there are still enough valid GPS Doppler measurements to compute user acceleration and consequently the acceleration consistency. To assess the

performance of the algorithm during such conditions, the pedestrian data collected in an open sky condition around the University of Calgary (Open Sky Pedestrian Data-1) is used.

At least seven GPS satellites were visible for the whole navigation test. During post processing, normally distributed range errors with a mean of 20 m and a standard deviation of 10 m were added to three satellite measurements for a period of 5 minutes. Similarly, randomly selected Doppler errors of values ranging from -5 Hz to 5 Hz (i.e. approx. -0.95 m/s to 0.95 m/s for GPS L1 signal) were also added to the same satellite measurements.

The reliability of the navigation solution is shown in Figure 6-12. The adaptive approach significantly improved the reliability of the position solution along all axes. There has been a reliability improvement of 25.4 % in easting, 44.9 % in northing and 8.2 % in the up direction. Contrary to the previous scenarios, there were only a few epochs where the numbers of valid Doppler observations were insufficient to compute the user accelerations. Thus, the covariance could be adapted almost all the time to fit the true measurement error characteristics, which consequently led to an excellent reliability improvement.

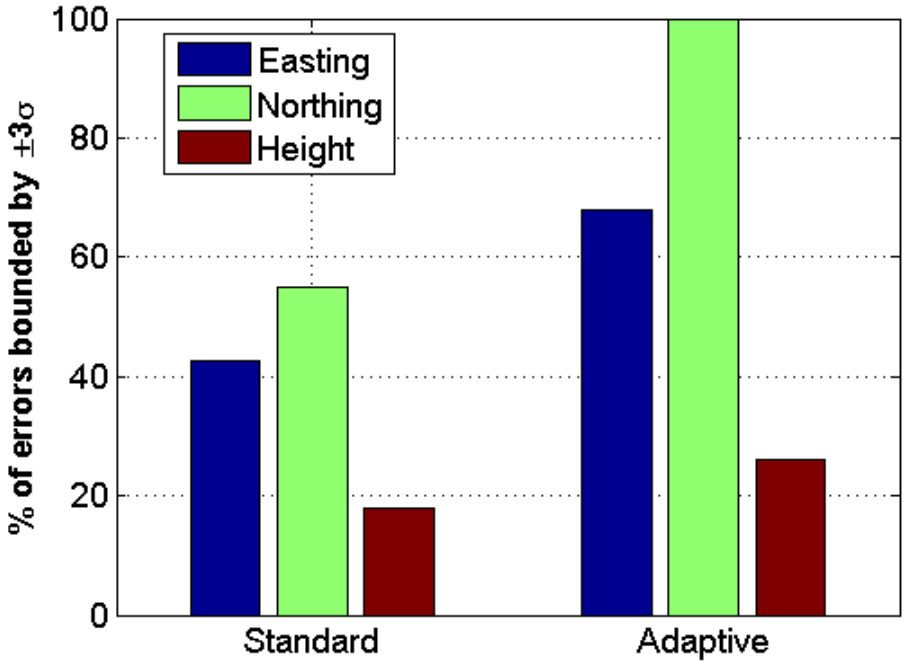

Figure 6-12. Reliability of Navigation Solution – OEM6+IMU (Open Sky Pedestrian Data-1)

In addition to improving the reliability, the proposed adaptive algorithm also improved the accuracy of the navigation solution along the horizontal direction as shown Figure 6-13. However, the algorithm often tends to over-bound the assumed GNSS error distribution during the times with good signal conditions. This occasionally results in slight degradation in the accuracy, as seen in the case of the vertical accuracy, shown in Figure 6-14. This is acceptable given the significant reliability enhancement.

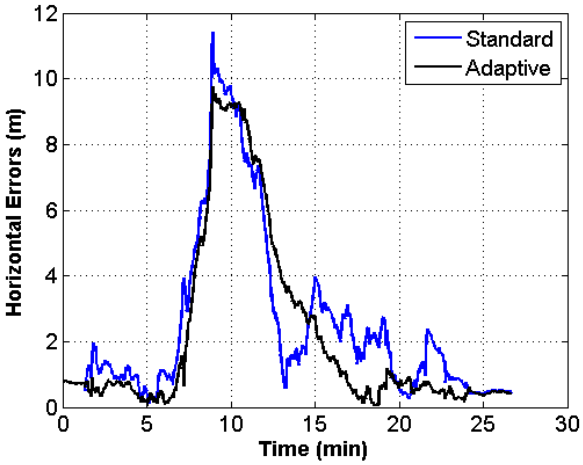

Figure 6-13. Horizontal Errors – OEM6+IMU (Open Sky Pedestrian Data-1)

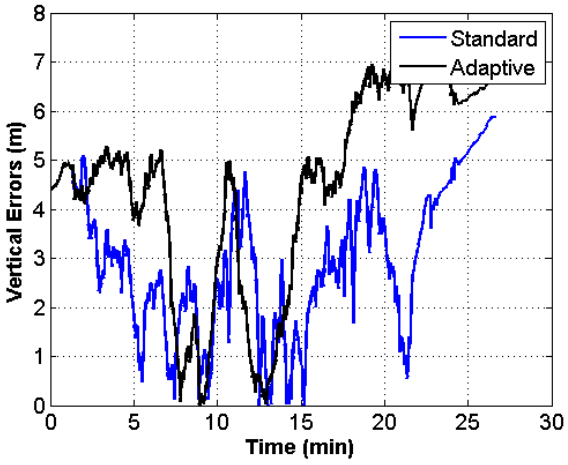

Figure 6-14. Vertical Errors – OEM6+IMU (Open Sky Pedestrian Data-1)

The RMS error values computed for the position solutions obtained using the two filters, for the three data sets, are summarized in Table 6-2.

Table 6-2. RMSE (Standard Vs Adaptive)

	RMSE (m)			
	Standard		Adaptive	
	Horizontal	Vertical	Horizontal	Vertical
Urban Canyon Vehicular Data	14.8	21.0	11.2	18.4
Urban Canyon Pedestrian Data-1	12.1	8.8	9.8	9.6
Open Sky Pedestrian Data-1	2.6	3.3	2.4	4.8

When it comes to navigating in areas like urban canyons, the GNSS measurements are not only corrupted by multipath but the visibility of satellites is also reduced. In such

environments, any rejection of GNSS measurements by the FDE will decrease the effect of GNSS updates in the integrated GNSS/INS filter. Moreover, this also leads to unavailability of the FDE scheme itself due to the lack of redundancy. Consequently, the unavailability of the FDE can degrade the reliability of the navigation solution. It is thus desirable to retain more measurements, albeit by choosing proper variances. The proposed scheme just does that and hence increases the availability of the GNSS measurements. The increase in the availability of range and Doppler measurements (after rejection of measurements by the FDE) on going from the standard to the adaptive approach is listed in Table 6-3.

Table 6-3. Measurement Rejection by the FDE

	Percentage of Measurements Rejected (%)			
	Standard		**Adaptive**	
	Range	**Doppler**	**Range**	**Doppler**
Urban Canyon Vehicular Data	0.12	8.32	0.05	6.7
Urban Canyon Pedestrian Data-1	1.0	18.7	0.98	6.13
Open Sky Pedestrian Data-1	~0	18.04	0	5.17

6.4 Assessment of the Use of *t* distribution for GNSS Measurement Errors

Prior to the incorporation of the algorithm proposed in Section 4.1 in an integrated navigation system, the suitability of using a heavy tailed distribution is examined through an initial test carried out using only GNSS range and Doppler measurements. The GNSS data collected in pedestrian mode using the OEM6 receiver under fairly open sky

conditions (Open Sky Pedestrian Data-1) is used for the assessment. Simulated errors were added to three satellite measurements for nearly 70% of the data in order to analyze the performance of the filters in presence of known faults. The simulated errors on the three satellites consisted of uniformly distributed pseudorange (ρ) errors ranging from 10 to 70 m and uniformly distributed Doppler ($\dot{\phi}$) errors ranging from -10 Hz to 10 Hz (±1.9 m/s). The results obtained with the navigation filter implemented with the assumption of *t* distributed measurement errors are compared against the results obtained with the assumption of normally distributed ($\mathcal{N}$) measurement errors. The comparisons are done for three cases, namely i) measurements without simulated errors, ii) measurements with simulated pseudorange errors and iii) measurements with simulated pseudorange as well as Doppler errors. RMS errors as well as reliability were calculated in local coordinates as shown in Table 6-4. It can be seen that the filter with the *t* distribution for measurement errors are least affected by the faults. It is also observed that, for the case with no added errors, the results are analogous for the two filter types. In fact, for an open sky data similar to the one used in this particular test, GNSS measurement errors follow the normal distribution more closely than the *t* distribution. This is supported by the slightly but not significantly better horizontal accuracy as well as better reliability along the local axes in case of the filter that assumes normal distribution for the measurement errors. Hence the *t* distribution is preferable for such an application.

Table 6-4. RMSE and Reliability (Open Sky Pedestrian Data-1 with Simulated Errors)

			No errors Added	Errors added on ρ	Errors added on ρ and $\dot{\phi}$
RMSE (m)	$\mathcal{N}$	**Horizontal**	2.6	6.4	6.5
		Vertical	2.3	7.9	7.5
	t	**Horizontal**	2.7	5.0	6.0
		Vertical	2.3	6.9	6.3
Reliability (%)	$\mathcal{N}$	**East**	93.4	73.0	68.4
		North	81.0	56.2	46.0
		Up	97.0	66.5	61.6
	t	**East**	72.3	71.9	70.0
		North	80.0	60.3	73.4
		Up	69.0	55.7	62.1

Taking the above result as an affirmation of the suitability of the *t* distribution for GNSS challenged environments, the algorithm proposed in Section 4.1 is incorporated in the GNSS/INS integrated system. The resultant algorithm module is assessed by analyzing the results obtained by processing the two pedestrian data sets collected in harsh environments, namely Urban Canyon Pedestrian Data-1 and Natural Canyon Pedestrian Data-1.

The GPS/INS integrated navigation system with *t* distributed GNSS measurement errors is referred to as the 'VB filter" for it uses the Variational Bayes technique in its realization (Webb & Copsey 2011). Moreover, when the algorithm module with *t* distributed GNSS measurement errors is combined with the covariance adaptive model of Section 4.2, the resulting module is termed as "VB Adaptive filter". The following analyses in this section, thus, presents comparative assessment of three algorithms, namely (i) "Standard filter",

(ii) “VB filter” and (iii) “VB Adaptive filter”. Furthermore, since carrier to noise ratio (C/N_o) based weighting has been found to be more robust in harsh GNSS signal conditions, the Sigma-ε variance model discussed by Wieser et al (2005) is used to scale the GNSS range and Doppler measurements in all three filters.

A rough idea of the nature of measurement discrepancies in the urban canyon data (Urban Canyon Pedestrian Data-1) was developed through the assessment of pseudorange measurements in Figure 6-6. To further illustrate the nature of signal degradation, the carrier to noise ratios (C/N_o) of available GNSS measurements are plotted in Figure 6-15 along with the average of all the C/N_o values at each epoch plotted in dark green. It is observed that the C/N_o values are very low at 30 dB-Hz for many measurements in the middle section of the test duration. Such low values will result in higher measurement noise. This further highlights the limitations imposed by the test environment in terms of signal conditions.

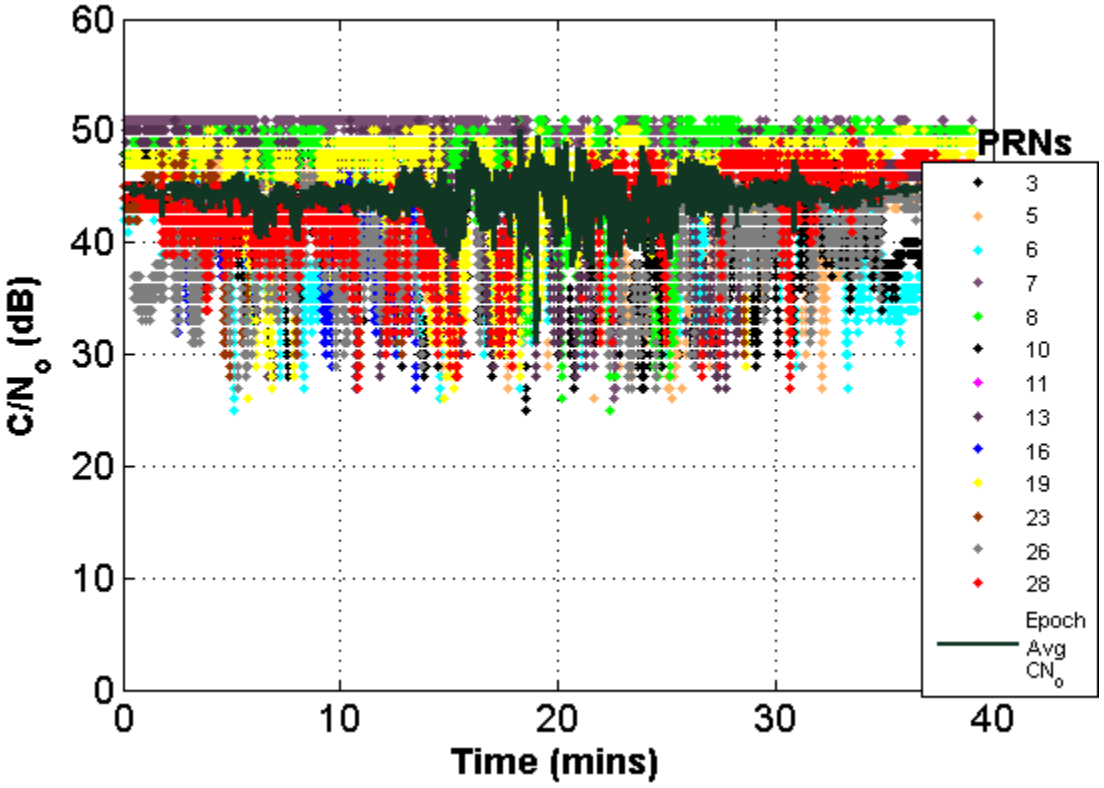

Figure 6-15. C/N$_o$ Values – OEM6 (Urban Canyon Pedestrian Data-1)

The performances of the above mentioned three filters are first inter-compared by computing absolute values of horizontal and vertical errors. In order to confine the analysis to degraded environments, the errors are plotted only for the section of the data in which the GNSS conditions are very harsh and the errors are more severe. In this regard, the portions of the data, especially at the beginning and at the end, during which the user was static in a relatively open sky condition with many line of sight (LOS) GNSS measurements are omitted. Moreover, it is also known that the error values can grow very large corresponding to the times for which the satellite geometry is very poor as indicated

by the dilution of precision. Thus, to segregate the effect of biased and diffused measurements from that of poor satellite geometry, the error statistics are computed only for the times in which the position dilution of precision (PDOP) values are less than 10. The PDOP values, plotted alongside the errors in Figure 6-16 and Figure 6-17, also gives an idea of the effect of masking in the urban environment.

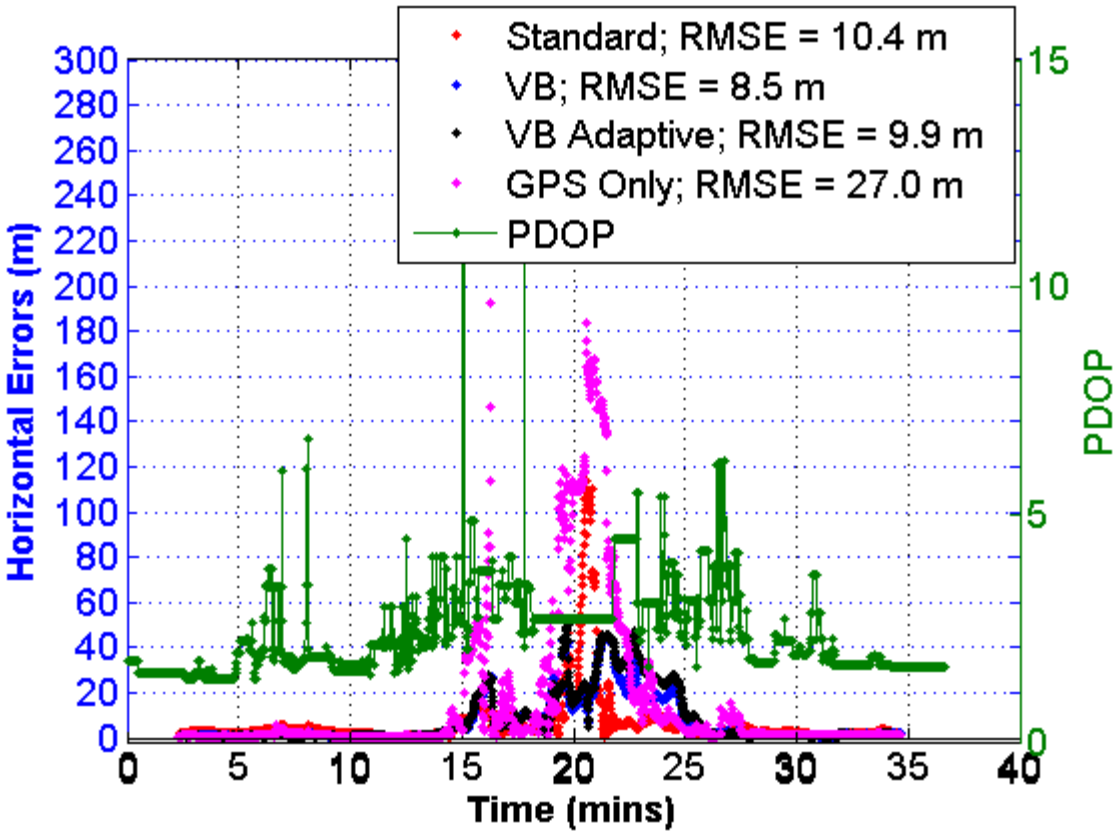

Figure 6-16. Horizontal Errors (VB and VB Adaptive) – OEM6+IMU (Urban Canyon Pedestrian Data-1)

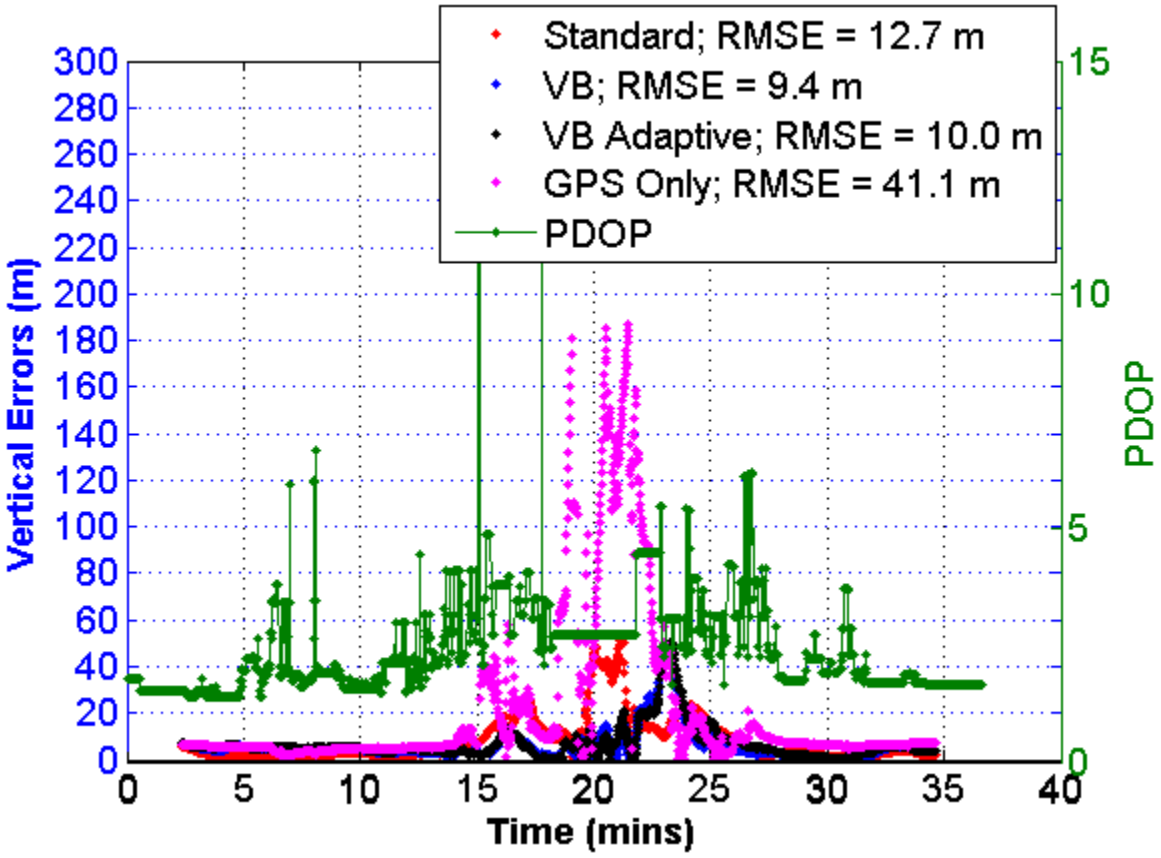

Figure 6-17. Vertical Errors (VB and VB Adaptive) – OEM6+IMU (Urban Canyon Pedestrian Data-1)

The above figures show that the errors along both horizontal and vertical directions are smaller in the case of VB filters, thus indicating the robustness of using the *t* distribution in environments with multipath laden GNSS measurements. The maximum horizontal error decreases by a factor of about 2.5 when using VB and VB Adaptive as compared to the Standard filter. The accuracy seems to slightly degrade in the adaptive case. This is most likely due to subtle over-bounding of the assumed GNSS error distribution. Such over-bounding decreases the weight of the GNSS measurements. This de-weighting often leads to the dilution of unaffected measurements, thus degrading accuracy.

However, as observed in the previous section, the adaptive module very significantly improves the reliability of the navigation solution.

The above figures also include error plots for the GPS only solution which is realized using an extended Kalman filter (EKF) that assumes a normal distribution for range and Doppler measurements. A standard residual based FDE is also implemented to detect and eliminate aberrant measurements. The error plots for the GPS only solution gives an idea about the GNSS signal conditions in the test environment. It is observed from the error plots that there are a few instances where the errors are in the range of 200 m, thus leading to much higher RMSE as compared to the integrated GPS/INS solutions.

The algorithm modules are further compared in terms of another critical performance parameter, namely reliability. Figure 6-18 shows the average reliability values along the axes of the local plane for the three filters discussed above. It is observed that the reliability values are lower for the Standard filter. This is a common problem with standard Kalman filters, especially in integrated systems like GPS/INS where the estimated accuracy of the navigation solution is often optimistic. However, the reliability values are found to improve with the VB filter and even further with the VB Adaptive filter, thus mitigating the limitations of standard Kalman filters. These reliability results further indicate that, among the three filters, the VB Adaptive filter best characterizes the true GNSS noise characteristics.

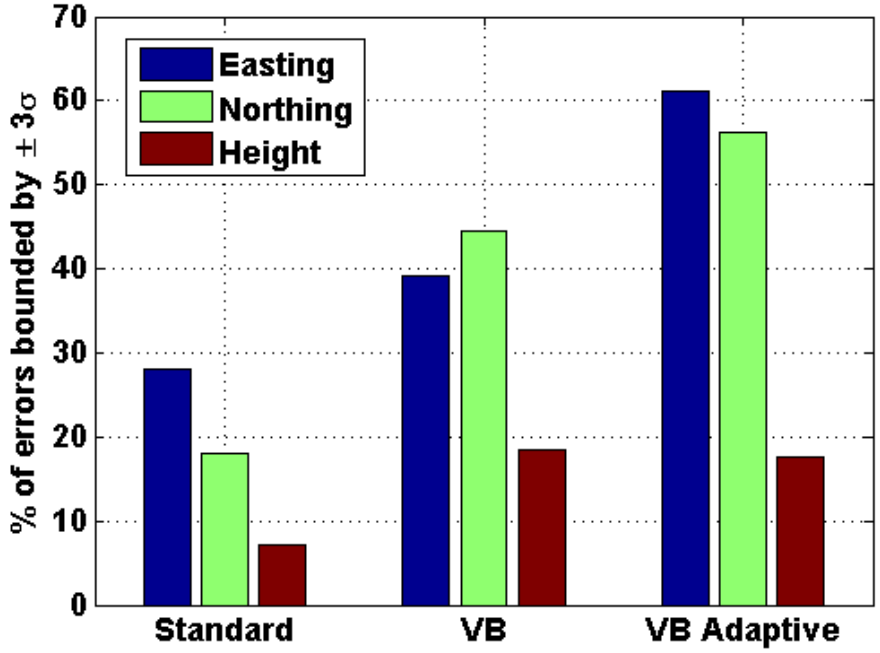

Figure 6-18. Reliability of Navigation Solution – OEM6+IMU (Urban Canyon Pedestrian Data-1)

As discussed in the previous section, availability of GNSS measurements is another key parameter to be assessed in such signal deprived environment. Since the *t* distribution inherently tends to retain more measurements, the availability of GNSS measurements was found to increase when using the *t* distribution. The percentage of range measurements rejected by the FDE decreased from 1.0 % to 0.5 % when going from the Standard filter to the VB Adaptive filter. The standard approach identified 18.7 % of the Doppler measurements as faults and subsequently rejected them. This indicates that the Doppler measurements had an optimistic variance associated with the observation in comparison to the internal solution. This statistic pointedly shows how the standard method is insufficient since the system is incapable of handling the increased variance in

the degraded environment. The VB filter alternatively rejected only 0.3 % of the Doppler measurements.

Additionally, if a personal navigation system is also required to provide GNSS integrity parameters such as horizontal and vertical integrity limits, then a certain minimum requirement in terms of GNSS measurement availability must be met. When using only GPS, as in this work, a minimum of 5 GPS measurements must be available. However, in signal challenged environments, the available GNSS measurements are often less than 5 due to signal masking. Moreover, improper assumption of measurement noise statistics can also add to this unavailability. The availability of the integrity information for the three filters discussed above is tabulated in Table 6-5. Since there are only a few epochs with PDOP higher than 10, the exclusion of those epochs did not change the availability values by more than 0.1 %. Thus the tabulated availability values were computed without discarding those epochs. The tabulated values indicate a slight improvement in terms of availability of GNSS integrity information with the VB filters as compared to the Standard filter. However, for users navigating in GNSS challenged environments for a prolonged duration of time, such improvement could be magnified.

Table 6-5. Availability of GNSS Integrity Information – OEM6 (Urban Canyon Pedestrian Data-1)

	Standard	**VB**	**VB Adaptive**
Availability Percentage of Integrity Information	78.3	80.1	79.5

The proposed algorithm modules are further assessed using the pedestrian data collected in a natural canyon (Natural Canyon Pedestrian Data-1). The GNSS data collected using two different receivers, namely an OEM6 and u-blox6 are used for the analysis. The use of data from different GNSS receivers further validates the performance analysis of the proposed algorithms. Similarly, the IMU data collected using the external sensor pod (ADIS16488), mounted on top of the backpack, is used. During the analysis, the GNSS data collected using the two receivers are integrated separately with the IMU in order to obtain the integrated solutions for the three filters, namely Standard, VB and VB Adaptive.

Firstly, the range errors were computed using a similar technique as that for the urban data set using the GNSS data from the OEM6 receiver. These range errors, plotted in Figure 6-19, show that a significant portion of the data is affected by biased measurements, which at some epochs go as high as nearly 120 m.

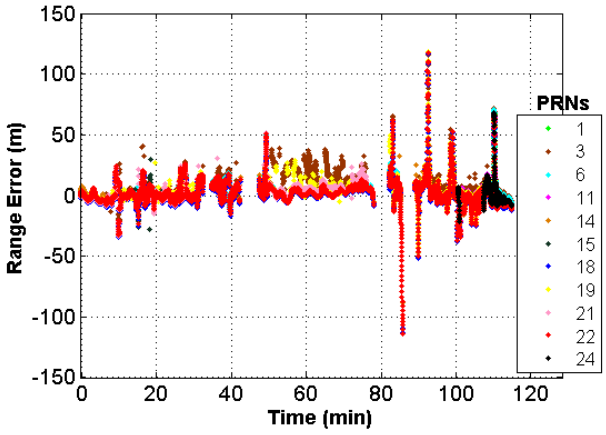

Figure 6-19. Pseudorange Errors – OEM6 (Natural Canyon Pedestrian Data-1)

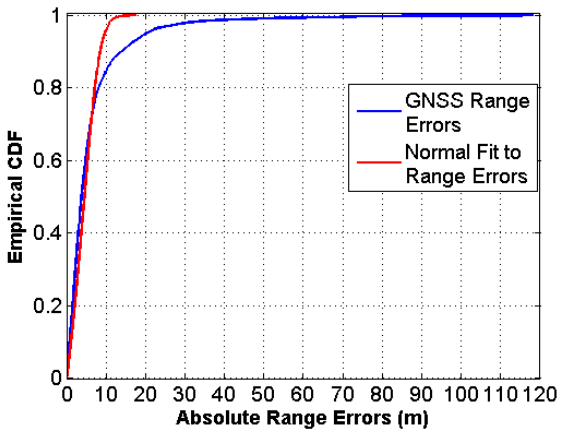

Figure 6-20. CDF of Pseudorange Errors – OEM6 (Natural Canyon Pedestrian Data-1)

Moreover, a cumulative density function (CDF) of the absolute values of the range errors is also plotted in Figure 6-20 along with the CDF of absolute values of the normal fit to the range errors. It can be observed from the figure that there are not only errors with significant magnitude but there is also a high non-conformity between the two CDFs. This indicates that assuming a normal distribution for such errors is likely to lead to a sub-optimal navigation solution. The deviation of the range error distribution from the normal distribution is obvious from the normal probability plot of the range errors shown in Figure 6-21. The deviation from the straight line indicates the departure from the normal distribution.

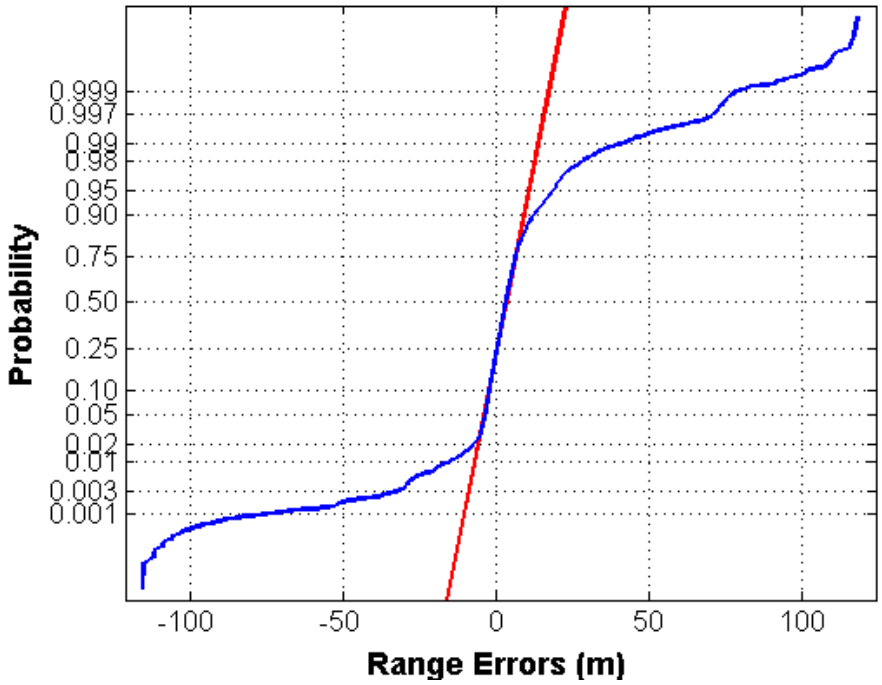

Figure 6-21. Normal Probability Plot of Range Errors – OEM6 (Natural Canyon Pedestrian Data-1)

The nature of signal degradation in the natural canyon is further illustrated through the carrier to noise ratios of the GNSS signal collected using the OEM6 receiver, as plotted in Figure 6-22.

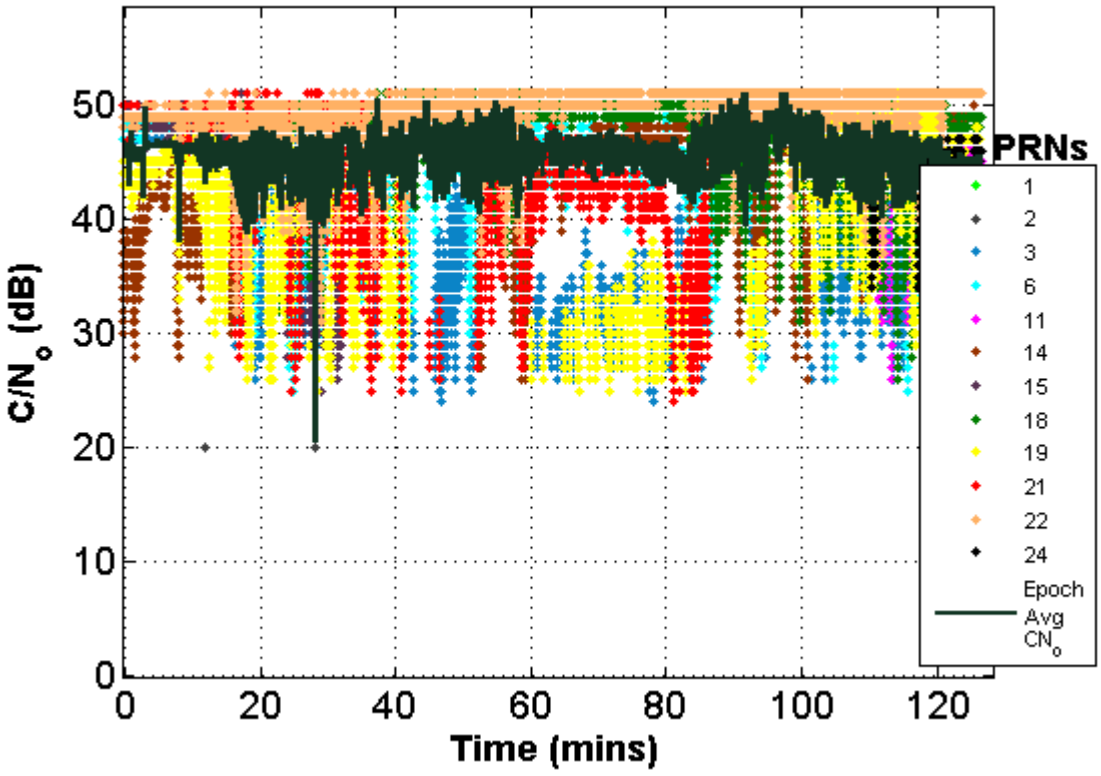

Figure 6-22. C/N$_o$ Values – OEM6 (Natural Canyon Pedestrian Data-1)

With a broad idea about the nature of signal degradation in the test environment, the integrated solutions for the three filters (Standard, VS and VB Adaptive), obtained separately using the GNSS data from u-blox6 and OEM6, are compared in terms of the position accuracies. The horizontal and vertical errors obtained using GNSS data from the u-blox6 receiver integrated with the IMU data are shown in Figure 6-23 and Figure 6-

24. These errors are computed following the same procedure as that for the previous data set, neglecting the static LOS data at the two ends of the canyon. Moreover, the data corresponding to the time epochs with very high PDOP values (PDOP >10) are also discarded during the position error computation. As before, the error values obtained for the GPS only solutions and the PDOP values are also included.

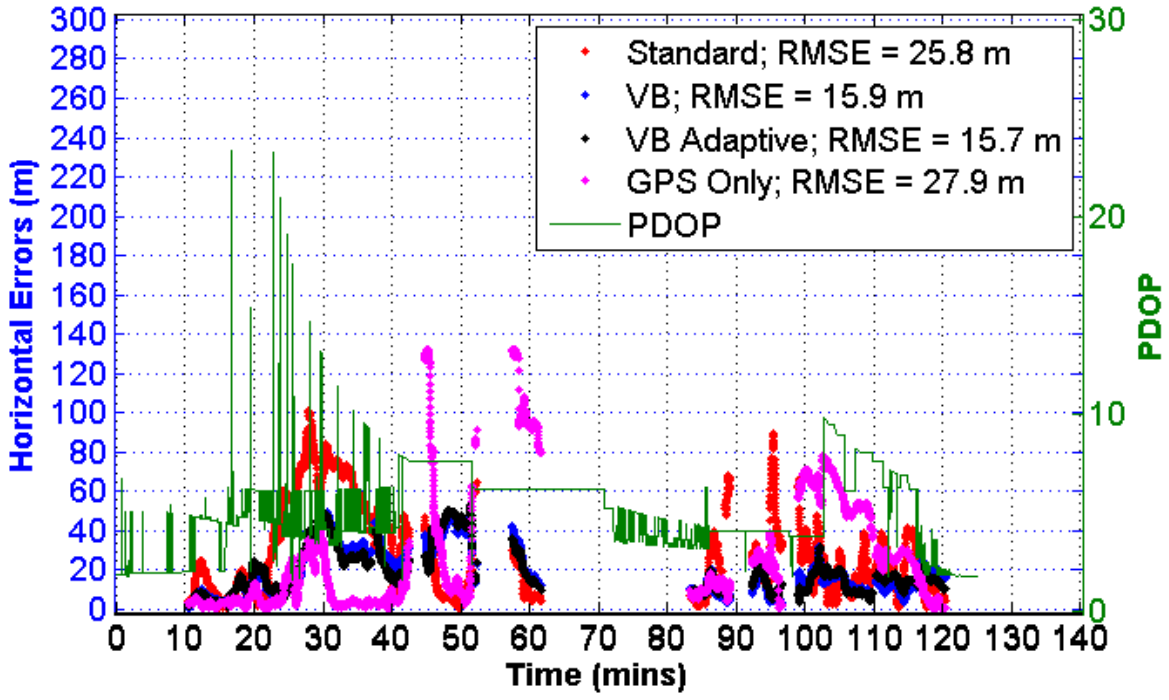

Figure 6-23. Horizontal Errors – ublox6+IMU (Natural Canyon Pedestrian Data-1)

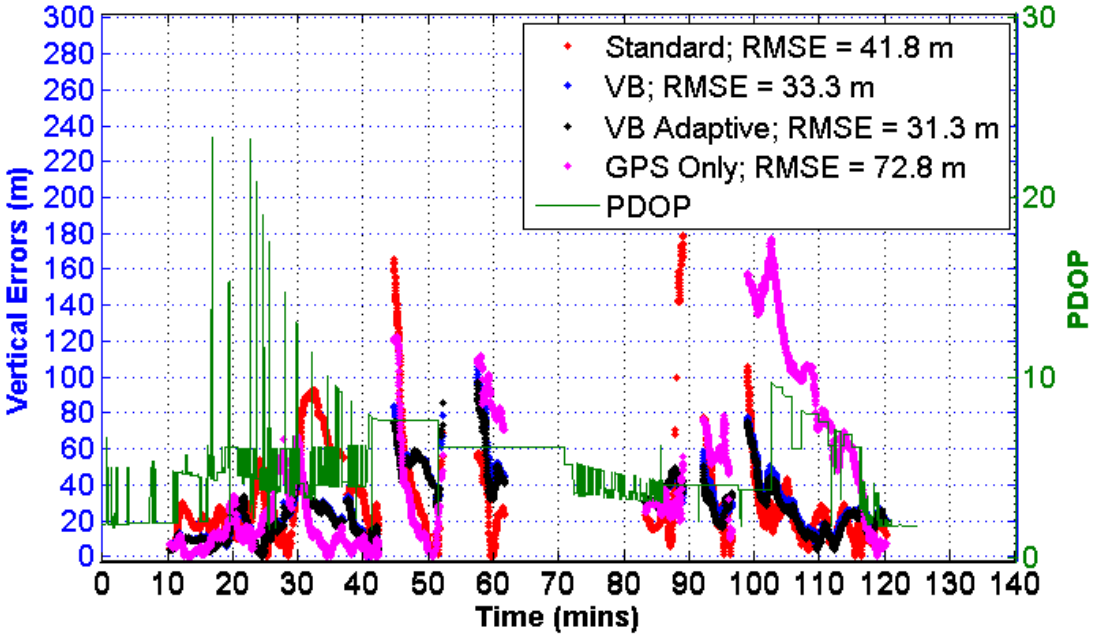

Figure 6-24. Vertical Errors – ublox6+IMU (Natural Canyon Pedestrian Data-1)

A considerable improvement in accuracy can be observed when using the proposed schemes as compared to the Standard filter. The maximum errors are also found to decrease significantly with the proposed schemes. The reliability values for the same data set, as depicted in Figure 6-25, again shows that there is an improvement in the reliability of the navigation solution with the proposed VB Adaptive filter.

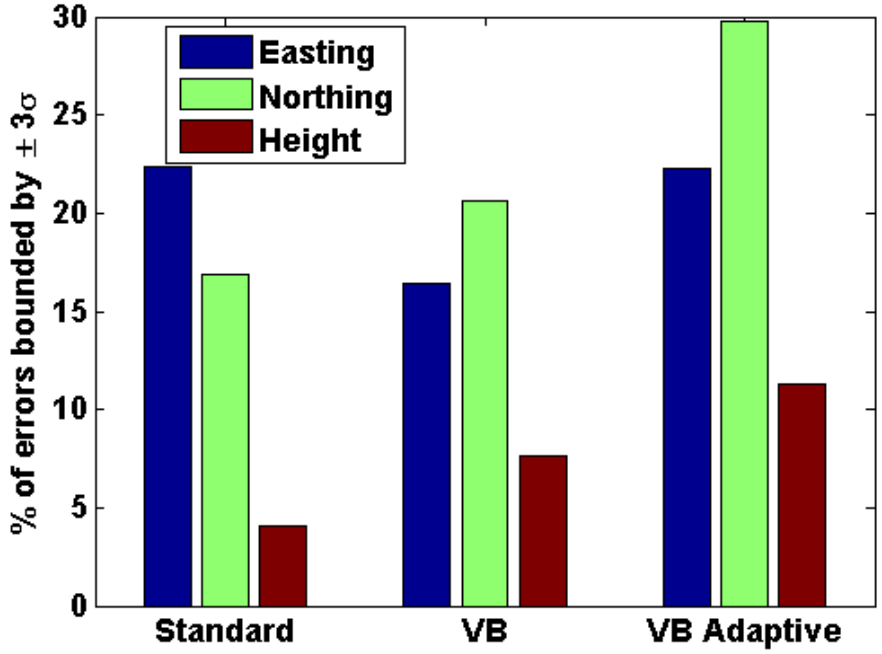

Figure 6-25. Reliability of Navigation Solution – ublox6+IMU (Natural Canyon Pedestrian Data-1)

The position errors and reliability values are re-calculated by processing the GNSS data collected using the OEM6 receiver tightly integrated with the IMU data. The results obtained are tabulated in Table 6-6.

Table 6-6. RMSE and Reliability – OEM6+IMU (Natural Canyon Pedestrian Data-1)

	RMS Errors (m)		Reliability (%)		
	Horizontal	**Vertical**	**Easting**	**Northing**	**Height**
Standard	12.2	12.1	32.7	32.5	36.7
VB	16.4	12.1	56.7	50.3	38.9
VB Adaptive	12.0	11.4	57.7	50.9	42.4

The above table indicates a slight improvement in accuracy when using the proposed scheme. However, there is a considerable improvement in the reliability of the navigation solution. This further validates the claim that the proposed algorithm, which adapts the covariance of the *t* distributed GNSS measurement errors, characterizes the GNSS measurement errors more closely to its true behaviour.

Finally, the availability of integrity information was also computed as before. As with the previous data set, the availability of integrity was again found to improve when using the proposed scheme. The improvement in availability is summarized in Table 6-7 for the GPS/INS solutions obtained using both OEM6 and u-blox6 receivers.

Table 6-7. Availability of GNSS Integrity Information (Natural Canyon Pedestrian Data-1)

		Standard	VB	VB Adaptive
Availability of Integrity Information (%)	**OEM6**	71.9	72.0	71.9
	u-blox6	65	74.5	74.5

6.5 Assessment of Pre-Filter Sensor Validation Scheme

The pre-filter sensor validation scheme, presented in Chapter 5, is assessed through the simulation of faults in various sensor measurements. The following sub-sections evaluate the performance of the proposed algorithm module in the presence of faults in individual sensor measurements.

6.5.1 Simulation of Faults in Accelerometers

As discussed in Section 3.2.3, MEMS inertial sensors can potentially suffer from faults like stiction which can cause the IMU to output spurious measurements. The performance of PNDs that use such sensors can severely degrade if the outliers in the inertial sensor measurements go undetected. Hence, to assess the capability of the pre-filter sensor validation scheme in detecting such faults, a spurious effect is simulated in the accelerometer measurements in the open sky data collected at Nose Hill Park (Open Sky Pedestrian Data-2). The faults are simulated through addition of a constant acceleration of 0.2 m/s^2 in all axes. Such faults are simulated in the accelerometer measurements for five minutes, occurring between the 10^{th} and the 15^{th} minute, as shown in the vertical acceleration plot in Figure 6-26.

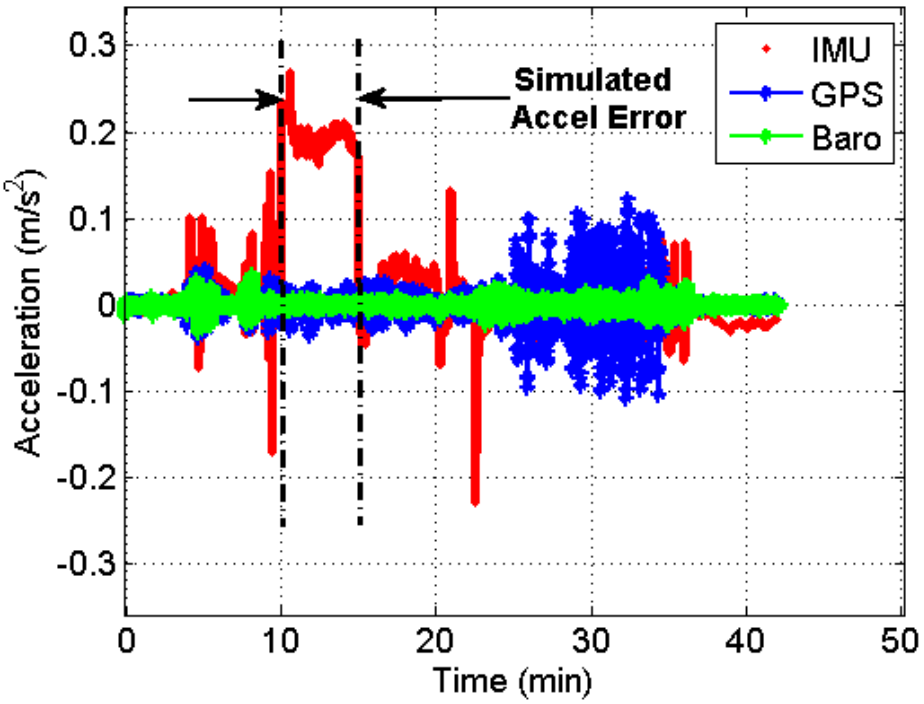

Figure 6-26. User Acceleration along Vertical Direction (Open Sky Pedestrian Data-2)

Pedestrian navigation is typically characterized by a high order of short term dynamics. In the case of a strap-down INS configuration realized for such high dynamic applications, even a small error in attitude (especially roll and pitch) can result in significant errors in the computation of user acceleration, due to the infiltration of the gravity component. This often induce large spikes in the vertical acceleration of the form observed in the above figure that occur even during the times when no fault is simulated. The presence of such spikes makes the acceleration comparison more challenging.

The faults in the accelerometer measurements has to be detected by the acceleration validation block in Figure 5-1. This is done through the computation of consistencies

between the accelerations obtained using the IMU with those obtained using the barometer and GPS. The consistency values, computed as Bhattacharyya coefficients (which assume values between 0 and 1, 1 being the highest consistency) using equation 4-6, are plotted as a function of time in Figure 6-27 and Figure 6-28. It is observed that, during the period of simulated faults, the accelerometer measurements are highly inconsistent with the barometer and GPS measurements in terms of the observed inter-sensor equivalent, namely the user acceleration. As a result, the combined consistency values in Figure 6-29 are also consistently below the threshold during the occurrence of accelerometer faults. However, as discussed in Chapter 5, a careful approach is adopted before declaring a fault in the key sensors, namely accelerometers and gyroscopes. Thus, unlike the case with other sensors like barometers and magnetometers, the accelerometer measurements are not immediately deemed invalid when the combined consistency value is below the threshold. The accelerometer is deemed to be generating spurious measurements only when the combined consistency values are below the threshold for at least 80 percent of the epochs during a time window of 30 second. A moving average filter with a 30 s window in the accelerometer validation block keeps track of the percentage of epochs at which faults were detected in the accelerometers (i.e. percentage of epochs when the combined consistencies were below the threshold). Figure 6-30 shows the output of this moving average filter as a function of time. It is observed from this figure that soon after the simulated faults are introduced, starting at the 10^{th} minute, the percentage rises above 80. It is at this point that the accelerometer is deemed to be outputting faulty measurements and a red alert flag is generated. Moreover, it is also observed that the combined consistency values are often below the

threshold even at times when no fault was simulated. This mostly correspond to the times when there are spikes in the user acceleration values obtained from the IMU, potentially causing the validation scheme to wrongly declare fault in the accelerometers. However, the relaxed approach used while declaring fault in the accelerometer avoids the possible false alarm that can result due to such short term spikes.

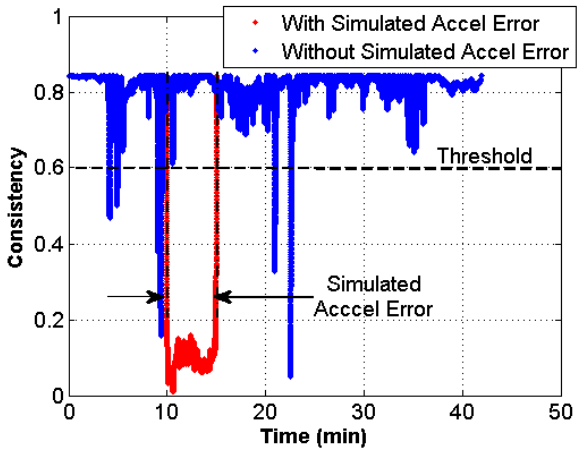

Figure 6-27. Acceleration Consistency between IMU and Barometer – With Simulated Faults in Accelerometer (Open Sky Pedestrian Data-2)

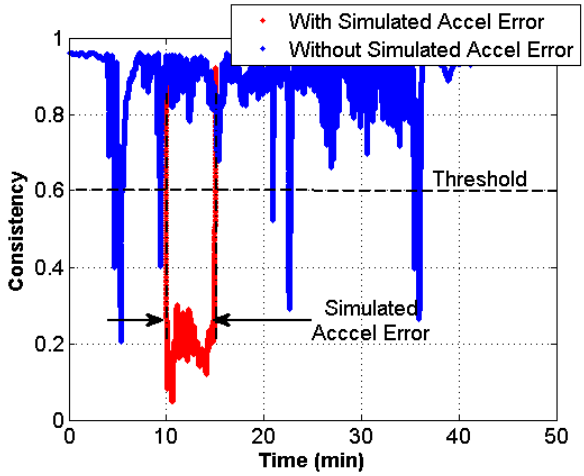

Figure 6-28. Acceleration Consistency between IMU and GPS – With Simulated Faults in Accelerometer (Open Sky Pedestrian Data-2)

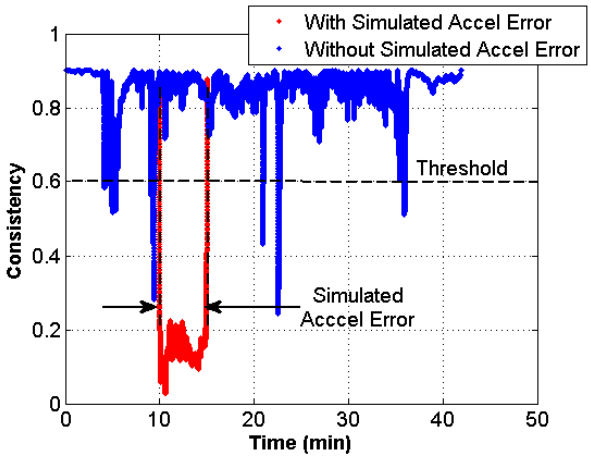

Figure 6-29. Combined Consistency for Validity of Accelerometer – With Simulated Faults in Accelerometer (Open Sky Pedestrian Data-2)

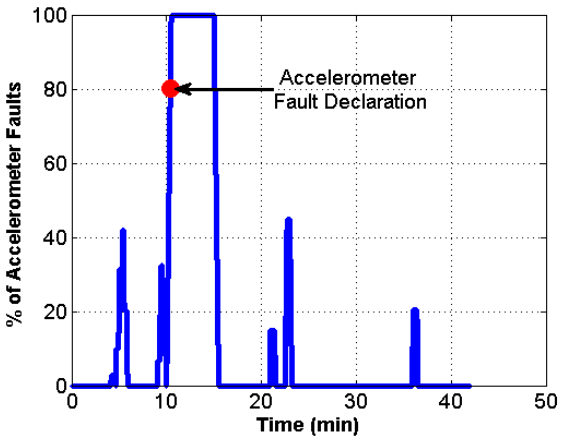

Figure 6-30. Percentage of Epochs with Combined Consistencies below Threshold during 30s Window – With Simulated Faults in Accelerometer (Open Sky Pedestrian Data-2)

6.5.2 Simulation of Faults in Barometer

The analysis of the barometer data collected during windy conditions, as presented in Section 3.2.2, showed that the faults introduced in the barometer measurements due to the wind results in both bias and noise in the barometer derived altitude. Hence, in order to assess the sensor validation scheme during similar conditions, faults of similar nature are simulated in the clean barometer data, collected in an open area with low wind conditions (Open Sky Pedestrian Data-2). The faults simulated in the barometer measurements can be modeled as

$$\varepsilon_{Sim,Baro}(t) = at + bt^2 + n_{Wind}\,\text{Pa} \qquad \textbf{6-1}$$

where $at + bt^2$ represents the time varying bias component defined by the constant terms a and b, and $t \in [0,1\,\text{min})$. n_{Wind} is the random component, namely normally distributed barometric noise with a similar variance as obtained for the windy data of Section 3.2.2. The minute long simulated error, represented by Equation 6-1, is repeated for fifteen minutes, from the 10th minute to 25th minute. The resulting errors in altitude can be observed from the barometer derived altitude plot in Figure 6-31 and its zoomed version in Figure 6-32.

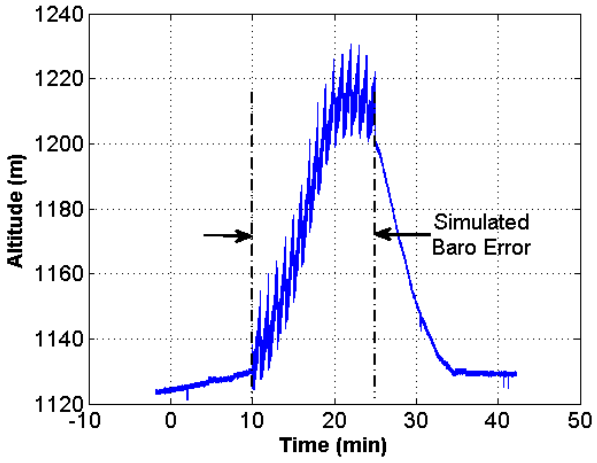

Figure 6-31. Barometer Derived Altitude – With Simulated Faults in Barometer (Open Sky Pedestrian Data-2)

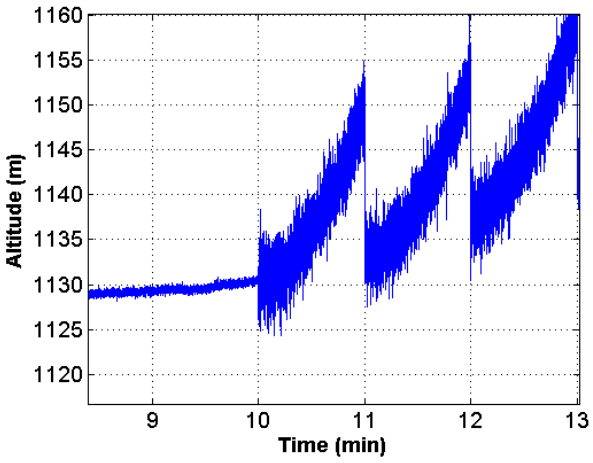

Figure 6-32. Zoomed Altitude Plot – With Simulated Faults in Barometer (Open Sky Pedestrian Data-2)

As with the accelerometers, the simulated barometer faults also have to initially go through the accelerometer validation block. Although the simulated barometer faults are quite severe in nature, they should not affect the validity of the accelerometers. To investigate the effect of such faults, the acceleration consistencies are computed as

before and are plotted in Figure 6-33 through Figure 6-35. During the presence of simulated faults in the barometer, the consistencies between user acceleration along the vertical direction obtained from the IMU and that obtained from the barometer, as shown in Figure 6-33, are very poor and often below the threshold value. The consistency between the user accelerations obtained using the IMU and the GPS, however, are not affected. The combined consistencies, shown in Figure 6-35, indicate the presence of many epochs during which the consistency values are below threshold. This is due to the severity of the simulated barometer errors. However, these faults are not enough to cause a false alarm in the acceleration validation as illustrated by the percentage of accelerometer faults shown in Figure 6-36.

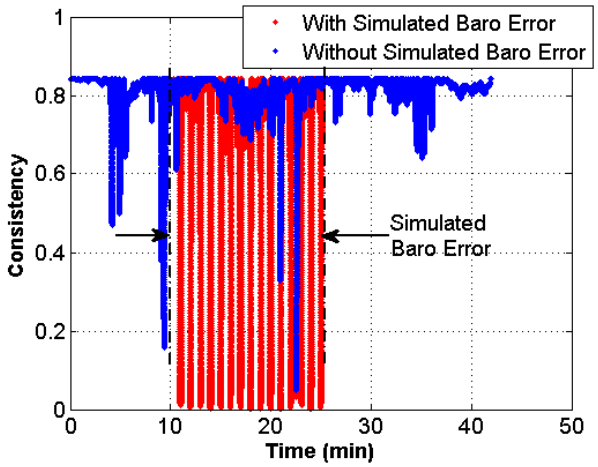

Figure 6-33. Acceleration Consistency between IMU and Barometer – With Simulated Faults in Barometer (Open Sky Pedestrian Data-2)

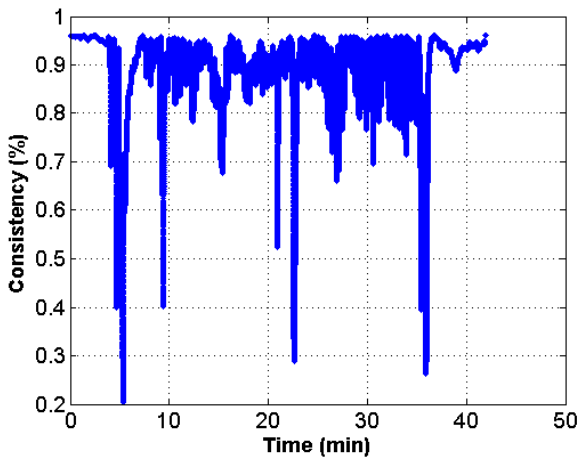

Figure 6-34. Acceleration Consistency between IMU and GPS – With Simulated Faults in Accelerometer (Open Sky Pedestrian Data-2)

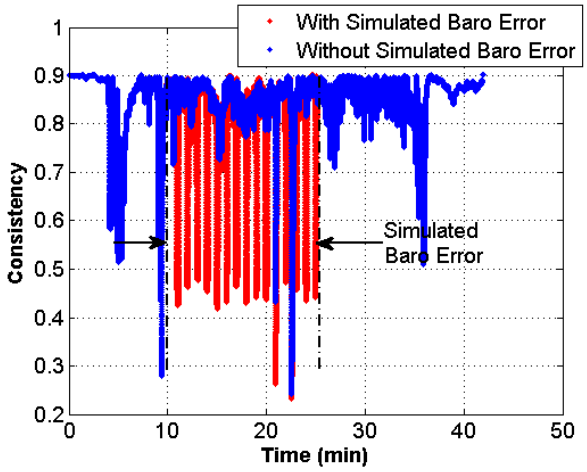

Figure 6-35. Combined Consistency for Validity of Accelerometer – With Simulated Faults in Barometer (Open Sky Pedestrian Data-2)

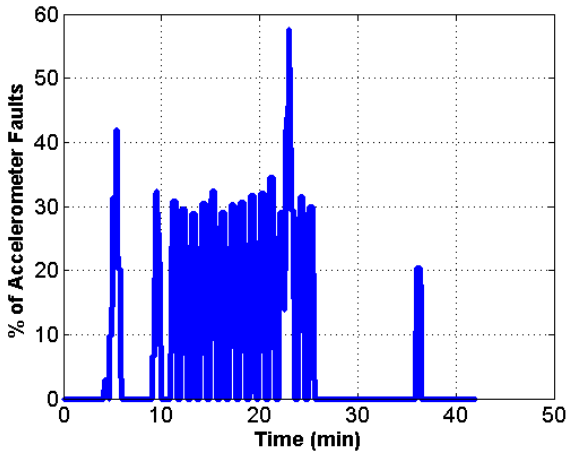

Figure 6-36. Percentage of Epochs with Combined Consistencies below Threshold during 30s Window – With Simulated Faults in Barometer (Open Sky Pedestrian Data-2)

After passing through the accelerometer validation block, the barometer data is then passed to the barometer validation block before it could be used in the integration filter. The barometer validation block prevents the faulty barometer measurements from entering the integration filter. The effectiveness of such validation scheme is examined by computing the accuracy of the navigation solution in presence of the above simulated barometer measurement errors. Two integrated solutions are computed using GPS, IMU and barometer, namely one with the pre-filter sensor validation scheme and the other without the validation scheme. The position errors of the two navigation solutions are plotted along the horizontal and vertical directions in Figure 6-37 and Figure 6-38. Moreover, the RMS errors are also tabulated in Table 6-8.

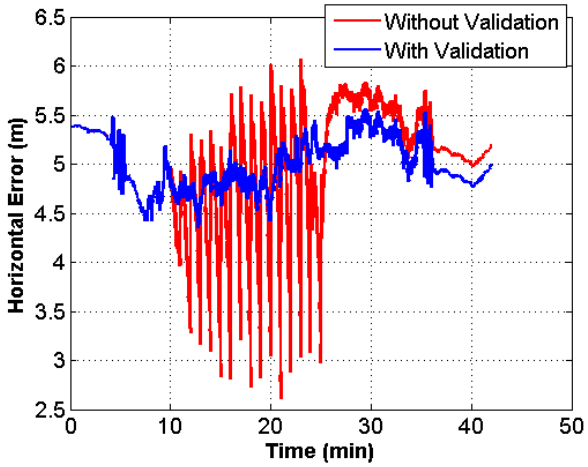

Figure 6-37. Horizontal Errors – OEM6+IMU+Baro (Open Sky Pedestrian Data-2)

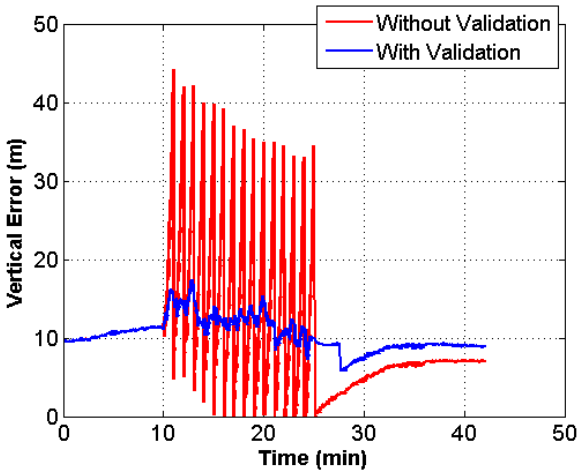

Figure 6-38. Vertical Errors – OEM6+IMU+Baro (Open Sky Pedestrian Data-2)

Table 6-8. RMSE and Maximum Errors – OEM6+IMU+Baro (Open Sky Pedestrian Data-2)

	RMS Errors (m)		RMS Errors – Simulation Period (m)		Maximum Error (m)	
	Horizontal	**Vertical**	**Horizontal**	**Vertical**	**Horizontal**	**Vertical**
Without Validation	3.6	12.8	3.3	18.6	6.1	44.2
With Validation	3.6	10.6	3.3	12.4	5.6	17.5

From the above error plots it is observed that, in the absence of the pre-filter sensor validation scheme, the position solution becomes highly erroneous. The above table shows the RMS values of the position errors computed for the whole trajectory as well as only at the times when the barometer errors are simulated. Due to the nature of the errors, however, despite having considerable fluctuations in the position solution, the RMS value

of the errors are not very different as compared to the solution where the sensor validation scheme was included. Nonetheless, as shown in the above table, the use of sensor validation scheme significantly (from 44 to 18 m) reduces the maximum error along the vertical direction by preventing the infiltration of simulated barometer faults into the integration filter. From the above analysis, one can conclude that in the case of a sustained wind, the position solution can deviate significantly if the pre-filter sensor validation scheme is not used. This highlights the importance of using such sensor validation scheme in personal navigation devices.

As indicated by the above results, the barometer validation scheme is very effective in detecting the faults arising in the barometer due to wind or short term pressure jumps associated with the user dynamics. However, in the case of low frequency barometric errors arising due to pressure variations over a longer duration of time, the proposed scheme will fail to detect the error as the rate of change in barometric pressure derived altitude due to such variation is negligible. This could potentially lead to a significant bias in height without being detected by the sensor validation scheme should a system be used continuously for long periods of time without differential barometric aiding.

6.5.3 Simulation of Faults in Magnetometer

Similar to the above sub-sections, faults are simulated in the magnetometer measurements in order to assess the performance of the magnetometer validation block of Figure 5-1. Normally distributed random errors with a standard deviation of 0.03 gauss are added to the magnetometer measurements for a period of five minutes, from the 10th

minute to the 15th minute. The simulated errors are on par with the auxiliary magnetic fields arising from typical magnetic perturbation sources in urban environments.

The sensor validation scheme, proposed in Chapter 5, validates the magnetometer measurements through the comparison of two inter-sensor equivalents, namely the angular velocity and the magnetic field strength. Figure 6-39 shows the angular velocities along the x-axis, obtained using the gyroscope as well as those derived from the magnetometer measurements. The zoomed plot in Figure 6-40 shows that the two angular velocities are in close agreement with each other. However, during the times when errors are simulated in the magnetometer measurements, the consistency of the two angular velocities degrades. This is shown by the angular velocity plot in Figure 6-41, which is zoomed during the period when faults are simulated.

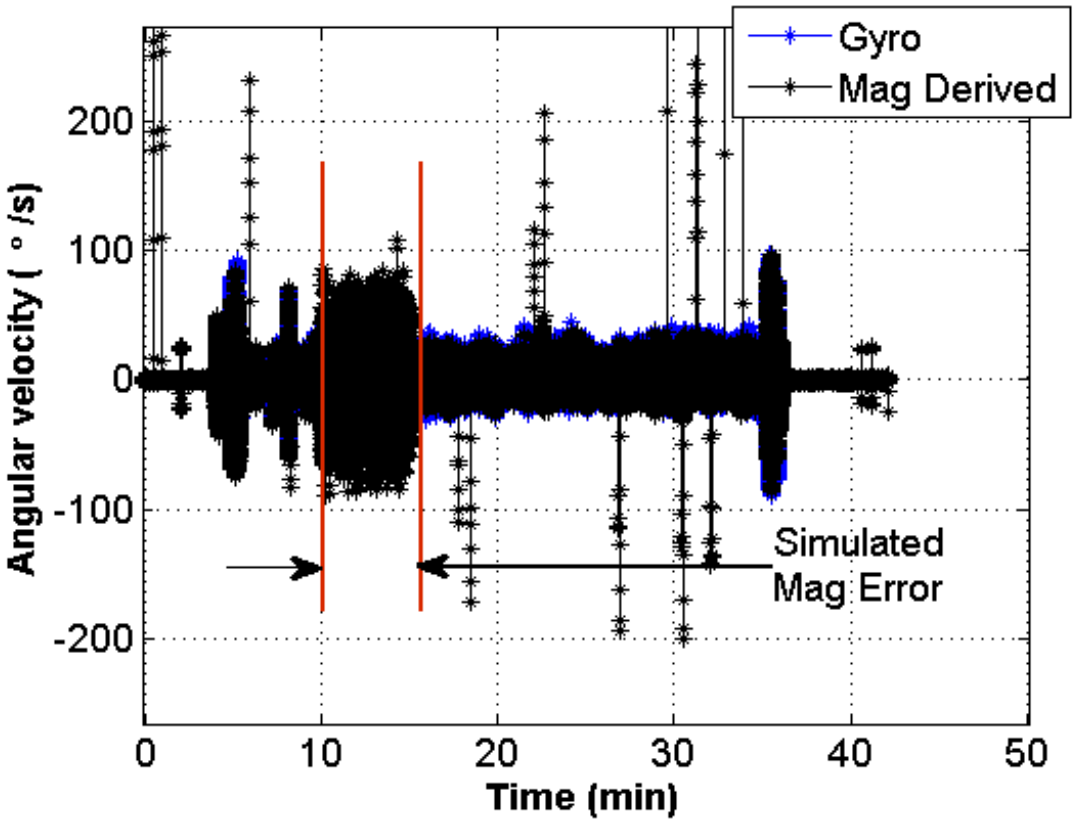

Figure 6-39. Angular Velocities along X-axis – With Simulated Magnetometer Error (Open Sky Pedestrian Data-2)

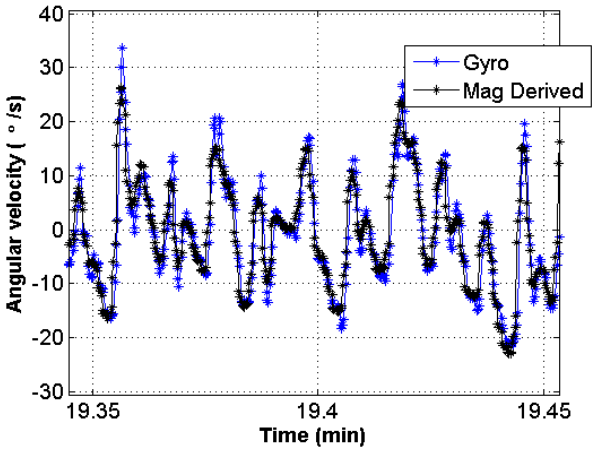

Figure 6-40. Angular Velocities along X-axis – Zoomed at Times Without Simulated Errors

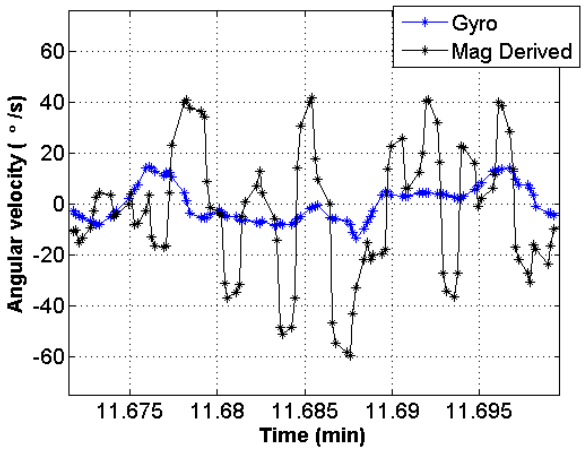

Figure 6-41. Angular Velocities along X-axis – Zoomed at Times With Simulated Errors

Throughout the duration of the simulated magnetometer faults, the magnetometer measurements were found to be highly inconsistent with both reference geomagnetic field as well as the gyroscopes, when compared in terms of the relevant inter-sensor equivalents. The combined consistency values, shown in Figure 6-42, indicate many epochs during which the consistencies are below the threshold, thus correctly leading to the rejection of faulty magnetometer measurements.

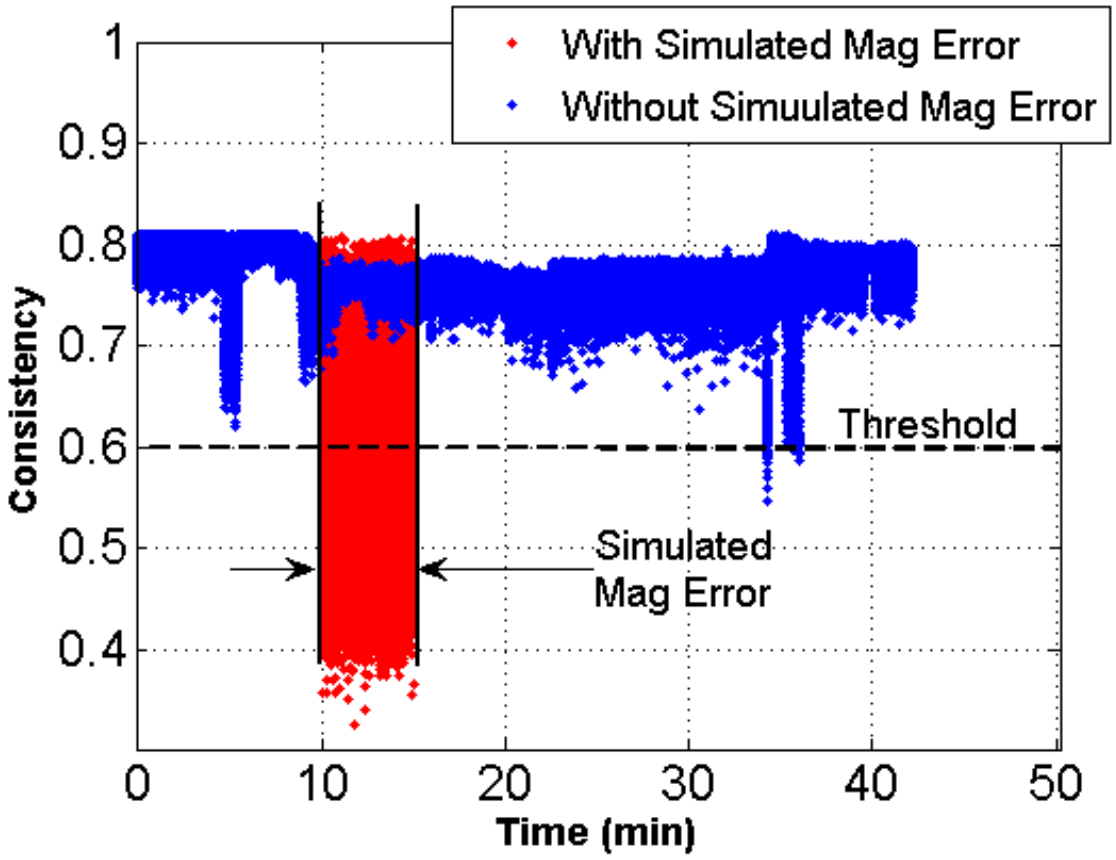

Figure 6-42. Combined Consistency for Validity of Magnetometer – With Simulated Faults in Magnetometer (Open Sky Pedestrian Data-2)

For the above data set, despite the simulation of faults in the magnetometer, due to very good GPS signal conditions, the position solution did not degrade even without the use of the sensor validation scheme. This, however, will be very different in scenarios where GPS is degraded. Hence, to analyze the effect of such magnetometer faults on the navigation solution during harsh GPS conditions and to assess the capability of the sensor validation scheme to improve the performance during such scenarios, magnetometer faults are simulated in a pedestrian data set collected in a natural canyon

environment (Natural Canyon Pedestrian Data-2). A natural canyon environment represents a scenario where a navigation system can get high benefits from using the magnetometer. The heading updates from the magnetometer can be very useful on improving the performance of the navigation system in such scenarios with degraded GPS conditions. Moreover, unlike urban environments, natural canyons or dense forests do not have the problem of magnetic perturbations. Thus, for the assessment of the sensor validation scheme in such scenarios, magnetic faults of the nature similar to the one simulated for the previous data set is simulated again. The five minute long faults, however, are added to the data in three instances starting from the 10^{th}, 25^{th} and the 40^{th} minutes.

The external sensor pod used for this test was mounted on the ankle of the user. With such foot-mounted IMU, the filtering algorithm is also implemented to incorporate zero-velocity updates, as discussed in Section 2.7.5.3. The navigation algorithm using zero-velocity updates is capable of providing a navigation solution with a reasonable accuracy for much longer durations of time as compared to the navigation algorithm that does not incorporate such velocity updates.

The performance of the sensor validation scheme used in the above described scenario is assessed by computing the position errors along horizontal and vertical directions as shown in Figure 6-43 and Figure 6-44. The errors are plotted for two cases, one with the sensor validation scheme and the other without its use.

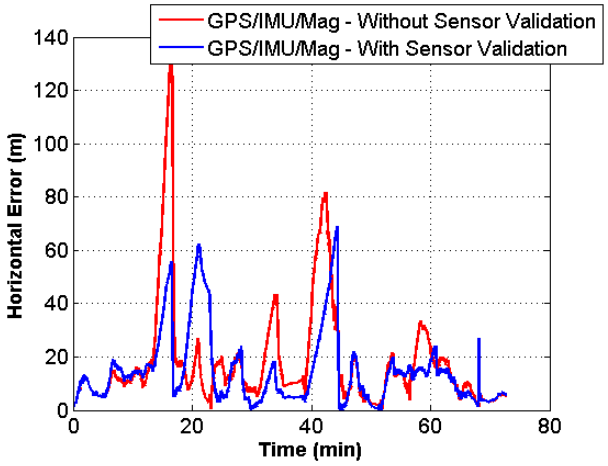

Figure 6-43. Horizontal Errors – With Simulated Magnetometer Errors (Natural Canyon Pedestrian Data-2)

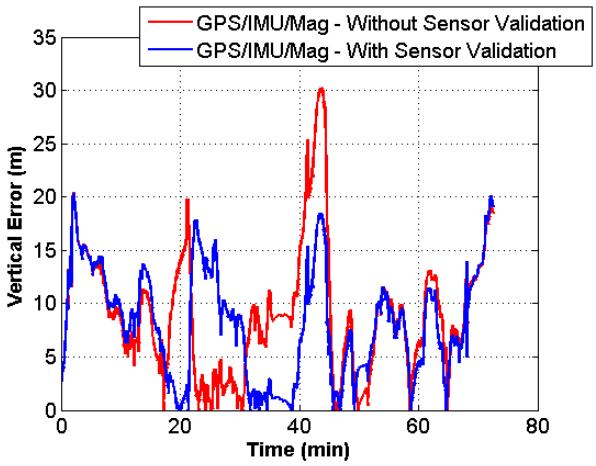

Figure 6-44. Vertical Errors – With Simulated Magnetometer Errors (Natural Canyon Pedestrian Data-2)

The RMS errors and the maximum error values in the above plots are summarized in Table 6-9. The error values are found to be reduced when using the pre-filter sensor validation scheme. The maximum horizontal error in particular is reduced by 50% from 138 to 69 m.

Table 6-9. RMSE and Maximum Errors (Natural Canyon Pedestrian Data-2)

	RMSE (m)		Maximum Error (m)	
	Horizontal	**Vertical**	**Horizontal**	**Vertical**
Without Sensor Validation	19.2	10.8	138	30
With Sensor Validation	13.9	9.5	69	20

6.5.4 Assessment in the Presence of Magnetic Perturbations

The effectiveness of the proposed pre-filter sensor validation scheme is further assessed by processing and analyzing a pedestrian data set collected in an urban area (Urban Canyon Pedestrian Data-2), often characterized by the presence of numerous magnetic perturbing sources.

Urban areas, such as the ones chosen as the test locations during this work, offer harsh GNSS conditions. Thus, aiding the navigation system with measurements from any other sensors could be very useful in improving the performance of the navigation solution. For instance, the heading update from the magnetometer can significantly reduce the errors during poor GNSS conditions. However, an urban area also offers equally harsh conditions for magnetometer measurements due to the abundance of perturbing sources. The interference from these perturbing sources often results in high noise and short term biases in the magnetic field measurement, as depicted in Figure 3-2.

The pre-filter sensor validation scheme must be effective enough to incorporate good magnetic measurements and discard faulty ones. In this regard, the effectiveness of magnetometer validation was examined by computing position errors horizontally and vertically.

Figure 6-45 and Figure 6-46 show the horizontal and vertical errors plotted for three cases:

1. GPS/IMU integrated solution
2. GPS/IMU and magnetometer integrated solution with no pre-filter sensor validation scheme

3. GPS/IMU and magnetometer integrated solution with pre-filter sensor validation scheme

Table 6-10 summarizes the root mean square errors (RMSE) and the maximum error values for the three cases. It is observed that the RMSE and the maximum error values are actually higher, along both horizontal and vertical directions, in the case of the integrated solution that uses magnetometer without the validation scheme as compared to the integrated solution that uses only GPS and IMU. Thus, the magnetic heading update without the validation of magnetometer data proved to have an adverse effect on the navigation solution. However, the inclusion of sensor validation scheme prevented the faulty magnetometer measurements from being used in the integration filter. Consequently, the heading updates with validated magnetometer measurements resulted in better performance. Specifically, both the RMSE and maximum errors along the horizontal direction are reduced by considerable amounts as compared to the case without magnetometer aiding. The improvement along the vertical direction is however very small. This is expected as heading updates affect only the horizontal coordinates.

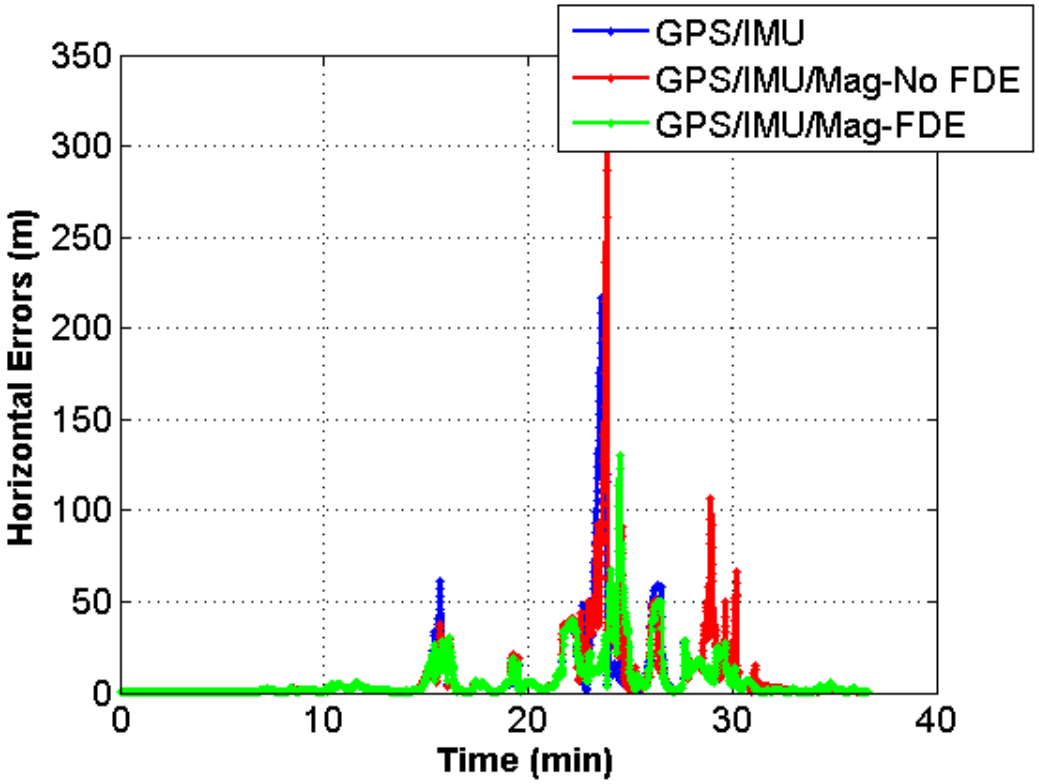

Figure 6-45. Horizontal Errors – OEM6+IMU+Mag (Urban Canyon Pedestrian Data-2)

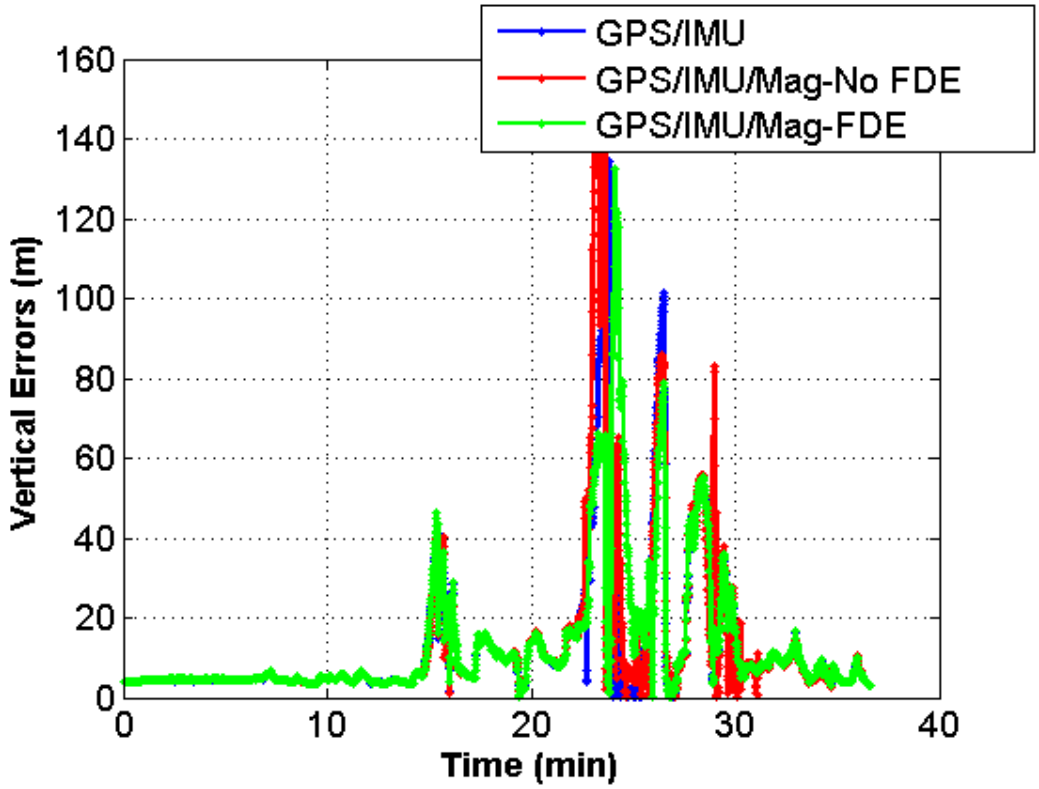

Figure 6-46. Vertical Errors – OEM6+IMU+Mag (Urban Canyon Pedestrian Data-2)

Table 6-10. RMSE and Maximum Errors (Urban Canyon Pedestrian Data-2)

	RMSE (m)		Maximum Errors (m)	
	Horizontal	Vertical	Horizontal	Vertical
GPS/IMU	14.9	22	216	134
GPS/IMU/Mag – Without Sensor Validation	15.6	24	311	157
GPS/IMU/Mag – With Sensor Validation	9.9	21	130	132

Furthermore, the CDF plots of the above results, plotted in Figure 6-47 and Figure 6-48, gives more insight to the performance of the proposed method. These plots depict that the proposed method is superior especially in addressing the gross errors that occur for approximately 10 % to 30 % of the data. The CDF of the horizontal errors, in Figure 6-47, shows the integrate filter that uses heading updates without the fault detection scheme severely deteriorates for the last 30 % of the data. However, on including the FDE these gross errors are significantly reduced.

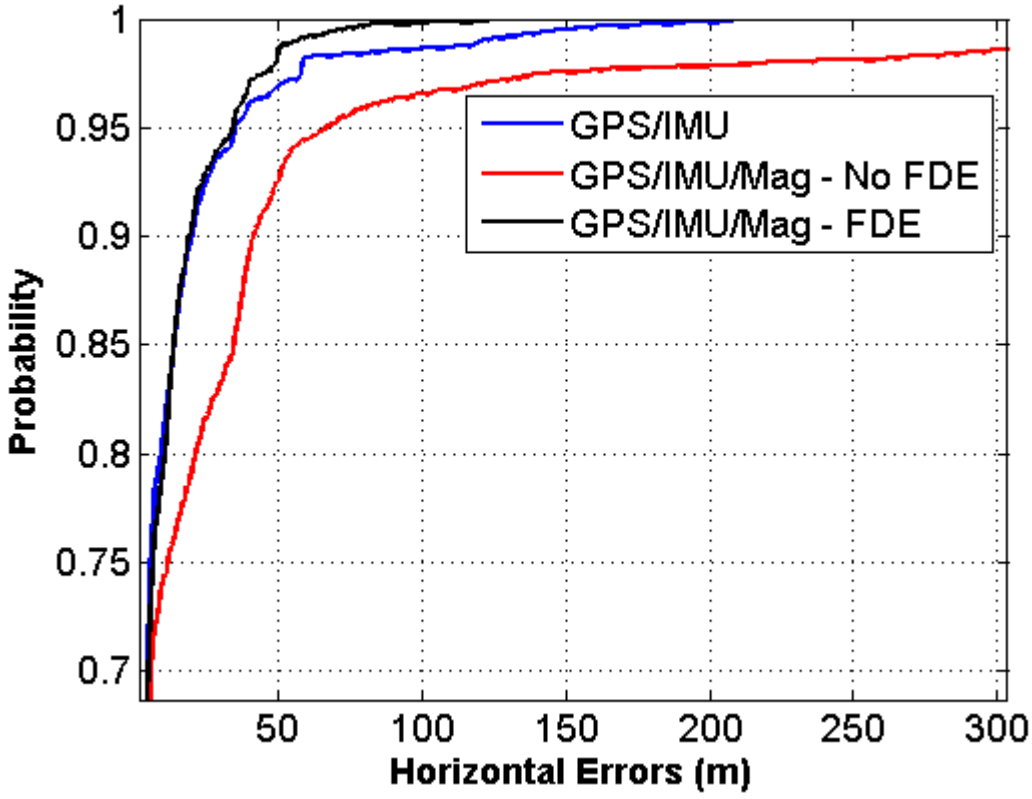

Figure 6-47. CDF of Horizontal Errors – OEM6+IMU+Mag (Urban Canyon Pedestrian Data-2)

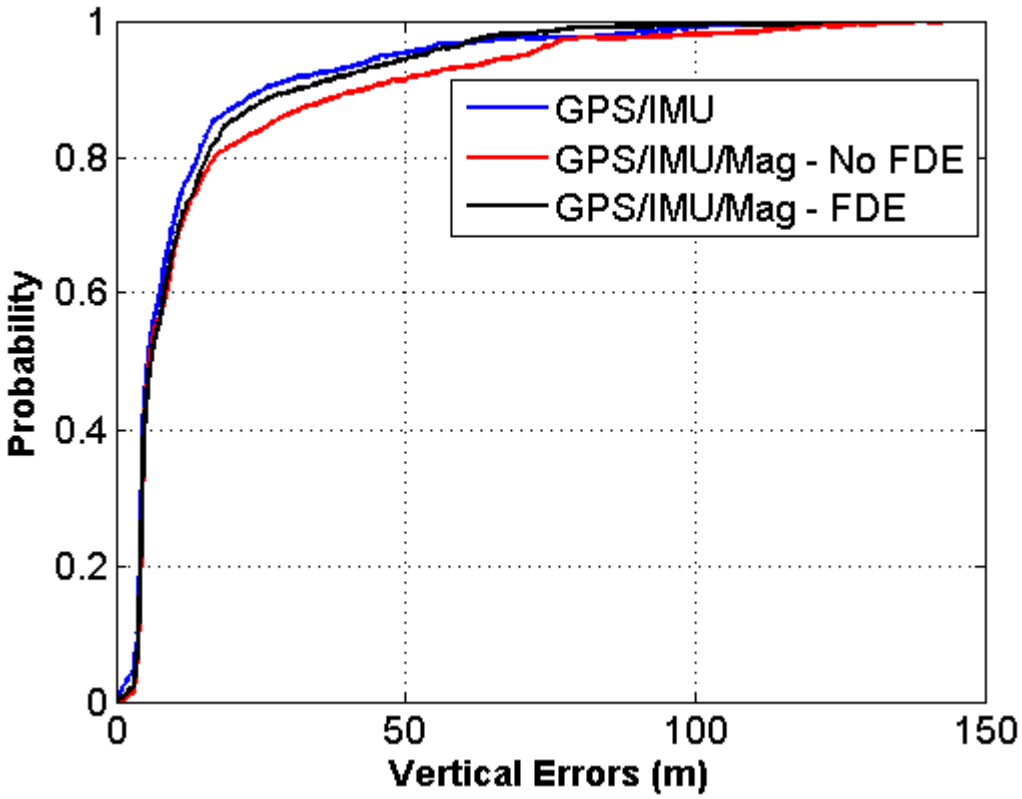

Figure 6-48. CDF of Vertical Errors – OEM6+IMU+Mag (Urban Canyon Pedestrian Data-2)

6.6 Assessment of Complete Filtering Algorithm

Finally, the filtering algorithm that includes all the proposed algorithm modules is assessed for the complete personal navigation system using a pedestrian data collected in an urban canyon environment (Urban Canyon Pedestrian Data-2). As mentioned before, the complete personal navigation system developed during this work includes a GPS receiver, a barometer with accelerometer, gyroscope and magnetometer triads. The navigation filters to be inter-compared are termed “Standard filter” and “Proposed filter”. These filtering algorithms are similar to the “Standard filter” and “VB Adaptive filter”

described in Section 6.4, but include additional data from barometer and magnetometers. Moreover, the proposed filter also incorporates the pre-filter sensor validation scheme presented in Chapter 5. The accuracies of the navigation solutions obtained using the two filters are shown in Figure 6-49 and Figure 6-50. The RMS values of the errors, along with the maximum error values, are given in Table 6-11.

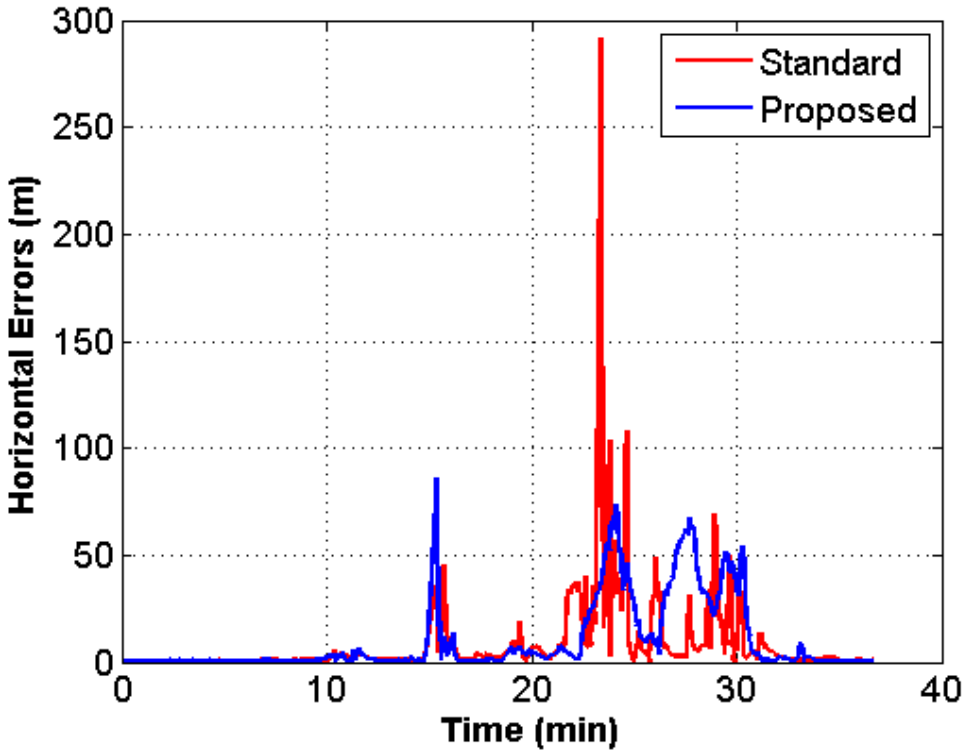

Figure 6-49. Horizontal Errors - Complete System (Urban Canyon Pedestrian Data-2)

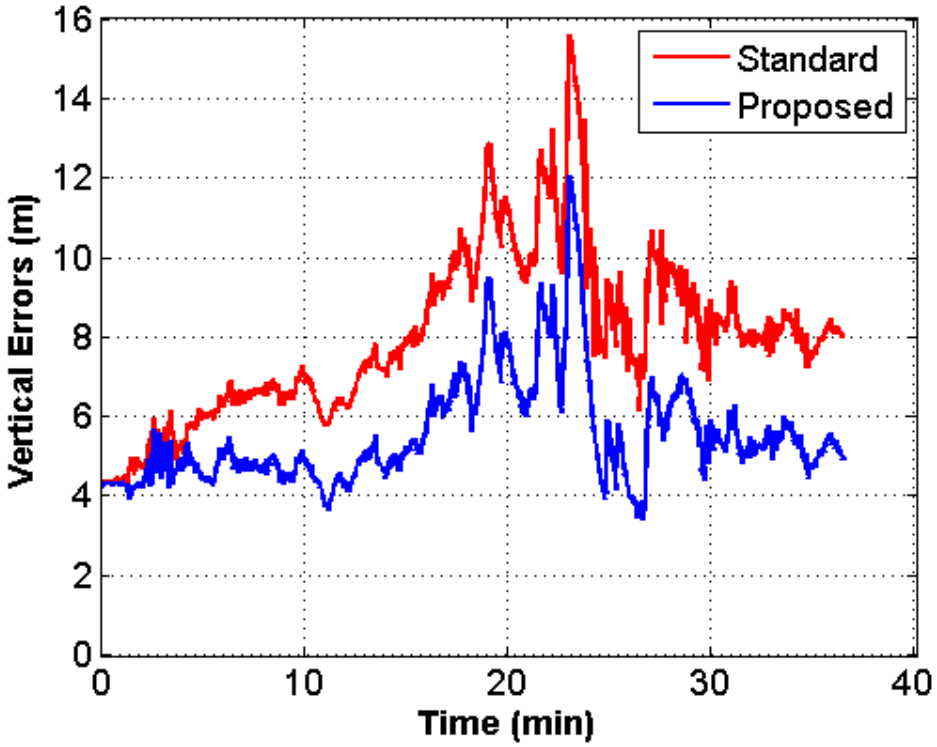

Figure 6-50. Vertical Errors - Complete System (Urban Canyon Pedestrian Data-2)

Table 6-11. RMSE and Maximum Errors (Urban Canyon Pedestrian Data-2)

	RMSE (m)		Maximum Errors (m)	
	Horizontal	**Vertical**	**Horizontal**	**Vertical**
Standard	14.3	8.2	291	15.6
Proposed	13.9	5.7	86	12.1

From the above figures and the table, it is observed that the errors are reduced both horizontally as well as vertically when using the proposed scheme. Specifically, the proposed scheme is seen to be more robust against unmodeled sensor faults that can

cause the navigation solution to deviate significantly from the true trajectory. This is indicated by the high values of maximum errors in the case of the standard filter, which when using the proposed filter decreases significantly.

Moreover, as with the previous data sets and the analyses presented in the previous sections, the algorithm modules within the proposed filter is found to make the navigation solution more reliable as compared to that obtained from the standard filter. This is observed from the reliability values obtained for the two filters as plotted in Figure 6-51.

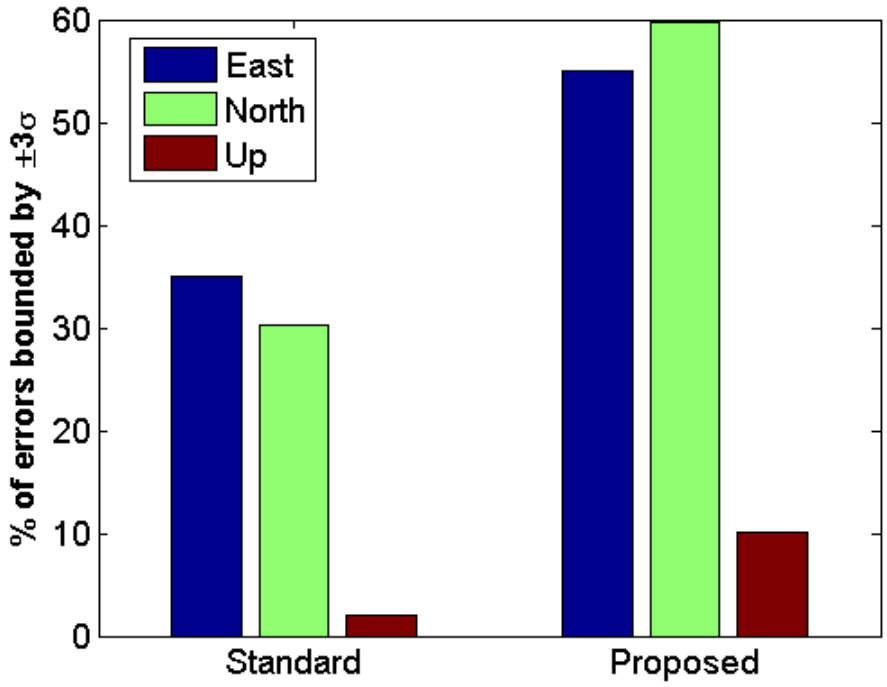

Figure 6-51. Reliability of Navigation Solution – Complete System (Urban Canyon Pedestrian Data-2)

It is observed that the inclusion of barometer in the navigation filter makes the vertical solution more optimistic. This is reflected by the lower reliability values for both the filters, as seen in the above figure. Nonetheless, the improvement on using the proposed algorithms is still significant.

Chapter Seven: **Conclusions and Recommendations**

This research investigated various methods for improving the reliability of a personal navigation system that use multiple sensors. Different algorithm modules were proposed to mitigate the effect of faults occurring in any of the sensors in use on the performance of the navigation system, especially the reliability of the navigation solution. The proposed algorithms were thus assessed for multiple scenarios where faults occur in the sensor measurements. This final chapter draws conclusions from these investigations and provides some recommendations as to what can be done further with regard to improving the reliability of personal navigation systems.

7.1 Conclusions

When navigating in environments with degraded GNSS signal conditions, personal navigation devices, which may use various sensors along with GNSS, often result in highly erroneous and unreliable navigation solutions. Moreover, in navigation systems that are realized as multi-sensor integrated systems, the navigation solution can also degrade due to faults occurring in other sensors besides GNSS. Hence it is necessary to identify and remove these faults. In this regard, the research presented in this thesis can be considered to be composed of two parts. The first part presented novel methods to improve the reliability of personal navigation systems in areas where GNSS signals are degraded. Similarly, the second part developed a sensor validation architecture to detect and remove faults in other sensors before they are used to generate navigation solution in the integration filter. Thus, based on the theoretical development and analyses based

on actual tests conducted in diverse environments as presented in the previous chapters, the following conclusions are deduced:

1. The GNSS measurement covariance adaptive scheme proposed in Chapter 4 significantly improved the reliability of the navigation solution when compared to the standard approach defined in the thesis. The reliability values, computed along the three mutually perpendicular axes of the local level frame, were found to improve substantially for both vehicular and pedestrian data sets collected in urban canyons. On average, single-axis reliability was found to increase by approximately 15 % when using the proposed covariance adaptive scheme.
2. The covariance adaptive scheme was also found to be more robust than the standard approach in the sense that the maximum errors occurring during extremely harsh signal conditions were significantly reduced. The accuracy of the navigation solution was also found to improve.
3. Adaptation of the GNSS measurement covariance also mitigated unnecessary measurement rejections due to improper characterization of GNSS measurement noise. This led to an increase in the availability of GNSS measurements, which could also be retained by over-bounding their errors. However, mere over-bounding through the adoption of higher covariance values can lead to poor accuracy. Although the algorithm slightly over-bounded the assumed GNSS error distribution during good signal conditions, the fact that the overall accuracy did not degrade and instead became better, proves the validity of the proposed covariance adaptation method.

4. One of the limitations of the proposed covariance adaptive algorithm is that a minimum number of Doppler measurements is required to compute the user acceleration for the covariance adaptation. This condition was not always met at the test locations and, as a result, the covariance could not be adapted all the time. However, the benefit of the proposed scheme was magnified when assessing the scheme in a simulated environment with several simultaneously degraded satellite signals but still having a sufficient number of Doppler measurements to compute user acceleration. The average reliability in this case improved by 26 %.
5. The Student's t-distribution is more representative of the GNSS measurement errors in harsh environments as compared to the normal distribution. The implementation of the integrated navigation system with an assumption of *t* distribution for GPS measurement errors resulted in better accuracy and reliability in harsh environments, without degrading the solution in open sky environments. The maximum horizontal error decreased by a factor of about 2.5 when using the *t* distribution. The *t* distribution based algorithm also improved the reliability of the navigation solution as well as the measurement availability.
6. The integration of the two algorithm modules presented in Chapter 4, termed as VB (Variational Bayes) Adaptive during the analysis, resulted in the best performance in terms of reliability of the navigation solution. The analyses of this combined module, performed using two pedestrian data sets collected in harsh environments, showed an average reliability improvement of approximately 22 %.
7. The analysis of the proposed pre-filter sensor validation architecture was preceded by a detailed theoretical study and experimental analyses of the nature of the faults

in various sensors. This was necessary in order to simulate realistic faults in the sensor measurements for the assessment of the proposed sensor validation algorithm.

8. The dynamics associated with pedestrian navigation applications imposes a major challenge in the computation of user accelerations from an IMU. The errors in the estimated attitude (especially roll and pitch) result in the infiltration of the gravity component into the user acceleration, which makes the acceleration comparison in the validation architecture very challenging.
9. The proposed architecture was able to detect the sustained faults simulated in the accelerometers by correctly identifying the inconsistency of user acceleration values when compared to the user accelerations obtained from other sensors. The architecture however is not able to detect short-term accelerometer errors as these cannot be distinguished from the occasional gravity component infiltration caused by user dynamics.
10. The sensor validation architecture successfully prevented the faulty barometer measurements from entering the integration filter. The simulated faults resembled the scenario with high wind conditions. The adoption of the sensor validation scheme during such fault simulated conditions reduced the maximum error values by approximately 38 m along the vertical direction and 12 m along the horizontal direction.
11. Heading updates from a magnetometer can significantly improve the performance of the integrated system in areas where GNSS is degraded. However, the faults arising in magnetometer measurements due to interference from ferromagnetic

substances in the vicinity can make the heading update counter-effective, further deteriorating the navigation solution. The detection and removal of magnetometer faults using the proposed technique considerably improved the accuracy of the navigation solution. In particular, the maximum horizontal error was significantly reduced.

12. The complete filtering algorithm, which incorporates the novel methods proposed in Chapter 4 and Chapter 5, provided navigation solutions with better accuracy and reliability, thus validating the benefits of using the proposed techniques in personal navigation devices.

7.2 Recommendations

Considering the findings of this research, the following recommendations are suggested for future work:

1. The concept of validating sensor measurements through the observation of common parameters using dissimilar sensors can be applied to improve the estimation of those parameters that are used in a navigation filter. For instance, the angular velocity obtained from the magnetometer could be used to improve the angular velocity estimate from a low cost gyroscope.
2. In order to be able to incorporate more magnetometer measurements in areas with many perturbing sources, a magnetometer calibration technique that can perform on the fly calibration could be used. Such a calibration method must however have an acceptable accuracy and should be computationally effective.

3. The effects of user dynamics on the computation of IMU accelerations can be mitigated by using advanced techniques that deal with these dynamics.
4. The benefits of the proposed algorithms can be explored in pedestrian navigation applications that are realized using pedestrian dead reckoning method instead of the strap-down configuration.
5. The analysis of the proposed methods using different grades of inertial sensors could provide an interesting insight into the suitability of these methods for various applications.
6. The proposed methods can be further extended by inclusion of new sensors and signals including wheel speed sensors (for vehicular use), Wi-Fi, etc. The inclusion of such sensors is likely to further improve the performance of personal navigation devices through the addition of new observations, constraints and redundancies.

References

Afzal, H., V. Renaudin, and G. Lachapelle (2011) “Multi-magnetometer based perturbation mitigation for indoor orientation estimation,” *Navigation*, Vol. 58, No. 4, pp. 279-292

Allan, D. W. (1966) “Statistics of atomic frequency standards,” in *Proceedings of the IEEE*, vol 54, no 2, pp. 221–230

Almagbile, A., J. Wang, and W. Ding (2010) “Evaluating the Performances of Adaptive Kalman filter Methods in GPS/INS Integration,” *Journal of Global Positioning Systems*, vol. 9, no. 1, pp. 33-40, October 2010

Angus, J.E. (2006) "RAIM with Multiple Faults," *Navigation*, Vol. 53, Issue 4, pp. 249-257

Arasaratnam, I. and S. Haykin (2009) “Cubature Kalman Filters,” *IEEE Transactions on Automatic Control*, vol. 54, no. 6, pp. 1254-1269

Arunlampalam, M.S., S. Maskell, N. Gordon and T. Clapp (2002) “A Tutorial on Particle Filters for Online Nonlinear/Non-Gaussian Bayesian Tracking” *IEEE Transactions on Signal Processing 2002*, vol. 50, no. 2, pp. 174-188

Axelrad, P. and R.G. Brown (1996) “GPS Navigation Algorithms,” in *Global Positioning System: Theory and Applications Volume I*, Parkinson, B.W. and J.J. Spilker Jr., American Institute of Aeronautics and Astronautics, Inc., pp. 409-434

Baarda, W. (1967) *Statistical Concepts in Geodesy,* Netherlands Geodetic Commission, vol. 2, no. 4

Bancroft, J.B. (2010) *Multiple Inertial Measurement Unit Integration for Pedestrian Navigation,* PhD Thesis, Department of Geomatics Engineering, University of Calgary (Available at http://plan.geomatics.ucalgary.ca)

Bancroft, J.B. and G. Lachapelle (2011), "Data Fusion Algorithms for Multiple Inertial Measurement Units," *Sensors*, MDPI, vol. 11, no. 7, pp. 6771-6798

Benzerrouk, H., A. Nebylov, H. Salhi and P.Closas (2014) "MEMS IMU/ZUPT Based Cubature Kalman Filter applied to Pedestrian Navigation System," in *Proceedings of International Electronic Conference on Sensors and Applications*

Bhaskar, S. (2014) "Exploiting quasi-periodicity in receiver dynamics to enhance GNSS carrier phase tracking," in *Proceedings of ION GNSS+ 2014*, Tampa, FL, U.S. Institute of Navigation, Fairfax VA

Bickerstaff, J., R. Frayling-Cork, and T. Haddrell (2006) "Capture, Analysis and Mitigation of Multipath in a High Sensitivity GPS Receiver," in *Proceedings of the ION GNSS 2006*, 26-29 September, Fort Worth, TX, pp. 1696-1705, U.S. Institute of Navigation, Fairfax VA

Bicking, R. E. (1998) *Fundamentals of Pressure Sensor Technology* (http://www.sensorsmag.com/sensors/pressure/fundamentals-pressure-sensor-technology-846)

Bras, S., P. Rosa, C. Silvestre, and P.Pliveira (2012) “Fault Detection and Isolation for Inertial Measurement Units,” in Proceedings of 51st IEEE Conference on Decision and Control, 10-13 December, Maui, Hawaii, USA

Brown, R. G. and P. Y. C. Hwang (1997) *Introduction To Random Signals and Applied Kalman Filtering, 3rd Ed,* John Wiley & Sons, Inc., Hoboken, NJ

Caruso, M.J. (1997) “Applications of Magnetoresistive Sensors in Navigation Systems,” *SAE Transactions*, vol. 106, pp. 1092-1098

Caruso, M.J., T.Bratland, C.H.Smith and R.Schneider (1998) “A New Perspective on Magnetic Field Sensing,” in *Proceedings of Sensors Expo*, October 1998, pp. 195-213

Dhital A. (2010) *Bayesian Filtering for Dynamic Systems with Applications to Tracking*, MSc Thesis, Department of Signal Theory and Communications, Universitat Politecnica de Catalunya, Spain

Dhital A., A. Morrison and G. Lachapelle (2011) “Improvement of GNSS positioning with proper calibration of Inter-channel and Inter-element bias in receiver front-ends,” in *Proceedings of ION GNSS 2011*, 20-23 September, Portland, OR, pp. 2022-2030, U.S. Institute of Navigation, Fairfax VA

Dorveaux, E., D. Vissiere, A. P. Martin and N. Petit, “Iterative calibration method for inertial and magnetic sensors,” in *Proceedings of 48th IEEE Conference on Decision Control held jointly with the 28th Chinese Control Conferenc*e,15-18 December, Shanghai, China, pp. 8296–8303

El-Sheimy, N. (2006) *Inertial Techniques and INS/DGPS Integration*, ENGO 623 Course Notes, Department of Geomatics Engineering, University of Calgary, Canada

El-Sheimy, N., H. Hou and X. Niu (2008) "Analysis and Modeling of Inertial Sensors Using Allan Variance," *IEEE Transactions on Instrumentation and Measurement*, vol. 57, no. 1, pp. 140-149

Fang, J., H. Sun, J. Cao, X. Zhang and Y. Tao (2011) "A novel calibration method of magnetic compass based on ellipsoid fitting," IEEE Transactions on Instrumentation and Measurements, vol. 60, no. 6, pp. 2053–2061

Farrell, J. and M. Barth (1999) *The Global Positioning System & Inertial Navigation*, McGraw Hill Professional, New York

Gebre-Egziabher, D., G. H. Elkaim, J. D. Powell and B. W. Parkinson (2006) "Calibration of Strapdown Magnetometers in Magnetic Field Domain," *Journal of Aerospace Engineering*, vol. 9, no. 2, pp. 87–102

Gelb, A. (1974) *Applied Optimal Estimation*, M.I.T. Press, Cambridge MA, pp. 42-45

Gelman, A., J. B. Carlin, H. S. Stern, D. B. Dunson, A. Vehtari and D. B. Rubin (1995) *Bayesian Data Analysis*, CRC Press

Godha, S. (2006) *Performance Evaluation of Low Cost MEMS-Based IMU Integrated with GPS for Land Vehicle Navigation Application*, MSC Thesis, Department of Geomatics Engineering, University of Calgary (Available at http://plan.geomatics.ucalgary.ca)

GPS World (2013) *AP15 GNSS-Inertial Board Set for Positioning*, http://gpsworld.com/trimble-launches-ap15-gnss-inertial-board-set-for-positioning/, last accessed February 10, 2014

Grewal, M.S., L. R. Weill, and A. P. Andrews (2001) *Global Positioning Systems, Inertial Navigation, and Integration*, John Wiley & Sons, Inc., Hoboken, NJ

Grewal, M. S. and A. P. Andrews (1993) *Kalman Filtering Theory and Practice*, Prentice Hall, Upper Saddle river, NJ

Groves, P. (2013) *Principles of GNSS, Inertial, and Multisensor Integrated Navigation Systems*, *2nd Ed*, Artech House, London, UK

Hide, C., T. Moore, and M. Smith (2002) "Adaptive Kalman Filtering for Low Cost INS/GPS," in *Proceedings of ION GPS 2002*, 24-27 September, Portland, OR, pp. 1143-1147, U.S. Institute of Navigation, Fairfax VA

ICD GLONASS 5.1 (2008) *Navigational radio-signal in bands L1, L2 Information-Analytical Centre*

IEEE Standard 647 (2006) *IEEE Standard Specification Format Guide and Test Procedure for Single-Axis Laser Gyros*, IEEE

Jirawimut, R., P. Ptasinski, V. Garaj, F. Cecelja and W. Balachandran (2003) "A method for dead reckoning parameter correction in pedestrian navigation system," *IEEE Transactions on Instrumentation and Measurement*, vol. 52, no. 1, pp. 209–215

Kalman, R. E. (1960) “A New Approach to Linear Filtering and Prediction Problems,” *ASME Journal of Basic Engineering*, vol. 82, pp. 34–45

Kay, S.M. (2001) *Fundamentals of Statistical Signal Processing: Estimation Theory*, Prentice Hall, Upper Saddle River, NJ

Kolpekwar, A., R. D. Blanton and D. Woodilla (1998) “Failure modes for stiction in surface-micromachined MEMS,” in *Proceedings of International Test Conference*, 18-23 October, Washington, DC, pp. 551-556

Kuipers, J.B. (1999) *Quaternions and rotation Sequences: a Primer with Applications to Orbits, Aerospace, and Virtual Reality*, Princeton University Press, Princeton NJ

Kuusniemi, H. (2005) *User-Level Reliability and Quality Monitoring in Satellite-Based Personal Navigation*, PhD Thesis, Tampere University of Technology, Finland, pp.87-93

Lachapelle, G. (2010) *Advanced GNSS Theory and Applications*, ENGO 625 Course Notes, Department of Geomatics Engineering, University of Calgary, Canada

Lange, K.L., R.J.A. Little and J. M.G. Taylor (1989) “Robust Statistical Modeling Using the t Distribution,” *Journal of the American Statistical Association*, vol. 84, no. 408, pp 881-896

Lee, Y.C. (1986) "Analysis of range and position comparison methods as a means to provide GPS integrity in the user receiver," in *Proceedings of the Annual Meeting of the Institute of Navigation*, 24-26 June, Seattle WA, pp.1-4, U.S. Institute of Navigation, Fairfax VA

Leick, A. (2004) *GPS Satellite Surveying, 3rd Ed*, John Wiley & Sons, Inc., Hoboken, NJ

Maybeck, P. S. (1994) *Stochastic Models, Estimation and Control*, *vol. 1*, NavtechGPS, Arlington, VA

McLellan, J.F., J. Schleppe, D. McLintock and G. Deren (1994) "GPS/barometry height-aided positioning system," in Proceedings of IEEE/ION PLANS 1994, 11-15 April, Las Vegas, NV, pp. 369-375

Mishra, P. and P. Enge (2011) *Global Positioning System: Signals, Measurements, and Performance*, Ganga-Jamuna Press, Loncoln MA, pp. 3-66

Morrison, A., V. Renaudin, J. B. Bancroft and G. Lachapelle (2012) "Design and Testing of a Multi-Sensor Pedestrian Location and Navigation Platform," *Sensors*, vol. 12, no. 3, pp 3720-3738

Nassar, S. (2003) *Improving the Inertial Navigation System (INS) Error Model for INS and INS/DGPS Applications*, PhD Thesis, Department of Geomatics Engineering, University of Calgary, Canada

Nassar, S., K. P. Schwarz, A. Noureldin and N. El-Sheimy (2003) "Modeling Inertial Sensor Errors Using Autoregressive Models," in *Proceedings of the ION NTM 2003*, 22-24 January, Anaheim CA, pp. 116-125 , U.S. Institute of Navigation, Fairfax VA

Noureldin A., T. B. Karamat and J. Georgy (2013) *Fundamentals of Inertial Navigation, Satellite-based Positioning and their Integration*, Springer-Verlag, Berlin, Germany

Papoulis, A. (1991) *Probability, Random Variables, and Stochastic Processes*, 3rd Edition, McGraw-Hill, New York, pp. 410-460

Parkinson B.W. (1996) “GPS Error Analysis,” in *Global Positioning System: Theory and Applications Volume I*, Parkinson, B.W. and J.J. Spilker Jr., American Institute of Aeronautics and Astronautics, Inc., pp. 469-484

Parkinson, B.W. and P.A. Axlerad (1987) "Basis for the Development of Operational Algorithms for Simplified GPS Integrity Checking," in *Proceedings of the ION GPS 1987*, 21-25 September , Colorado Springs CO, pp. 269-276, U.S. Institute of Navigation, Fairfax VA

Piche, R., S. Sarkka and J. Hartikainen (2012) “Recursive Outlier-Robust Filtering and Smoothing for Nonlinear Systems using the Multivariate Student-t Distribution,” in *Proceedings of 2012 IEEE International Workshop on MSLP*, 23-26 September, Santander, Spain, pp. 1-6

Renaudin, V., H. Afzal and G. Lachapelle (2010) “Complete tri-axis magnetometer calibration in the magnetic domain” *Journal of Sensors*, vol. 2010, Hindawi

Schroth, G., A. Ene, J. Blanch, T. Walter, and P. Enge (2008) "Failure Detection and Exclusion via Range Consesus," in *Proceedings of the European Navigation Conference*,21-25 April , Toulouse

Schwarz, K.P. and M. Wei (1990) "Efficient Numerical Formulas for the Computation of Normal Gravity in a Cartesian Frame," *Manuscripta Geodaetica*, vol. 15, no. 4, pp. 228-234

Serrano, L., D. Kim, R. B. Langley (2004) "A single GPS Receiver as a Real-Time, Accurate Velocity and Acceleration Sensor," in *Proceedings of the ION GNSS 2004*, 21-24 September, Long Beach CA, pp. 2021-2034, U.S. Institute of Navigation, Fairfax VA

Simon, J., J. Vazquez, A. Madrazo, A. Cezon, and W. Enderle (2010) "Advanced RAIM scheme and its evaluation for non-aeronautical users in different environments," in *Proceedings of the ION GNSS 2010*, 21-24 September, Portland, OR, pp. 292-300, U.S. Institute of Navigation, Fairfax VA

Sturza, M.A. (1988) "Navigation system integrity monitoring using redundant measurements," *Navigation*, Vol. 35, Issue 4, pp. 483-501

Sukkarieh, S., P. Gibbens, B. Grocholsky, K. Willis, and H.F. Durrant-Whyte (2000) “A Low-Cost, Redundant Inertial Measurement Unit for Unmanned Air Vehicles,” *The International Journal of Robotics Research*, vol. 19, no. 11, pp. 1089-1103

Susi, M. (2012) *Gait Analysis for Pedestrian Navigation Using MEMS Handheld Devices*, MS Thesis, University of Calgary, Canada

Tabatabaei, S. A. H., A. Gluhak and R. Tafazolli (2013) “A Fast Calibration Method for Triaxial Magnetometers,” *IEEE Transactions on Instrumentation and Measurement*, vol. 62, no. 11, pp. 2929-2937

Tas, N., T. Sonnenberg, H. Jansen, R. Legtenberg and M. Elwenspoek (1996) “Stiction in surface micromachining,” Journal of Micromechanics and Microengineering, vol. 6, no. 4, pp. 385-397

Thacker, N.A., F.J. Aherne and P. Rockett (1998) "The Bhattacharyya Metric as an Absolute Similarity Measure for Frequency Coded Data," *Kybernetika*, vol. 34, no. 4, pp. 363-368

Titterton, D. H. and J. L. Weston (2004) *Strapdown Inertial Navigation Technology, 2nd Ed*, The Institution of Electrical Engineers, Herts, UK

Van Diggelen, F. (2009) *A-GPS: Assisted GPS, GNSS, and SBAS*, Artech House, Boston MA, pp. 127-223

Vanícek, P. and E. J. Krakiwsky (1986) *Geodesy: The Concepts, 2nd Ed*, Elsevier, Amsterdam, Netherlands

Webb, A. and K. Copsey (2011) *Statistical Pattern Recognition, 3rd Ed*, John Wiley & Sons, Ltd., West Sussex, UK, pp. 126-137

Wei, S.Y. and J.R. Huddle (1986) “Sensor Management for a Fault Tolerant Integrated Inertial Flight Control Reference and Navigation System,” in *Proceedings of the IEEE Plans 1986*, 4-7 November, Las Vegas, NV, pp. 445-455

Wieser, A., M. Gaggl and H. Hartinger (2005) “Improved Positioning Accuracy with High Sensitivity GNSS Receivers and SNR Aided Integrity Monitoring of Pseudo-Range

Observations," in Proceedings of the ION GNSS 2005, Long Beach CA, USA, 13-16 September, pp. 1545-1554, Institute of Navigation, Fairfax VA, USA

APPENDIX A: GNSS RANGE ERROR COMPUTATION

GNSS pseudorange measurements can be expressed as

$$\rho = r + cdt + \varepsilon \quad \textbf{A-1}$$

where ρ is the pseudorange, r is the true range (true distance between the satellite and the receiver position), cdt is the receiver clock bias and ε is the total range error which include atmospheric errors, orbital errors and multipath.

With the availability of an accurate reference solution for the user locations and with the knowledge of satellite positions from the ephemeris data, the true range r can be calculated. Now the problem lies in the segregation of ε from cdt.

The clock bias can be estimated in a filter by fixing the known receiver position and velocity from the reference solution and by modeling ε as a stochastic parameter. However, despite having a high observability obtained by fixing user position and velocity, accurate clock estimation cannot still be obtained. This is because of the fact that, in presence of large biases, cdt and ε get highly correlated due to which some part of ε gets consumed in cdt.

Thus, to mitigate the effect of multipath and other biases and noise in the estimation of cdt, an FIR filter is applied to the estimated clock bias. Finally, the range error is computed as

$$\varepsilon = \rho - r - \widehat{cdt} \quad \textbf{A-2}$$

where $\widehat{cdt}$ is the filtered clock bias.

APPENDIX B: COMPUTATION OF USER ACCELERATION FROM GNSS DOPPLER MEASUREMENTS

The user acceleration can be obtained from GNSS, either using phase measurements or Doppler measurements. In either case, the first step is to obtain the phase range acceleration. Assuming that phase measurements are used, the carrier phase range acceleration is obtained as follows (Serrano et al 2004):

$$\ddot{\phi}(t) \approx \frac{\dot{\phi}(t+\Delta t) - \dot{\phi}(t-\Delta t)}{2\Delta t} = \frac{\phi(t+\Delta t) - 2\phi(t) + \phi(t-\Delta t)}{4\Delta t^2} \quad \textbf{B-1}$$

where

$$\dot{\phi}(t) \approx \frac{\phi(t+\Delta t) - \phi(t-\Delta t)}{2\Delta t}$$

Now, the velocity (Doppler) measurements can be expressed as

$$\dot{\phi}_i = u_i.(v_u - v_{s,i}) + \dot{B}_{u,i} + \dot{d}_{ion,i} + \dot{d}_{trop,i} + \dot{\xi}_i + \dot{\varepsilon}_i \quad \textbf{B-2}$$

where u_i is the unit vector of the ith satellite, v_u is the user velocity, $v_{s,i}$ is the velocity of the ith satellite, $\dot{B}_{u,i}$ is the clock drift, $\dot{d}_{ion,i}$ is the ionospheric delay rate, $\dot{d}_{trop,i}$ is the tropospheric delay rate, $\dot{\xi}_i$ is the rate of change of orbital error and $\dot{\varepsilon}_i$ is the contribution of the receiver noise and other unmodeled errors. The contribution of atmospheric errors and orbital errors are usually very small and thus can be considered as a part of the stochastic noise component. Equation B-2 can thus be re-written as

$$\dot{\phi}_i = u_i.(v_u - v_{s,i}) + \dot{B}_{u,i} + \dot{\varepsilon}_{u,i} \qquad \textbf{B-3}$$

where

$$u_i = \begin{bmatrix} u_{x,i} \\ u_{y,i} \\ u_{z,i} \end{bmatrix}$$

The range acceleration is given as

$$\ddot{\phi}_i = \dot{u}_i.(v_u - v_{s,i}) + u_i.(a_u - a_{s,i}) + \ddot{B}_u + \ddot{\varepsilon}_{u,i} \qquad \textbf{B-4}$$

where a_u and $a_{s,i}$ are user and satellite velocities respectively.

The rate of change of the unit directional vector is approximately zero. Hence, we assume $\dot{u}_i = 0$. The range accelerations and user acceleration can thus be shown to be related as

It can be shown that the range accelerations and user acceleration are related as

$$\begin{bmatrix} \ddot{\phi}_1 + u_1.a_{s,1} \\ \ddot{\phi}_2 + u_2.a_{s,2} \\ \vdots \\ \ddot{\phi}_N + u_N.a_{s,\mathrm{N}} \end{bmatrix} = \begin{bmatrix} u_{x,1} & u_{y,1} & u_{z,1} & 1 \\ u_{x,2} & u_{y,2} & u_{z,2} & 1 \\ \vdots & \vdots & \vdots & \vdots \\ u_{x,N} & u_{y,N} & u_{z,N} & 1 \end{bmatrix} \begin{bmatrix} a_x \\ a_y \\ a_z \\ \ddot{B}_u \end{bmatrix} + \begin{bmatrix} \ddot{\varepsilon}_{u,1} \\ \ddot{\varepsilon}_{u,2} \\ \vdots \\ \ddot{\varepsilon}_{u,N} \end{bmatrix} \qquad \textbf{B-5}$$

This is in the form:

$z = Hx + \varepsilon$

where z is the measurement vector, x is the vector of state parameters, H is the design matrix relating the state parameters to the measurements and ε is the error vector.

The accelerations can thus be estimated by solving Equation B-5 using least squares technique.